

UNIVERSIDADE DE LISBOA
FACULDADE DE CIÊNCIAS
DEPARTAMENTO DE FÍSICA



Ciências
ULisboa

Improving foetal and neonatal echo-planar imaging with image-based shimming.

Mestrado Integrado em Engenharia Biomédica e Biofísica
Perfil em Sinais e Imagens Médicas

Andreia Sofia Oliveira Gaspar

Dissertação orientada por:
Doutor Anthony Price e Doutora Rita Nunes

Abstract

The Developing Human Connectome Project (dHCP) aims to make major scientific progress by creating the first 4-dimensional connectome of early life. Echo planar imaging (EPI) is the main acquisition technique applied in functional and diffusion imaging, which are central to map the human brain. This technique allows fast acquisition of spatial information enabling volumetric coverage of the whole brain, but it is associated with susceptibility artefacts. In order to minimize those artefacts it is necessary to reduce main magnetic field B_0 inhomogeneities through shimming.

Conventionally, the attempts to overcome this problem use the manufacturer's default method. Unfortunately, with those techniques the user has little control over the process, and the regions within which the field is corrected are not anatomically based. The main objective of this project was to develop an image-based shimming tool to optimize the magnetic field in the context of EPI images adjusted to the neonatal and foetal brains.

The babies' brain suffers changes in dimension and shape during its development from foetal to neonatal age. In each one of those stages the baby is surrounded by a different environment which requires a distinct shimming approach. As a result, the work was divided into three main parts: framework description, neonatal shimming and foetal shimming.

First, the limitations of image-based shimming were investigated, and the framework to apply the method was described. It was demonstrated that fields generated by shim coils were consistent with the spherical harmonic model applied. In addition, the coordinate information of the B_0 field map was corrected in order to include the table displacement needed for foetal imaging.

Second, a tool was developed for neonatal shimming. The tool included region-of-interest (ROI) definition, phase unwrapping and shim calculation. The ROI definition implemented was flexible in order to adjust to each subject under study. When applying this approach while keeping the same threshold/eye exclusion methodology the volume included was similar between babies. The shim calculation allowed to generate shim values that improved homogeneity of the magnetic field within the volume imaged. This method slightly improved the field near the brain's margins when compared with the manufacturer's default techniques.

Finally, for foetal shimming the groundwork of the neonatal tool was adjusted to this co-

hort characteristics. The tool for foetal shimming included additional cylindrical ROI definition and constrained image-based shimming. The constrained shimming allowed to account for the mother's adipose tissue which in the presence of high shim values can lead to imperfect fat suppression. Along with the implementation of shimming tools, the radio frequency pulse used for fat suppression was studied. The new constrained image-based shimming showed similar results in terms of field homogeneity within the fetus' brain when compared with the optimal image-based shimming, with improvement of fat suppression that is enhanced when simultaneously used with the optimized fat suppression radiofrequency pulse.

Keywords: Echo planar imaging, image-based shimming, foetal, neonatal.

Resumo

O *Developing Human Connectome Project* pretende realizar um progresso científico único através da criação do primeiro *connectome 4D* no início da vida do bebé. De forma a criar um mapa dinâmico da conectividade do cérebro do bebé é fundamental obter imagens funcionais e com ponderação em difusão.

A imagem eco-planar (EPI) é a principal sequência de ressonância magnética aplicada na aquisição dessa informação. Esta sequência permite uma aquisição rápida e repetida de imagens cerebrais permitindo mapear as flutuações da atividade cerebral (imagiologia funcional) bem como ter uma boa resolução nas imagens de difusão (movimento de moléculas de água no volume cerebral).

No entanto, esta técnica está associada a artefactos de suscetibilidade. Estes artefactos surgem quando existem interfaces entre duas amostras com suscetibilidades magnéticas diferentes como sejam o tecido biológico e o ar. De forma a minimizar esses artefactos é necessário reduzir as heterogeneidades do campo magnético principal B_0 através de *shimming*. O presente trabalho focou-se em *shimming* ativo, no qual o campo magnético é mapeado com base num modelo composto por funções harmónicas esféricas e são calculadas as correntes a aplicar às bobinas de *shimming*. Essas bobinas geram um campo magnético que compensa as heterogeneidades presentes anteriormente.

Convencionalmente, as tentativas para superar este problema envolvem a utilização do método disponibilizado no sistema de ressonância magnética, nas quais o campo é mapeado com base em projeções (ex: FASTMAP). Este método é de execução rápida mas apresenta duas desvantagens principais: em primeiro lugar, o utilizador tem um controlo reduzido sobre o processo; em segundo, as regiões nas quais o campo é mapeado não são definidas com base na anatomia de interesse. No contexto deste trabalho, o controlo sobre o processo é importante no sentido de ser possível aplicar exatamente a mesma metodologia a um grupo elevado de sujeitos. Por seu lado, o mapeamento com base na anatomia permite obter uma otimização mais precisa. Com o surgimento de novas tecnologias passou a ser possível fazer um mapeamento mais detalhado do campo magnético com técnicas baseadas em imagem ao invés de projeções. Estas técnicas envolvem a definição de um volume relacionado com a anatomia, e que é incluído na totalidade na otimização do campo.

O principal objetivo deste trabalho foi desenvolver uma ferramenta de *shimming* baseado em imagem a fim de otimizar o campo magnético no contexto de imagens de EPI do cérebro neonatal e fetal.

O cérebro do bebê sofre alterações na sua dimensão e forma durante o seu desenvolvimento desde a idade fetal até neonatal. Em cada uma dessas fases o bebê encontra-se cercado por um ambiente diferente que requer uma abordagem específica ao mesmo. Neste sentido, o trabalho desenvolvido foi dividido em três partes principais: descrição da estrutura necessária para a correta aplicação do *shimming*, *shimming* neonatal e *shimming* fetal.

Em primeiro lugar, as limitações do *shimming* baseado em imagem foram estudadas e o algoritmo básico para aplicar o método foi testado. Nesta parte do trabalho foi demonstrado que os campos gerados pelas bobinas de *shim* presentes no equipamento de ressonância magnética são consistentes com as funções harmônicas esféricas que compõem o modelo aplicado. O efeito do movimento da cama do equipamento sobre a eficiência do *shimming* foi também estudada. Foi possível corrigir a informação do sistema de coordenadas que descrevem o mapa de campo B_0 de forma a incluir o movimento da cama necessário para a obtenção das imagens em sujeitos fetais.

A segunda parte do trabalho focou-se no desenvolvimento do *shimming* para o caso neonatal. Foi desenvolvida uma ferramenta para definição de uma região de interesse, *unwrapping* da fase e cálculo das correntes de *shim*. Esta foi desenvolvida em ambiente MATLAB.

Nos recém-nascidos o *shimming* deve ser aplicado numa região de interesse restrita ao cérebro devido à presença da interface ar/tecido no escalpe do bebê. Assim, a definição da região de interesse consistiu principalmente na aplicação de um limiar a fim de binarizar a imagem de magnitude, ajustada pelo utilizador. Em simultâneo foi implementada uma técnica de exclusão dos olhos com base na anatomia dos diferentes planos. No seu conjunto o método apresentou-se flexível de forma a ser ajustado ao sujeito em estudo. Quando aplicado com a mesma metodologia (limiar e exclusão de olhos) o volume incluído foi semelhante entre bebês.

O método de *shimming* foi avaliado com base em três medidas de dispersão do mapa de campo residual: largura a meia altura, desvio padrão dos pixéis no interior da região de interesse e o intervalo de frequências no interior do qual 95 % dos pixéis se encontravam. A utilização de diferentes medidas permitiu a avaliação do método em relação a diferentes aspetos. Este método foi aplicado a 52 participantes recém-nascidos com idade gestacional média de 39.8 ± 1.7 semanas.

O cálculo das correntes de *shim* permitiu gerar um campo magnético que melhorou a homogeneidade do campo B_0 no volume adquirido, sendo consistente com o previsto. Uma imagem média do campo residual foi calculada mostrando que existem duas regiões (occipital e pequenas regiões laterais) nas quais o campo magnético B_0 apresenta ainda heterogeneidades. Por fim, os resultados indicam que este método melhorou o campo perto da periferia do cérebro quando comparado com o método convencional disponibilizado no equipamento.

O *shimming* neonatal (*shimming* ótimo ou OIBS) foi utilizado como alicerce para a implementação de um método ajustado às características das aquisições fetais. Existem duas características principais que devem ser tidas em conta. Em primeiro lugar, os fetos encontram-se envoltos em líquido amniótico e tecido materno pelo que o ambiente no qual estão inseridos permite que a região de interesse seja definida de forma menos restrita. Em segundo lugar, o facto de a cabeça do feto ser pequena pode levar à existência de valores de corrente das bobinas de *shim* elevados. Essas correntes, principalmente associadas às bobinas de segunda ordem geram campos de magnitude elevada na região do tecido adiposo, o que altera a sua frequência de ressonância. Desta forma, as técnicas de supressão de gordura específicas em frequência são menos efetivas e a imagem de EPI apresenta artefactos.

Assim, a ferramenta para *shimming* fetal incluiu a definição de uma região de interesse cilíndrica e um método de *shimming* baseado em imagem com limites lineares (*shimming* limitado ou CIBS) impostos com base na frequência de ressonância do tecido adiposo. O CIBS consistiu na aplicação de limites superiores e inferiores ($[-300\ 100]$ Hz) para a frequência dos pixéis pertencentes à gordura após a aplicação do *shimming*.

Adicionalmente, o impulso de radiofrequência utilizado para a supressão de gordura foi estudado a fim de otimizar para a sua utilização no contexto do *shimming* fetal. Para o estudo dos parâmetros do impulso de radiofrequência, os rins de dois voluntários adultos saudáveis foram utilizados como simulação do ambiente fetal, devido às semelhanças entre a localização e interface entre tecidos.

Os métodos OIBS e CIBS foram aplicados em 6 grávidas saudáveis com idades gestacional média de 28 ± 6 semanas. Os mapas de campo residuais mostraram que as técnicas eram semelhantes em termos de homogeneidade no interior da região de interesse definida como cérebro, mas a segunda (CIBS) apresentou melhores resultados na supressão de gordura.

Como estudo do impulso de radiofrequência foi demonstrado que o desvio do impulso em cerca de 100 Hz no sentido da frequência de ressonância da água melhoraria a supressão de gordura sem detrimento do sinal da água. A utilização do novo método CIBS em simultâneo com um impulso de radiofrequência otimizado mostrou ser a melhor solução para homogeneizar o campo e suprimir a gordura.

Em conclusão, as ferramentas apresentadas permitiram melhorar a qualidade das imagens de EPI da cabeça do feto e do recém-nascido no contexto do *Developing Human Connectome Project*. O *shimming* neonatal mostrou ser um método consistente que pode facilmente ser utilizado por parte da equipa clínica. A nível fetal foi apresentado um método que demonstra a capacidade de superar as limitações demonstradas pelas técnicas convencionais.

Palavras-passe: Imagem eco-planar, *shimming* baseado em imagem, fetal, recém-nascidos.

Acknowledgements

I wish to express my sincere gratitude to my supervisor, Dr Anthony Price, for all the help, patience and guidance during the project. This journey would not be possible without your support. I also would like to thank Dr Rita Nunes for her friendship, advise and help. She has been a support since I first started to work in magnetic resonance imaging as an undergraduate.

Many thanks to my work colleges at the Centre for the Developing Brain Giulio Ferrazi, Rui Teixeira, Dr. Emer Hugher and other fellows for all the valuable assistance and suggestions. You make this office a great place to work. I also thank Dr Jo Hajnal for the support and financial assistance of my research.

Many thanks to my fellow graduate students Ana Moital and Carina Mendes, without whom the last five years would have been more difficult. You assisted me in every situation I needed.

I'm very thankful to my parents and sister who believed in me and always encouraged my dreams. And finally, to Diogo Duarte who always cheer me up and stood by me when I needed.

Contents

Abstract	i
Resumo	iii
Acknowledgements	vi
Contents	vii
List of Figures	x
List of Tables	xiv
List of Acronyms	xv
1 Introduction	1
2 MRI and B_0 field inhomogeneity	3
2.1 Introduction	3
2.2 MRI overview	3
2.2.1 Theoretical principles	3
2.2.2 Scanner system	5
2.2.3 MR signal sampling	6
2.2.4 Echo planar imaging	7
2.2.5 Chemical shift and lipid suppression	9
2.3 B_0 field inhomogeneity	10
2.3.1 Theory	10
2.3.2 B_0 field mapping	11
2.3.3 Correct for B_0 field inhomogeneities: Shimming	12
2.3.3.1 Active shimming - Automatic methods	15
2.3.3.1.1 Projection-based shimming	15
2.3.3.1.2 Image-based shimming	15
2.3.3.1.3 Alternative approaches	18

3	Verification of shim coil and B_0 field map coordinate information	20
3.1	Introduction	20
3.2	Methods	21
3.2.1	Shim coil verification	21
3.2.2	B_0 field map coordinate information	22
3.3	Results	22
3.3.1	Shim coil verification	22
3.3.2	B_0 field map coordinate information	25
3.4	Discussion	27
4	Development of a neonatal image-based shimming tool	29
4.1	Introduction	29
4.2	Methods	30
4.2.1	Data acquisition and Shim evaluation	30
4.2.2	Image-based shimming tool adapted to neonatal brain	31
4.2.2.1	Region of interest	31
4.2.2.2	Phase unwrapping	35
4.2.2.3	Shim calculation	35
4.2.2.4	Reconstruction and Export	36
4.2.3	Shimming graphical interface	36
4.2.4	Fat suppression - Neonatal head	37
4.3	Results	38
4.3.1	Optimization algorithm	38
4.3.2	B_0 homogeneity	39
4.3.3	IBS vs PB	41
4.3.4	Neonatal brain EPI	44
4.3.5	Fat suppression - Neonatal head	45
4.4	Discussion	49
5	Development of foetal image-based shimming tool optimized for efficient fat suppression	52
5.1	Introduction	52
5.2	Methods	53
5.2.1	Data acquisition	53
5.2.2	Fat suppression	53
5.2.3	Image-based shimming adapted to the foetal brain	54
5.3	Results	56
5.3.1	B_0 -map homogeneity	56

5.3.2	Fat suppression and EPI imaging	57
5.3.2.1	Fat suppression - Kidney testing	58
5.3.2.2	Fat suppression - Foetal EPI	62
5.4	Discussion	66
6	Summary and Future work	69
	References	71
	Appendix A Coil verification graphs.	76
	Appendix B Regularization	81

List of Figures

Figure 2.1	Schematics of scan system with patient table.	5
Figure 2.2	Spherical and Cartesian coordinates according with scan coordinate system.	6
Figure 2.3	Scheme of k-space filling trajectory.	7
Figure 2.4	Gradient-echo of EPI sequence representation.	8
Figure 2.5	Simulation of the deformation due to magnetic susceptibility of a foetal brain.	9
Figure 2.6	Magnetic field generated by linear shim coils.	13
Figure 2.7	Magnetic field generated by second order shim coils.	14
Figure 2.8	Shim coil designs for all first and second order spherical harmonics.	14
Figure 2.9	L-curve. The increase of λ leads to higher residual norm $\ A\mathbf{s}_\lambda - \mathbf{b}\ $ and lower solution norm $\ \mathbf{s}_\lambda\ $. The optimal λ value is found in the corner of the curve.	18
Figure 3.1	Calibration plots of Y coil	23
Figure 3.2	Coronal plane of residual B_0 field map of a phantom displaced 40 mm from isocentre in z direction.	25
Figure 3.3	Simulated field generated by the difference of shim values between shims 1 and 2 of figure 3.2.	25
Figure 3.4	Coronal plane of residual B_0 field map of a phantom displaced 40 mm from isocentre in z direction and angulation of the imaging volume.	26
Figure 3.5	Coordinate information in xyz system of the slice presented in figure 3.4.	26
Figure 3.6	Simulated field generated by the difference of shim values between shims 1 and 2 of figure 3.4.	26
Figure 4.1	Flow chart of the image-based shimming tool.	30
Figure 4.2	Magnitude B_0 field map in the coronal and sagittal planes with definition of the region to be excluded from the ROI.	32
Figure 4.3	Magnitude B_0 - map sagittal plane with region excluded.	33
Figure 4.4	T2 weighted image in sagittal plane and representation of the eye exclusion region.	33
Figure 4.5	Interface with eye exclusion.	34

Figure 4.6	3D ROI definition based on the three planes.	35
Figure 4.7	Main magnetic field within the ROI defined for all slices. The B_0 field map measured before shimming (at the left) and predicted after shimming (at the right) for 14 slices. Slices with blue border were the ones included in the optimization. Shim values for this example are presented at the left. The scale is presented at the bottom (-200 to 200 Hz).	37
Figure 4.8	Envelope of the SPIR rf pulse.	37
Figure 4.9	Simulation of the 95% interval in Hz of the B_0 map if the shim values calculated with different regularization parameter (λ) values are applied after translation in $-x$ (RL) and $-y$ (PA) directions. Translation of 1, 2 and 3 pixels correspondent to 2.65, 5.25 and 7.87 mm.	38
Figure 4.10	Box plot of FWHM of B_0 field maps without shim and measured and predicted residual B_0 map after shim.	39
Figure 4.11	Box plot of standard deviation (SD) of B_0 field maps without shim, and predicted and measured residual B_0 field map after IBS.	40
Figure 4.12	Box plot of 95 % interval of B_0 field maps without shim, and predicted and measured residual B_0 field map after image-base shimming (IBS).	40
Figure 4.13	Characterization of the main field in the brain after applying IBS tool and respective structural images	41
Figure 4.14	Mean \pm SD of shim values applied with PB and IBS.	42
Figure 4.15	Box plot FWHM of the residual B_0 field map when applying IBS and PB volume.	42
Figure 4.16	Box plot SD of the residual B_0 field map when applying IBS and PB volume.	42
Figure 4.17	Box plot of the 95% interval of the residual B_0 field map when applying IBS and PB volume.	43
Figure 4.18	Example of comparison between IBS and PB volume results in terms of field inhomogeneity in Hz.	43
Figure 4.19	Effects of low field inhomogeneities in EPI.	44
Figure 4.20	Effects of high field inhomogeneities in EPI fMRI.	45
Figure 4.21	Anatomical image with brain's region of interest	45
Figure 4.22	Head B_0 field maps before and after image-based shimming (IBS) in Hz.	46
Figure 4.23	Histograms of brain (black) and outside brain (red) regions.	46
Figure 4.24	Head B_0 field maps before and after image-based shimming (IBS) in Hz.	47
Figure 4.25	Chemical shift in the phase encoding direction of single-shot EPI of an adult head.	48
Figure 4.26	Effect of saturation pulse frequency offset on brain signal intensity with fat histogram.	48

Figure 5.1	Histogram of maternal fat and foetal brain regions of B_0 field map of a pregnant volunteer.	54
Figure 5.2	Schematics of the two methods available in the shimming tool for foetal imaging: optimal IBS (O-IBS) and constrained (C-IBS).	55
Figure 5.3	Box plot of measures of dispersion within the foetal brain ROI (N=6).	57
Figure 5.4	Effect of SPIR and shim application in abdomen EPI.	58
Figure 5.5	Torso B_0 field map before and after image-based shimming (O-IBS) in Hz.	59
Figure 5.6	Effect of fat saturation pulse frequency offset on the kidney signal intensity when applying O-IBS.	60
Figure 5.7	First slice of the B_0 field map measured pre and post O-IBS of the left kidney.	61
Figure 5.8	EPI images of the abdomen (kidney level) after applying different saturation pulse settings when applying O-IBS.	62
Figure 5.9	Histogram of the pixels in fat and foetal brain.	63
Figure 5.10	EPI with different shim methods O-IBS, C-IBS and Auto.	63
Figure 5.11	B_0 map of a foetal acquisition predicted using the optimal IBS (O-IBS) and the constrained IBS (C-IBS).	64
Figure 5.12	Foetal EPI with different shim methods O-IBS, C-IBS while varying the saturation pulse frequency offset.	65
Figure 5.13	Foetal EPI images of one volunteer. EPI acquired with O-IBS and C-IBS were applied with default and optimized SPIR offset (shift of 220 Hz).	66
Figure A.1	Calibration plots of X coil	76
Figure A.2	Calibration plots of Y coil	77
Figure A.3	Calibration plots of Z coil	77
Figure A.4	Calibration plots of Z^2 coil	78
Figure A.5	Calibration plots of ZX coil	78
Figure A.6	Calibration plots of ZY coil	79
Figure A.7	Calibration plots of X^2Y^2 coil	79
Figure A.8	Calibration plots of $2XY$ coil	80
Figure B.1	Simulation of the standard deviation and 95% interval in Hz of the B_0 map if the shim values calculated with different regularization parameter (λ) values are applied after translation in $+x$ (towards the right) and $+y$ (towards posterior) directions. Translation of 1, 2 and 3 pixels correspondent to 2.65, 5.25 and 7.87 mm. Measures presented are the mean of 10 neonatal datasets, and vertical bars represent the SD for each λ	81

Figure B.2 Simulation of the standard deviation and 95% interval in Hz of the B_0 map if the shim values calculated with different regularization parameter (λ) values are applied after translation in -x (RL) and -y (PA) directions. Translation of 1, 2 and 3 pixels correspondent to 2.65, 5.25 and 7.87 mm. 82

Figure B.3 Simulation of the standard deviation and 95% interval in Hz of the B_0 map if the shim values calculated with different regularization parameter (λ) values are applied after rotation in $+\theta_z$ and $-\theta_z$ directions. Rotation of 1, 5 and 10 degrees. 83

Figure B.4 Simulation of the standard deviation and 95% interval in Hz of the B_0 map if the shim values calculated with different regularization parameter (λ) values are applied after translation in dz and $-dz$ directions. Translation of 1 pixel correspondent to 6 mm. 84

List of Tables

Table 2.1	Spherical harmonics where l is order and m degree.	13
Table 3.1	MR scanner and RAF coordinate systems	21
Table 3.2	Shim slope verification including all spherical harmonics in the fit.	24
Table 3.3	Shim slope verification including shim + F0. F0 is a constant that corresponds to the frequency offset with nominal B_0 value at 3 T (~ 128 MHz).	24
Table 5.1	Dispersion measures within the foetal brain ROI.	57
Table 5.2	Dispersion measures within within three slices of the foetal brain ROI example.	64

List of Acronyms

AP Anterior-Posterior.

BOLD Blood-Oxygenation-Level-Dependent.

C-IBS Constraint Image-based shimming.

dHCP The Developing Human Connectome Project.

DSU Dynamic shim updating.

EPI Echo Planar Imaging.

ETL Echo Train Length.

FAST(EST)MAP Fast, Automatic Shim Technique using Echo-planar Signal readout for Mapping Along Projections.

FASTMAP Fast Automatic Shimming Technique by Mapping Along Projections.

FH Feet-Head.

FLATNESS Five Linear Acquisitions for up to Third-order, Noniterative, Efficient Slice Shimming.

fMRI functional Magnetic Resonance Imaging.

FOV Field-of-view.

FWHM Full Width at Half Maximum.

GRE Gradient-echo.

MRI Magnetic Resonance Imaging.

O-IBS Optimal Image-based shimming.

ppm parts-per-million.

RAF Right, Left, Feet.

rf Radiofrequency.

RL Right-Left.

ROI Region Of Interest.

ROLI Region Of Less Interest.

SD Standard Deviation.

SPIR Spectral Presaturation with Inversion Recovery.

SVD Singular-Value Decomposition.

TE Echo Time.

TR Repetition time.

Chapter 1

Introduction

There is growing interest in the use of imaging to study both structure and function in the developing brain. The Developing Human Connectome Project (dHCP) aims to make major scientific progress by creating the first 4-dimensional connectome of early life (from 20 to 44 weeks post-conceptual age). In order to create a dynamic map of human brain connectivity in foetal and neonate infants it is key to apply functional and diffusion imaging.

Echo planar imaging (EPI) is the main acquisition technique applied in functional and diffusion imaging. It allows fast acquisition of spatial information enabling volumetric coverage of the whole brain [1]. Fast acquisition methods are required to cope with the temporal resolution needed to: 1. map spontaneous fluctuation in brain activity in resting state functional imaging; and 2. have a good directional resolution in diffusion imaging [2].

Nevertheless, the EPI technique is associated with susceptibility artefacts, namely geometric distortion and signal loss, due to lower encoding bandwidth in the phase direction. In order to minimize those artefacts it is necessary to maintain a homogeneous main magnetic field B_0 .

Shimming methods made available by the manufacturer are fast but have two main disadvantages in the context of neonatal and foetal acquisitions. First, in order to be fast, the field mapping is based on projections which can increase error in regions with high field variation. In addition, mapping by projections implies the definition of a cuboid region of interest which is not anatomical adapted, leaving some areas outside the optimization. Second, because the only parameter available to the user is a cuboid region of interest, it is not possible to have control over the shimming process or predict the outcome before the acquisition. For foetal shimming these methods have one further disadvantage: shimming small areas like foetus' brain can be linked with high shim values that change the frequency of the abdominal fat, which hinders fat suppression efficiency. EPI acquisitions are sensitive to the frequency difference found between fat tissue and water in a way that fat tissue appears misregistered in the image and fat suppression is essential to limit that artefact. Therefore, it is important to implement a shimming

method that accounts for its effect on fat frequency, in addition to fat suppression optimization.

The main objective of this project was to develop an image-based shimming tool to optimize the magnetic field in the context of EPI images applied to neonatal and foetal brain, that overcome those deficiencies. The project has three specific objectives:

1. To verify the magnetic field created by first and second order shim coils and B_0 map coordinate information (Chapter 3);
2. To develop and apply a tool which integrates region of interest (ROI) definition, phase unwrapping and shim calculation for neonatal brain (Chapter 4);
3. To develop and apply a tool for image-based shimming of the foetal brain optimized to also achieve efficient fat suppression (Chapter 5).

Chapter 2 will introduce fundamental concepts associated with MRI, EPI and main magnetic field correction, as well as the state-of-art of shimming methods.

Chapter 2

MRI and B_0 field inhomogeneity

2.1 Introduction

Magnetic Resonance Imaging (MRI) is an imaging technique with a growing importance in neuroscience [3]. The complexity of the principles involved in the acquisition is associated with a high degree of flexibility in terms of the information that can be retrieved from a biologic system. Nevertheless, as the acquisition and reconstruction methods get more elaborated, additional challenges emerge. The scope of this chapter is to introduce the principles of MRI needed in the context of this work, and describe the process of mapping and correction of main magnetic field inhomogeneities.

2.2 MRI overview

2.2.1 Theoretical principles

MRI is a non-ionizing technique that can obtain functional and anatomical information, by selectively exciting atomic nuclei.

When an electrically charged nucleus rotates, it generates a magnetic field perpendicular to the rotational trajectory, similarly to the effect observed when current flows through a coil. Hydrogen atoms behave like small magnets with a bipolar magnetic moment. Spinning protons can also be referred to as spins and the direction of the spin magnetic moment vector is randomly distributed in the absence of external stimulus. However, if those nuclei are exposed to an external magnetic field B_0 applied in the z direction they will precess around it. The precession frequency (Larmor frequency ω_L in MHz) depends on the external field B_0 in Tesla (T):

$$\omega_L = \frac{\gamma B_0}{2\pi} \tag{2.1}$$

Where γ is the gyromagnetic ratio (Hz/T^{-1}). Nevertheless, the local effect of the external field is dependent on the molecular environment in which the spin is found. In living tissue the major contribution to the MR signal is H^1 in water, but the human body contains fat (mainly adipose tissue) that contributes for the signal measured as well. Hydrogen protons in fat and water are in different molecular environments. While water has two hydrogen atoms that have the same contribution, fat can have hydrogen atoms in different chain positions having different contribution to the local magnetic field [4]. The electrons that surround the nucleus and its interaction with the neighbourhood molecules determines the shielding effect to the magnetic field applied. The local magnetic field $B_{0,i}$ can be expressed as:

$$B_{0,i} = B_0(1 - \delta_i) \quad (2.2)$$

As a result protons in different molecules like water and fat will present different precession frequencies. This phenomenon is called chemical shift [5] and can be expressed in parts per million (ppm) relative to the main magnetic field resonant frequency. Water and fat ($[CH_2]_n$) have a shift of 3.3 to 3.5 ppm according with fat chemical composition, with the major peak at 3.35 ppm which corresponds approximately to 430 Hz at 3 T [6].

When a static B_0 field is applied, the individual nuclei precess resulting in net magnetization (M_0 in equilibrium) parallel to B_0 . Magnetization in this direction is longitudinal magnetization (M_z).

In order to get information about an object in MR it is necessary to induce a perturbation to that equilibrium. A second magnetic field B_1 in a form of a radiofrequency pulse (rf) can be employed to change the net magnetization. If an rf pulse is applied with an orientation perpendicular to the main field, the protons with frequencies within the frequency range of the pulse will absorb its energy. As a result, the magnetization M_z rotates from the equilibrium position to the transverse plane (90 pulse), resulting in a transverse magnetization component (M_{xy}).

When the rf pulse terminates, the M_{xy} decays due to loss of phase coherence between nuclei. Loss of phase coherence results from magnetic field variations due to spin-spin or B_0 inhomogeneities. Subsequently protons realign with B_0 emitting radiation at the same Larmor frequency which induces currents in the receiving coils.

According to the Bloch equations M_{xy} decay due to spin-spin interactions is represented by a negative exponential function with time constant T_2 .

$$M_{xy} = M_0 e^{-t/T_2} \quad (2.3)$$

Taking into account the contribution of B_0 field heterogeneities for this decay (T_2'), it is possible to represent the overall transverse relaxation time T_2^* as:

$$\frac{1}{T_2^*} = \frac{1}{T_2} + \frac{1}{T_2'} \quad (2.4)$$

Recovery of M_z after a 90 rf pulse cessation is also exponential but positive, and the longitudinal relaxation time is T_1 :

$$M_z = M_0(1 - e^{-t/T_1}) \quad (2.5)$$

2.2.2 Scanner system

The scan system is composed by a set of components which includes a main magnet, a set of room temperature coils (shim, gradient and RF coils) and a spectrometer(Figure 2.1)[7].

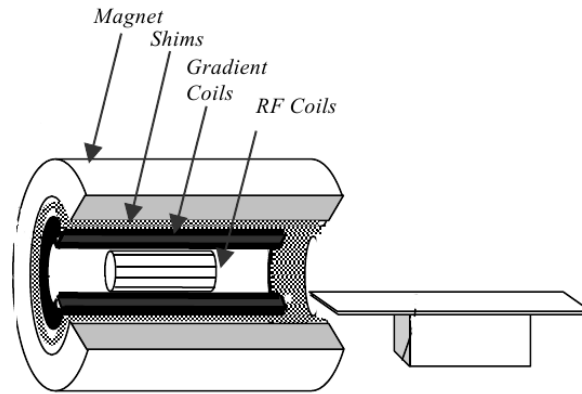


Figure 2.1: Schematics of scan system with patient table. Adapted from: Lvovsky Y, 2013 [8].

The main magnet is a superconducting system which is responsible for producing a uniform magnetic field of strength B_0 . Shim coils are the ones closest to the main magnet and are used to improve homogeneity of the main magnetic field [7].

Gradient coils are included inside the shim coil set and generate the linear field variations along x, y and z. Application of linear magnetic field gradient in one direction will change the Larmor frequency along that axis. This allows to localize signal contributions from different positions along the slice and phase/frequency encoding directions. The spatial representation of the imaged object can be done in various coordinate systems according to the objective. Coordinate systems can be classified in image-based and fixed coordinate systems. The first is linked with the image and depends on acquisition factors like the angulation of the imaging volume relative to the scan.

Within image-based systems the simplest system corresponds to the matrix index of each pixel in the image. The coordinate origin lies on the corner of the image and the units are pixels. One variant of matrix system considers the centre of the image as the origin.

On the other hand there are fixed coordinate systems which can be differentiated in patient or scanner coordinate system. In the first the system is defined according to patient anatomy and is expressed in anterior-posterior (AP), right-left (RL) and feet-head (FH), and is called as RAF system. In the scanner coordinate system all axes are linked with the scanner in a way that is independent of patient position or table movements. The origin is the scanner isocenter, z is parallel to the bore, x is upright and y is perpendicular to xy plan as depicted in figure 2.2 [7].

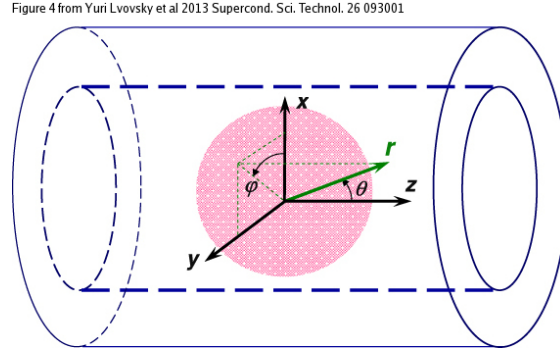


Figure 2.2: Spherical and Cartesian coordinates according with scan coordinate system. Adapted from: Lvovsky Y, 2013 [8].

Body transmitter coils are responsible for generating the rf pulse whereas the receiver coils detect the nuclear magnetic resonance signal close to the subject. This allows to maximize the strength of the signal recieved while transmitting a uniform B_1 field.

2.2.3 MR signal sampling

The MR signal received is sampled using an analog-to-digital converter. The time between samples is called dwell time (D), and should be small enough to correctly sample the frequency content of the signal. According with the Nyquist theorem the maximum frequency (ω_{NQ}) that can be accurately measured is half the sampling frequency. In the MR system the sampling frequency is known as the receiver bandwidth (BW_r) which is defined as the inverse of D . A high BW_r indicates that it is possible to accurately sample a large range of frequency components.

The readout bandwidth or BW_r can be defined as the range of spin frequencies in that direction within the FOV. This bandwidth is dependent on the gradient (G_r) and FOV (FOV_r) in that direction, according with [5]:

$$BW_r \simeq \frac{\gamma}{2\pi} \cdot G_r FOV_r \quad (2.6)$$

If the gradient applied increases then the range of frequencies for the same FOV will increase, i.e. the BW goes up. In opposition, if the FOV is smaller with the same gradient the BW is

smaller.

In a conventional spin warp acquisition, the phase-encode bandwidth BW_p can be approximated as the inverse of the phase encoding gradient duration. Nevertheless, if we consider other techniques using a train of gradient echoes for the same excitation, BW_p can be defined as [5]:

$$BW_p = \frac{1}{t_{ES} \cdot N_p} \quad (2.7)$$

Where t_{ES} is the echo spacing time, and N_p is the number of data points.

2.2.4 Echo planar imaging

EPI is a fast scanning technique that allows collecting 2D information following a single rf excitation. In fact, a 2D slice can be obtained in a time interval of the order of tens of milliseconds, making it possible to image the whole brain in 2-3 seconds [1]. This concept implies traversing all k-space before transverse magnetization totally decays (for brain ~ 100 msec) [5].

Gradients are responsible for k-space filling trajectory. In the conventional situation the gradient in readout direction is responsible for the progression over a line in k-space in each excitation, while phase gradient is applied immediately after the excitation to identify the line to be acquired. In opposite, EPI implies that gradients in the readout direction invert polarity along one excitation in order to change the direction in which a line in k-space is measured as shown in figure 2.3.

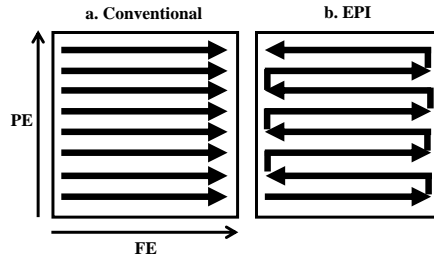


Figure 2.3: Scheme of k-space filling trajectory. The horizontal direction corresponds to the readout or frequency encoding (FE) direction and the vertical to the phase encoding direction (PE). In the conventional approach in **a.** one line is acquired after each excitation. In EPI in **b.** the gradients in phase direction are applied and reversed in FE direction in order to acquire multiple lines in one excitation.

In the past, phase encoding gradients were maintained constant along the acquisition, which resulted in a zigzag k-space trajectory. Nevertheless, the need to interpolate to Cartesian k-space points lead to artefacts. To avoid further k-space manipulation a brief phase gradient (blipped) is applied when the readout direction gradient ramp and data is not being acquired [9]. As a result, EPI produces a series of phase-encoded gradient echoes. The number of gradient echoes

after one rf excitation is the Echo Train Length (ETL) and the time between each line is the echo spacing (T_{ES}). Echoes acquired in each positive and negative lobe of the readout gradient have a different phase encode that corresponds to a different k-space line (Figure 2.4).

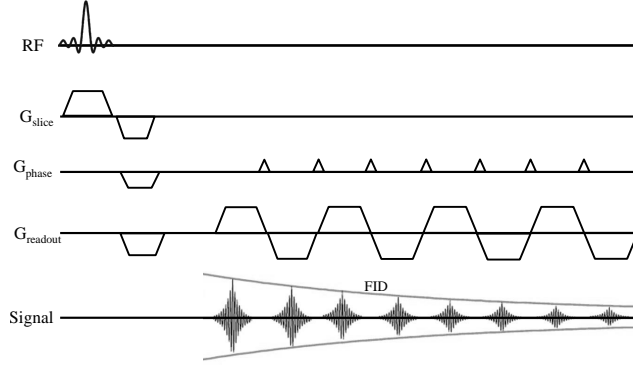


Figure 2.4: Gradient-echo of EPI sequence representation.

In order to maximize spatial resolution in the phase-encoding direction it is necessary to maximize ETL and minimize T_{ES} . Echo spacing is limited due to gradient slew rate, receiver bandwidth and matrix size in the readout direction [10], leading to a T_{ES} around 1 millisecond. This corresponds to a phase-encoding bandwidth of approximately 1 kHz. For readout direction the time between acquired points is dependent on the receiver bandwidth, resulting in a readout-encoding bandwidth of the order of 100 kHz. According to those values, each pixel in a 100×100 matrix has a bandwidth in the phase direction of the order of 10 Hz/pixel compared with 1 kHz/pixel in the readout direction. If the field deviation is of the order of 100 Hz the offset in phase direction will be of around 10 pixels.

Equation (2.8) represents signal induced in the receiver coil taking into account B_0 inhomogeneities (ΔB_0), where $\rho(x, y)$ is the proton density, x is the readout direction and y the phase direction [11, 12].

$$s(k_x, k_y) = \int_{xy} \rho(x, y) e^{i(k_x x + k_y y + \gamma \Delta B_0(x, y) t)} dx dy \quad (2.8)$$

As we can see in Equation (2.8) both read and phase direction are affected by magnetic field inhomogeneities, nevertheless longer time between sample points in the phase direction lead to higher phase accumulation [11, 13]. Those errors promote signal mismapping, causing image distortion and signal loss (Figure 2.5).

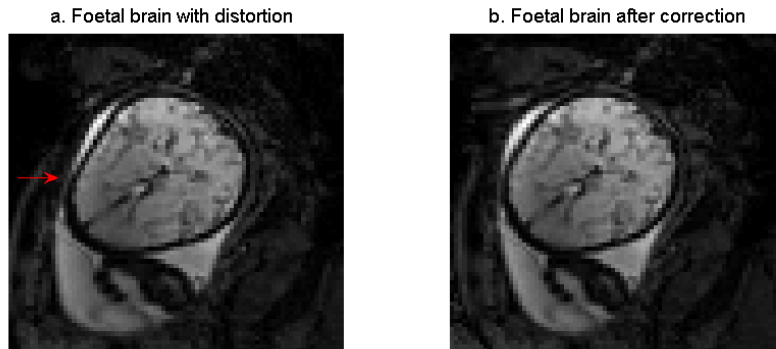


Figure 2.5: Simulation of image deformation due to magnetic susceptibility of a foetal brain. Courtesy of MSc Giulio Ferrazi

In multi-shot EPI (segmented EPI) the readout is divided into multiple segments. As a consequence spatial resolution is no longer limited by ETL. Data acquired in each segment is then combined before image reconstruction. Distortions are reduced but the overall acquisition takes more time [9], which increases motion sensitivity.

In gradient-echo EPI (GRE-EPI) each line is acquired at a different echo time (TE) and the echo that fills the central line corresponds to the effective TE, determining the T_2^* weighting contrast. This contrast is used in functional MRI (fMRI). Neuronal activation increases the blood flow and the oxygenation in that area prolonging T_2^* , and increasing the signal intensity in the activation area. This corresponds to the Blood-Oxygenation-Level-Dependent (BOLD) effect [5].

In spin echo EPI it is possible to reduce (or remove) T_2^* dependency by adjusting the effective TE in relation to the spin-echo TE. This allow a reduction of off-resonance effects and improvement of image quality, nevertheless spin-echo EPI has a reduced BOLD contrast.

2.2.5 Chemical shift and lipid suppression

Magnetic resonance imaging uses resonance frequencies for spatial encoding and is sensitive to off-resonance effects. According to equation 2.8 if the local resonance frequency of adjacent positions differs this will be reflected in a spatial shift in image domain i.e.chemical shift artefact. This effect takes special importance when the frequency difference is high relative to the bandwidth per pixel in a certain direction.

In conventional spin warp acquisition methods this displacement is present in the readout direction. The readout bandwidth is low because the time between points can be in the order of a dozen μs ($BW \sim 60 kHz$) [14, p. 113]. Regarding the phase encoding direction the acquisition of two adjacent lines is not continuous so in theory it would be possible to interrogate as many frequencies as we would want, leading to a higher BW_{PE} .

In opposition, EPI is not a spin-warp method in which the shift occurs in phase encoding

direction. As previously explained in the context of EPI the bandwidth in phase encoding direction is lower due to the continuous acquisition scheme. If we account for a $BW_{PE} = 1 \text{ kHz}$, a matrix of 64×64 pixels ($BW_{PE} = 16 \text{ Hz/pixel}$) and a chemical shift (Δf_{wf}) of 430 Hz (at 3 T), it is possible to calculate the water fat shift (WFS):

$$WFS = \frac{\Delta f_{wf}}{BW_{PE}/\text{pixel}} = \frac{430}{16} = 27 [\text{pixels}] \quad (2.9)$$

According with equation 2.9 the shift observed can be very high and contaminate regions where we aim to measure functional activity. For this reason, the application of lipid suppression techniques is imperative.

One common way to suppress fat is spectral fat saturation. In this method an rf pulse will tip fat spins to 90° , and a gradient is applied to spoil these spins. If only fat spins are dephased they will not contribute to the overall signal, and only water signal will be measured [15]. A method called Spectral Presaturation with Inversion Recovery (SPIR) uses a spectral selective rf pulse to invert only fat spins, tipping them by 180° . Afterwards, fat spins will suffer relaxation and at a given point will have an orientation perpendicular to the main magnetic field. At this moment, the MR sequence is initiated and fat does not contribute to the signal. Instead of 180° , a pulse that tips fat spins by $90^\circ + \delta$ (e.g. 105°) can be applied in order to reduce the time needed to start the imaging sequence. The spectral selective rf pulse can be characterized by its bandwidth, transition interval and frequency offset. Additionally, it is important to study the existence of B_1 inhomogeneities that could lead to incorrect fat suppression. Adiabatic rf pulses are independent of those inhomogeneities and can be used, mainly in the context of inversion [5].

2.3 B_0 field inhomogeneity

2.3.1 Theory

Main magnetic field (B_0) inhomogeneities can result from magnet imperfection or sample magnetic susceptibility effects. The sample distorts the magnetic field due to its geometric distribution of magnetic susceptibility (χ)[16, 17].

The induced magnetization \mathbf{M} by the applied auxiliary field \mathbf{H} in the context of MR can be expressed as:

$$\mathbf{M} = \chi \mathbf{H} \quad (2.10)$$

The magnetic potential ϕ_M taking into account that the object is nonconductive can be presented as:

$$\nabla \phi_M = -\mathbf{H} \quad (2.11)$$

In fact the susceptibility can be defined as the ratio M/H [18]. Magnetic susceptibility relates with the maximum field perturbation, in a way that if $\chi \gg 1$ can produce a field larger than the applied field. Nevertheless, in general MRI tissues have $\chi \ll 1$, as a consequence small perturbations are present, but due to the high sensitivity of some methods, these changes have to be corrected [18].

This distortion is greater in boundaries between low and high magnetic susceptibility tissues (aligned perpendicular to B_0 field) [19], local inhomogeneities (ΔB_0) in borders between two tissues can be expressed as:

$$\Delta \mathbf{B}_0 = \mathbf{B}_1 - \mathbf{B}_2 = (1 - \chi_1)\mu_0 \mathbf{H} - (1 - \chi_2)\mu_0 \mathbf{H} = (\chi_2 - \chi_1)\mathbf{B}_0 \quad (2.12)$$

Where χ_1 and χ_2 are the magnetic susceptibility of tissues 1 and 2, and \mathbf{H} is the auxiliary field.

One example is air-tissue boundaries found in temporal and frontal regions of the human brain, where $\chi_{air} = 0.3$ ppm and $-11.0 < \chi_{tissue} < -7.0$ ppm ($\chi_{water} \simeq 9.2$ ppm)[12]. In addition, this susceptibility distribution can vary across human subjects [12].

2.3.2 B_0 field mapping

In order to correct for field inhomogeneity it is necessary to map the B_0 magnetic field. Phase ϕ accumulated during a given period Δt can be described by:

$$\phi = \int \omega dt = \phi_0 + \omega \Delta t \quad (2.13)$$

Where ϕ_0 is the initial phase and ω is given by:

$$\omega = \gamma B_0 + \omega_{cs} + \gamma \Delta B_0 \quad (2.14)$$

In this expression B_0 is the static magnetic field, which can be excluded if the frame of reference is rotating, γ is the gyromagnetic ratio and ω_{cs} is the chemical shift. According to Schneider et al [20] the later can be ignored if we choose a Δt defined by the chemical shift frequency ν_F , i.e. $\Delta t = \frac{1}{\nu_F}$ [20]. Spins of fat and water will be in phase at multiples of that interval, and will contribute similarly to the measurement.

For a particular echo-time (TE), i.e. $\Delta t = TE$, equation (2.13) becomes:

$$\phi = \phi_0 + \gamma \Delta B_0 TE \quad (2.15)$$

In order to estimate ΔB_0 it is necessary to obtain the phase difference between at least two acquisitions at different TE values. Phase difference information constitutes the B_0 -map:

$$\begin{aligned} \Delta \phi(x, y, z) &= \phi_0 + \gamma \Delta B_0 TE_2 - (\phi_0 + \gamma \Delta B_0 TE_1) \\ &= \gamma \Delta B_0 (TE_2 - TE_1) \end{aligned} \quad (2.16)$$

Spatial variance of magnetic resonance is given by [12, 21]:

$$\Delta B_0(x, y, z) = \frac{\Delta\phi(x, y, z)}{\gamma(T E_2 - T E_1)} \quad (2.17)$$

Image acquisition for field map depends on phase calculation:

$$\phi = \tan^{-1} \left(\frac{\text{Im}[Image]}{\text{Re}[Image]} \right) \quad (2.18)$$

Measured phase signal difference can then only take values between $-\pi$ and π . Phase measured is the remainder after division between the original phase and 2π , leading to jumps near boundaries. As a consequence it is necessary to apply the inverse process, named unwrapping.

Magnetic field maps can be acquired through a standard gradient echo pulse sequence collecting at least two images using different TE. When using spin-echo sequences it is necessary to change the time between refocusing pulses and signal acquisition.

In the previous explanation only two echoes were presented. Inclusion of more than two phase images can increase the signal-to-noise ratio decreasing the error associated with the measurement. Nevertheless, it is important to maintain acquisition time in the range of a few minutes or less for breath-hold in order to enable automatic shimming application. Since the standard methods only include two scans Funai et al [22] studied suitable model alternatives that use more than two scans and then apply a regularized least-squares field map estimation method.

2.3.3 Correct for B_0 field inhomogeneities: Shimming

Shimming is a technique that allows optimizing magnetic field homogeneity. Passive shimming (ferroshimming) applies paramagnetic materials in order to distort the magnetic field and improve homogeneity [23]. Passive shimming has the limitation of not being easy to adapt to either individual characteristics or region of interest.

Active shimming corresponds to passing electrical currents in shim coils (superconductive or room temperature), allowing to reduce field inhomogeneities associated with the sample. Main magnet imperfections can be overcome with the use of passive-shimming, or applying sets of superconducting shimming coils, which allow to reduce the sample independent field inhomogeneities from 50 parts-per-million (ppm) to 1.5 ppm over defined diameter spherical volumes [12]. In this work we will focus on active shimming using room temperature coils [7]. The equation that governs the behaviour of the field in the bore of a superconducting magnet is:

$$\nabla^2 B_0 = 0 \quad (2.19)$$

The solution B_0 can be expressed in spherical coordinates as an expansion of spherical harmonics [12, 24]:

$$B_0(r, \phi, \theta) = \sum_{l=0}^{\infty} \sum_{m=-l}^l P_l^m(\cos \theta) r^l (A_{lm} \cos \phi + B_{lm} \sin \phi) \quad (2.20)$$

Where the $P_l^m(\cos \theta)$ are the Legendre polynomials, m is the degree and l is the order of the polynomial. In the Cartesian form equation (2.20) can be expressed as:

$$B_0(x, y, z) = \sum_{l=0} \eta_{lm} f_l^m(x, y, z) \quad (2.21)$$

With $f_l^m(x, y, z)$ denoting the magnetic field geometry corresponding to each spherical harmonic and η_{lm} the constant representing the contribution of each function (see Table 2.1).

Table 2.1: Spherical harmonics where l is order and m degree. Adapted from: Koch et al. 2009 [12].

l	m	Name	$f_l^m(x, y, z)$	$f_l^m(r, \theta, \phi)$
1	0	Z	z	$r \cos \theta$
1	1	X	x	$r \sin \theta \cos \phi$
1	-1	Y	y	$r \sin \theta \sin \phi$
2	0	Z^2	$z^2 - 0.5(x^2 + y^2)$	$\frac{1}{2}r^2(3 \cos^2 \theta - 1)$
2	1	ZX	zx	$r^2 \sin \theta \cos \theta \cos \phi$
2	-1	ZY	zy	$r^2 \sin \theta \cos \theta \sin \phi$
2	2	$X^2 - Y^2$	$x^2 - y^2$	$r^2 \sin^2 \theta \cos 2\phi$
2	-2	$2XY$	$2xy$	$r^2 \sin^2 \theta \sin 2\phi$

Spherical harmonics are orthogonal basis functions, and as a consequence each component can be applied through a shim coil. In fact, shim coils are designed to produce a magnetic field distribution that corresponds to each spherical harmonic function centred at the magnetic origin (see Figures 2.6 and 2.7) [25].

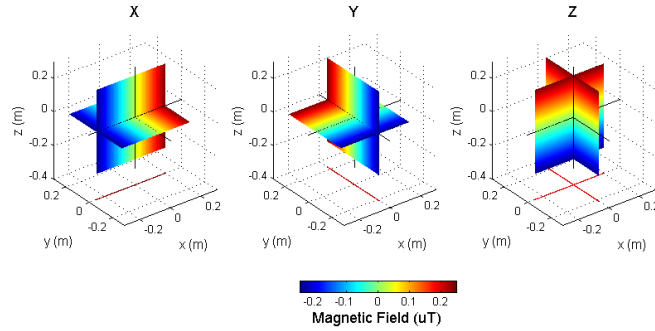


Figure 2.6: Magnetic field generated by linear shim coils.

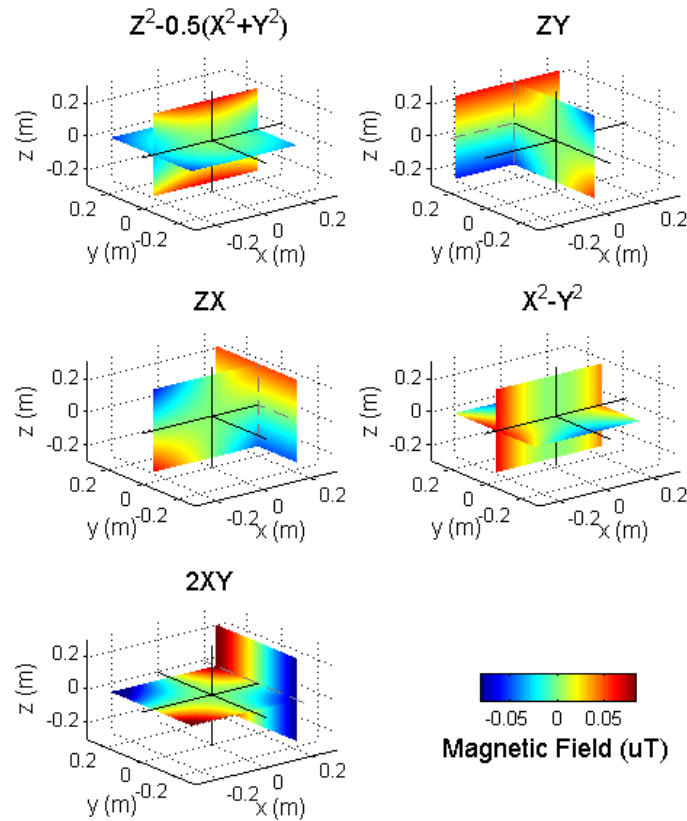


Figure 2.7: Magnetic field generated by second order shim coils.

Golay was the first to apply shim coils to generate orthogonal spherical harmonics by adjusting the respecting currents [26]. In theory, if it was possible to apply an infinite number of components it would be possible to perfectly compensate for all inhomogeneities. Shim coils designed for standard applications are presented in Figure 2.8.

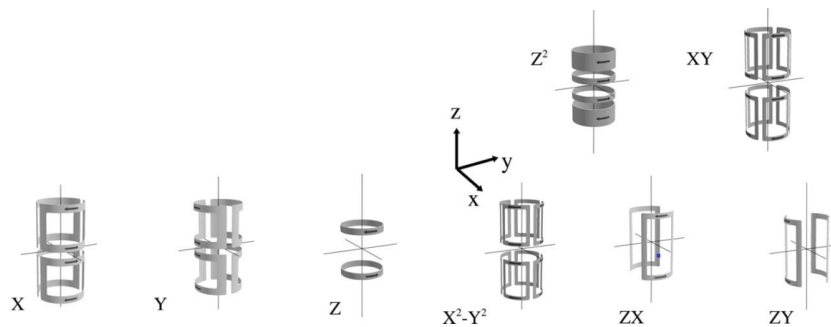


Figure 2.8: Shim coil designs for all first and second order spherical harmonics. Adapted from: Koch et al 2009 [12].

2.3.3.1 Active shimming - Automatic methods

Shimming consists of adjusting field gradients to obtain magnetic homogeneity [7]. As referred in section 2.3.3 active adjustment of field gradients implies finding optimized coil currents, represented by η_{lm} in equation (2.21). Manual approaches to find those currents do not allow finding optimal solution in a fast way and therefore it is important to implement automated techniques. Automated shim techniques can be differentiated in projection-base or image-based.

2.3.3.1.1 Projection-based shimming

Projection-based shimming was initially developed by Gruetter [25, 27], who implemented the fast automatic shimming technique by mapping along projections (FASTMAP). FASTMAP consists in mapping field homogeneity along 6 projections j ($j = xy, yx, zx, xz, zy, yz$), that cross the isocentre $r = 0$. The projections corresponds to bars of length L , with an orientation defined through the direction of orthogonal z, y and x gradients [27]. Using the spherical form of equation (2.21):

$$B_0(r, \phi, \theta) = \sum_{lm} \eta_{lm} r^l W_{lm}(\phi, \theta) \quad (2.22)$$

In this equation ϕ and θ are known for each projection, and coefficient W_{lm} is constant because it is a function of ϕ and θ . Each projection j is fitted to a polynomial regression of order l , obtaining the coefficients a_l^j in the model $a_0^j + a_1^j r + a_2^j r^2 + \dots + a_l^j r^l$.

Those are used to calculate the coefficient η_{lm} of each spherical harmonic:

$$\eta_{lm} = \frac{\sum_j a_l^j W_{lm}^j}{\sum_j (W_{lm}^j)^2} \quad (2.23)$$

This technique allows reducing time of field mapping and current calculation.

Additionally, variants of this algorithm have been applied, such as FASTERMAP (Fast, Automatic Shimming Technique with improved Efficiency and Reliability for Mapping Along Projections) [28], FLATNESS (Five Linear Acquisitions for up to Third-order, Noniterative, Efficient Slice Shimming) [29], or FAST(EST)MAP (Fast, Automatic Shim Technique using echo-planar signal readout for Mapping Along Projections) [30].

The major disadvantage of FASTMAP is its limitation to accurately map inhomogeneities over extended field areas, because field distribution along tissue borders changes abruptly [31]. Smaller volumes with heterogeneous regions, such as the human neonatal brain, also have rapid changes along borders which hinder FASTMAP efficiency.

2.3.3.1.2 Image-based shimming

Due to hardware improvements, it is currently possible to acquire three-dimensional field maps along a specific non squared ROI with detailed field information along tissue borders.

Image-based shimming enables fitting of the spherical harmonic model (ideal or measured) with all pixels included in the defined ROI in order to find the current intensity values that minimizes inhomogeneity. This is usually achieved through a least squares fit equation $\mathbf{A}\mathbf{s} = \Delta\mathbf{B}_0$:

$$\min_{\eta_{lm}} \sum_{p=1}^M \|\eta_{lm} f_l^m(x, y, z) - \Delta B_0(x_p, y_p, z_p)\|^2 = \|\mathbf{A}\mathbf{s} - \Delta\mathbf{B}_0\|^2 = \|\mathbf{A}\mathbf{s} - \mathbf{b}\|^2 \quad (2.24)$$

where $A \in \mathbb{R}^{k \times n}$ is the spatial distribution of n spherical harmonic fields in k positions, and \mathbf{s} its amplitude. The vectorial representation of $\Delta\mathbf{B}_0$ will be referred to as \mathbf{b} .

Previous works have implemented a global approach, because the whole region to be shimmed is included in the optimization problem [32, 33]. However, global shimming applied to the human brain can be limited because areas such as auditory and sinus cavities produce localized inhomogeneities which are difficult to compensate for without compromising other regions. Higher-order shim coils can be used to mitigate this problem, but their application is constrained by bore space and the Biot-Savart law (amplitude of magnetic field falls quadratically with distance from the coil). Localized methods that include smaller regions of interest, and based on anatomical characteristics have been applied with better results than rectangular regions [21, 34].

Nevertheless, inhomogeneities outside the ROI can affect image quality inside that region, especially in high-field MRI [35]. Fillmer et al. [36] developed a tool that included a ROI around which a region of less interest (ROLI) was defined. Both regions were included in the fit, but the ROLI was weighted. That allowed to control inhomogeneities in the vicinity of the ROI and avoid degeneracy due to small regions. They compared that method with the conventional optimization with only ROI and also standard FASTMAP. The fit with and without ROLI presented similar overall results with lower standard deviation when compared with FASTMAP, which indicates the importance of anatomically defined ROI. In addition, the authors mention less field variation at ROI edge when accounting the ROLI, which reduces image deformation.

The development of efficient image-based shimming algorithms has been an active area of research. In 1991 Schneider et al. [20] used an image-based shimming method applied to a single axial slice of the human brain to calculate the optimal linear shim coefficients. In the same year Webb et al applied chemical shift imaging using a least-square solver based on a QR factorization of A to calculate the optimal shim coefficients. Instead of applying the ideal spherical harmonic model they constructed a reference map over a volume sufficient to include any object that would be scanned. Such an approach can be used to quantify shim interaction in off-centre regions [32].

In 1995 Wen and Jaffer [33] implemented a third order shimming algorithm which included current constraints according with available current limits. The algorithm calculates shim currents through a least square method which iteratively set the currents within limits. The method achieved a reduction of at least 10 Hz in standard deviation of B_0 field of the selected ROIs,

when compared with the method with simple truncation.

The importance of constraining shim currents is not only related with the shim current hardware limits but also with the likelihood of an ill-conditioned solution. A well-posed problem corresponds to a problem for which a solution exists, is unique and stable. In the context of shimming calculations the problem is discrete, so the solution is not a continuous function of the data and small perturbations can lead to large perturbations in the solution and the solution is not unique. If the problem is ill-posed the solution has increased sensitivity to perturbations in \mathbf{A} or \mathbf{b} . This occurs when the number of polynomial coefficients increases and/or shimmed volume size decreases.

Considering \mathbf{e} the unknown error in \mathbf{b} , and $\hat{\mathbf{b}}$ the error free vector we can have:

$$\mathbf{b} = \hat{\mathbf{b}} + \mathbf{e} \quad (2.25)$$

Using the pseudoinverse of \mathbf{A} we want to find the approximate solution of $\hat{\mathbf{x}} = \mathbf{A}^\dagger \hat{\mathbf{b}}$, which is the minimal Euclidean norm of the linear system. This can be obtained by calculating the approximate solution of the least-squares problem including the error:

$$\mathbf{x} = \mathbf{A}^\dagger \mathbf{b} = \mathbf{A}^\dagger (\hat{\mathbf{b}} + \mathbf{e}) = \hat{\mathbf{x}} + \mathbf{A}^\dagger \mathbf{e} \quad (2.26)$$

According with equation 2.26 the existence of small errors \mathbf{e} will be propagated to the calculated solution [37]. In order to overcome this problem a regularization method is normally applied.

One type of regularization is the truncated singular-value decomposition (SVD) in which the smallest singular values are excluded reducing that effect. Kim et al. (2002) [38] used a modified version of the truncated SVD. They proposed a least-square solution using SVD in which singular values that contribute to high shim currents are truncated. This truncation is applied at the cost of residual norm $\|\mathbf{A}\mathbf{s} - \mathbf{b}\|_2$ increase. The idea is to create a stable solution that is independent of perturbations but also improves field homogeneity. They also suggest using a reference map \mathbf{M} instead of an ideal model \mathbf{A} .

One other example of regularization is the Tikhonov method [39]. This well known method consists in adding a stabilizing function weighted by a regularization parameter λ that allows to reduce the sensibility to perturbations in \mathbf{A} or \mathbf{b} . The solution x_λ (or s_λ) can be calculated according to:

$$\begin{aligned} \mathbf{x}_\lambda &= \min_{\mathbf{x} \in \mathbb{R}^n} \{ \|\mathbf{A}\mathbf{x} - \mathbf{b}\|^2 + \lambda \|\mathbf{x}\|^2 \} \\ &= \min \left\| \begin{pmatrix} \mathbf{A} \\ \lambda \mathbf{I}_n \end{pmatrix} \mathbf{x} - \begin{pmatrix} \mathbf{b} \\ 0 \end{pmatrix} \right\|^2 \end{aligned} \quad (2.27)$$

Where \mathbf{I}_n is the identity matrix of order n , and x_λ is the regularized solution. Parameter λ weights the minimization of the solution x relative to minimization of mean square error and should be dependent on the errors of \mathbf{b} and \mathbf{A} [40].

Kim's regularization shows good results in terms of decrease of solution norm per residual norm increase. Nevertheless Tikhonov is a method that allows continuous manipulation of the regularization parameter allowing a more subtle adaptation, whereas truncated SVD can only be applied in a discrete form. In fact, when applying Kim's approach the truncation of a singular value can lead to an increase the full width half maximum of the pixel frequency histogram from $9.3 \pm 0.8Hz$ to $14.0 \pm 0.7Hz$.

In order apply the regularization it is important to choose the right parameter value. In order to adapt the regularized parameter to the problem presented there are a number of options, namely L-curve [41] or generalized cross validation (GCV) [42]. L-curve is a plot of the size of the solution versus size of the least squared residual, for each parameter value λ (Figure 2.9).

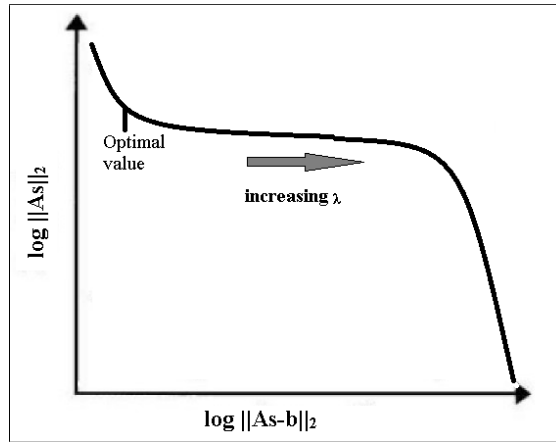


Figure 2.9: L-curve. The increase of λ leads to higher residual norm $\|As_\lambda - b\|$ and lower solution norm $\|s_\lambda\|$. The optimal λ value is found in the corner of the curve.

2.3.3.1.3 Alternative approaches

Alternative approaches include the application of shim coils in a localized manner. Dynamic shim updating (DSU) corresponds to updating shim settings during the acquisition for each slice or sub-volume [43]. Linear DSU was first applied in spectroscopy [44] and then by Blamire et al [45] to brain EPI imaging. High-order shim applied in this context was then added by de Graaf et al [46] to rat brain and Koch et al [43] applied to the human brain.

Usage of DSU implies additional hardware requirements - dedicated amplifier electronics - because this method implies rapid change of shim settings [31]. High-order DSU induces significant eddy-currents, which should be quantified in order to minimize additional field components through actively shielded coils or pulse pre-emphasis [47]. Another concern relates to DSU application to thin slices, because various three-dimensional spherical harmonic components can present the same form when projected in the plane. Those shim degeneracies can result in an ill-conditioned minimization problem that fails to converge. This problem can be approached

through the use of Kim's et al [38] regularization method previously referred to or including one slice on each side of the slice under study in order to optimize along a 3D slab. Nevertheless, the second approach may not be sufficient due to resolution limitations. Koch et al [43] present a third approach where they use a two-dimensional degeneracy analysis which allows to determine shim degeneracies in a slice specific manner. DSU characteristics imply additional complexity to the system and methods that may not overweight additional benefits from its application [47].

Recently, Balteau et al [48] implemented a shimming technique applied to fMRI, that maximizes BOLD sensitivity locally. BOLD sensitivity was estimated according to EPI parameters and the result compared with Kim et al approach [38] showing an increase of sensitivity to the activation. Nevertheless, the authors mentioned that BOLD sensitivity based shimming method should not be used in high resolution fMRI if image distortion correction is not used.

Chapter 3

Verification of shim coil and B_0 field map coordinate information

3.1 Introduction

Shim coils are responsible for creating a magnetic field variable in space according with a specific geometry (Section 1). The design of such coils started in 1958 with Golay, who developed a new set of coils based on spherical harmonics [26]. Then Romeo et al developed the mathematical framework and principles for field mapping that allowed to improve coil design which currently govern high order coil patterns [49]. Although the foundation for coil design has been developed more than 20 years ago, the creation of methods that allow to improve coil efficiency and accuracy in terms of field generation continues to be an area of interest.

Design of shim coils involves optimization over the field across a defined volume that should be large in order to be correctly applied over an extended space where the object/subject is. The field created by a specific coil is proportionally linear to the current applied to that same coil across the volume defined. According with the theory described in section 2.3.3 each coil is created to produce a field that corresponds to one of the spherical harmonics functions. This principle is the basis of the active shimming because magnetic field correction depends on the combination of harmonics [49].

The existence of coil imperfections due to manufacture or relative positioning of the coils can decrease the accuracy of the generated field [50]. As a result, in addition to the field intended, small field components are also generated. Those components contaminate the field and create cross terms across the spherical harmonics. Characterization of field imperfections and non-orthogonality between shim terms is critical to quantify experimental errors in shimming [47].

In order to create a correct correspondence between the model of the shim terms and the field created by each shim coil it is important to have access to coordinate information of the

region being imaged. As stated in section 2.2 the spatial representation can be displayed in two types of coordinate systems. In the context of shim term calculation based on spherical harmonic functions the coordinate system fixed to the scanner is the one that allows to simulate the field generated by the coils. Nevertheless, field information obtained from B_0 mapping is exported according to patient position (i.e. RAF) and therefore has to be transformed into scanner coordinates.

Patient position in Z direction can be described as feet-first (FFp) or head-first (HFp), while position in the xy plane can be described as supine, prone, right or left according with the anterior direction. In the present work the patient position is always supine, but the z direction can be FFp for foetal or HFp for neonatal scan. Differences between both systems directions are presented in table 3.1.

Table 3.1: MR scanner and RAF coordinate systems correspondence in: head-first position (HFp) and feet-first position (FFp).

MR system	RAF system	
	HFp Supine	FFp Supine
x	PA	PA
y	RL	LR
z	FH	HF

At the beginning of each scan the table position is calibrated and positioned in the scanner isocentre ($z = 0$ mm). For neonatal imaging the acquisition is held without need to readjust baby's head location, table movement or volume shift, as a consequence coordinate information extracted from acquisition can be used to fit spherical harmonic.

Nevertheless, for foetal imaging it is necessary to locate position and orientation of foetus in order to adjust the selected volume relative to isocenter. This adjustment can involve table movement which corresponds to a shift between the patient and the scanner coordinate systems.

In order to correctly apply active shimming it is important to verify that all conditions are fulfilled. This chapter presents the study of two parts of the shimming process. First, intends to evaluate the accuracy of the fields generated by first and second order shim coils. The second part is the correction of the effect of table movement in coordinate information.

3.2 Methods

3.2.1 Shim coil verification

In order to verify the magnetic field produced by each shim coil a spherical phantom $15 \times 15 \times 15$ cm³ containing physiologic saline water was used, and a 3D B_0 field map with matrix

$128 \times 128 \times 70$ was acquired. For each shim a set of N known values in the scanner (setting values) was applied. For each setting a B_0 field map was acquired which after subtracting the baseline B_0 -map (without shim) was used to fit the spherical harmonic model. This model included all model components in order to verify interaction between shims. A linear regression analysis was performed using the plot setting values vs model values.

3.2.2 B_0 field map coordinate information

Magnetic field mapping was done by applying a rf spoiled gradient echo sequence T_1 fast field echo (T_1 FFE). Data was exported in the PAR/REC format used by Philips. This format is composed of two files, a *.PAR file in which meta-information is listed and the a *.REC file where the image data can be found. B_0 -maps were read from PAR/REC format in order to obtain both imaging (phase and magnitude) and respective coordinate information (from *.PAR file).

In order to calculate the image coordinates in the MR system (xyz) a translation followed by rotation in each direction (FH, RL and AP) were applied.

Because the table movement changes the relation between FH direction and Z in the MR scanner system it is important to take into account movements that happen after calibration. Therefore in order to transform into MR coordinate system it was important to take into account two aspects: the relation between both systems (Table 3.1) and the table movement. According with the patient FFp or HFp, the relations in Table 3.1 were applied. Additionally, table position in relation to isocentre in z direction at the moment of B_0 field map acquisition was exported. That value was summed in HFp and subtracted in FFp after applying the rotation and translation aforementioned.

These transformations were tested in a fathom in two situations. First, the phantom was positioned in HFp and the scanner table was moved. Second, the object was positioned in FFp with angulation of the imaging volume and the table was displaced. In both conditions, a B_0 was acquired and the IBS was applied. For each situation the shim values were calculated two times: Shim 1 not taking the offset into account; and Shim 2 which included the z offset. For each Shim 1 and 2 a residual B_0 field map was simulated. Finally, Shim 2 was used in the acquisition of a measured residual B_0 field map to verify the accuracy of the method.

3.3 Results

3.3.1 Shim coil verification

Taking into account the errors in B_0 -map and spherical harmonic model fit, it was possible to find an error in the order of $1 \times 10^{-4} \text{ mT/m}$ (0.033 ppm/m) for first order and $1 \times 10^{-4} \text{ mT/m}^2$ (0.033 ppm/m^2) for second order shim calculation. B_0 -map errors were estimated based

on the noise outside the phantom [7]. Spherical harmonic model fit was estimated through shim coefficients standard error. After linear regression it was calculated a maximum standard error of 1×10^{-3} for slope coefficients.

For each spherical harmonic it was drawn a graph with the slope as it is presented in figure 3.1 for Y shim coil setting as example. Graphs for all coils tested are presented in Appendix A, figures A.1 to A.8.

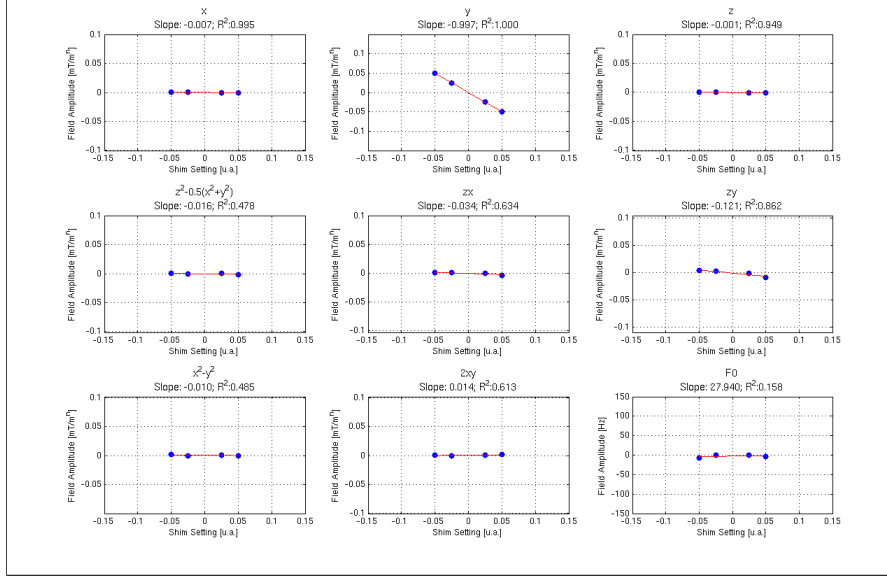


Figure 3.1: Calibration plots of Y coil after applying four known shim setting values. The maximum error of the field amplitude for all points was estimated in $1 \times 10^{-4} \text{ mT}/\text{m}^n$.

The results of this verification are presented in Table 3.2. The slope is negative in order to null inhomogeneities applying the same function but with inverse signal. A slope close to -1 was observed for all shims and all linear regressions showed a coefficient of determination (R^2) of 1.

Additionally, a fit that only included each corresponding shim was applied. The result is presented in Table 3.3 with respective coefficients of determination.

Table 3.2: Shim slope verification including all spherical harmonics in the fit.

	X	Y	Z	Z2	ZX	ZY	X2Y2	2XY
X	-0.994	-0.007	0.000	-0.001	0.000	0.000	0.000	0.002
Y	-0.006	-0.997	-0.002	-0.001	0.000	-0.007	-0.001	0.000
Z	0.000	-0.001	-0.979	0.000	0.000	-0.008	0.000	0.000
Z2	0.039	-0.016	-0.073	-1.028	-0.002	0.002	0.000	0.014
ZX	-0.083	-0.034	-0.068	-0.004	-0.998	0.000	0.000	0.001
ZY	0.007	0.000	-0.001	-0.002	-0.010	-1.014	0.000	-0.002
X2Y2	0.009	-0.010	-0.042	-0.005	-0.002	0.002	-1.039	0.001
2XY	-0.036	0.014	0.006	0.024	-0.001	0.003	-0.009	-0.983
Range [mT/m^n]	[-0.25, 0.25]	[-0.05, 0.05]	[-0.05, 0.05]	[-1,1]	[-0.75, 1]	[-2.5, 2.5]	[-1, 1]	[-1, 1]
N Points	4	4	4	8	5	10	8	6

Table 3.3: Shim slope verification including shim + F0. F0 is a constant that corresponds to the frequency offset with nominal B_0 value at 3 T (~ 128 MHz).

Shim	X	Y	Z	Z2	ZX	ZY	X2Y2	2XY
slope	-0.994	-0.995	-0.979	-1.022	-0.993	-1.016	-1.036	-0.981
R^2	1.000	1.000	1.000	1.000	1.000	1.000	1.000	1.000

3.3.2 B_0 field map coordinate information

Figure 3.2 presents the residual B_0 field maps when the calibrated object centre has an offset in FH direction (z direction) related to scanner isocentre in the HFp.

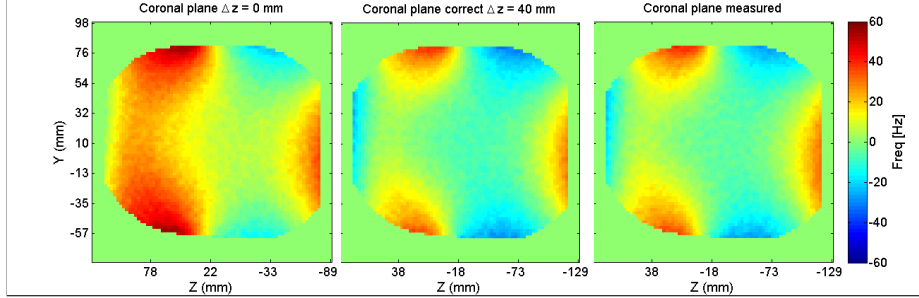


Figure 3.2: Coronal plane of residual B_0 field map of a phantom displaced 40 mm from isocentre in z direction. Image on the left represents the residual map if the offset is not taken into account (Shim 1). The centre image is the simulated residual map if the offset is taken into account (Shim 2) and the image on the right, the measured B_0 field when using Shim 2. Phantom is in HFp.

Figure 3.3 depicts the difference between the fields generated by a Shim 1 that does not account for the Z offset and Shim 2 that accounts for that difference.

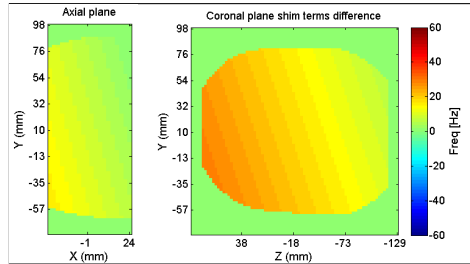


Figure 3.3: Simulated field generated by the difference of shim values between shims 1 and 2 of figure 3.2: $\Delta X_s = -0.005mT/m$ $\Delta Y_s = 0.001mT/m$ and $\Delta Z_s = 0.003mT/m$. Phantom is in HFp.

Figure 3.4 presents the residual B_0 field maps when the calibrated object centre has an offset in FH direction (z direction) related to scanner isocentre when the imaged object is in the FFp. Figure 3.5 describes coordinate information of figure 3.4.

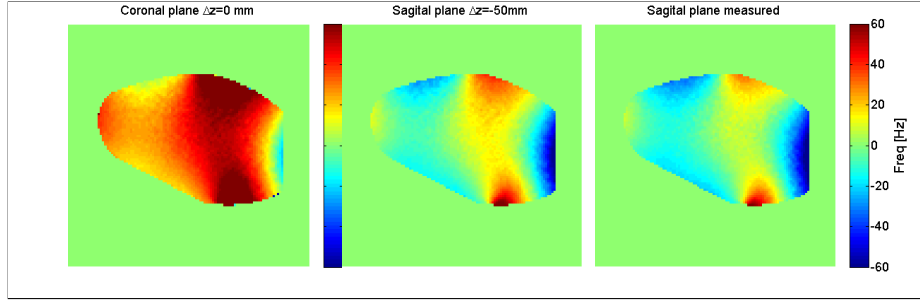


Figure 3.4: Coronal plane of residual B_0 field map of a phantom displaced 40 mm from isocentre in z direction and angulation of the imaging volume. Image on the left represents the residual map if the offset is not taken into account (Shim 1). The centre image is the simulated residual map if the offset is taken into account (Shim 2) and image on the right we have the measured B_0 field map when using Shim 2. Phantom is in FFp.

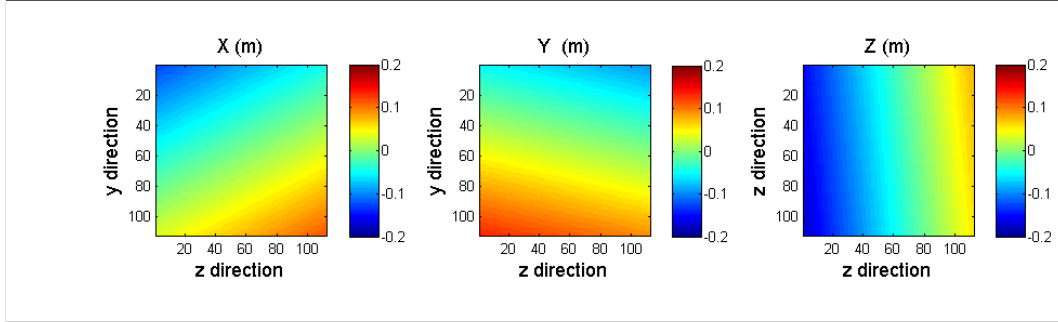


Figure 3.5: Coordinate information in xyz system of the slice presented in figure 3.4. In this example the angulation of the volume can be observed in the coordinate information.

In figure 3.6 is presented the field difference generated by a Shim 1 that does not accounts for the z offset and a Shim 2 that includes that displacement in FFp.

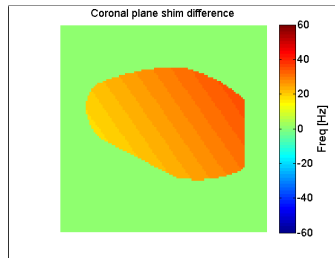


Figure 3.6: Simulated field generated by the difference of shim values between shims 1 and 2 of figure 3.4: $\Delta X_s = -0.001mT/m$ $\Delta Y_s = 0.003mT/m$ and $\Delta Z_s = 0.003mT/m$. Phantom is in FFp.

3.4 Discussion

This chapter intended to identify possible experimental limitations of the image-based shimming method. On the one hand it was intended to study shim coils accuracy, and on the other hand the coordinate information needed to correctly calculate shimming terms was evaluated.

For the coil verification it was possible to observe that all fields generated showed good correlation of one with its mathematical function description (table 3.3). The slope fit which takes into account all the functions in the model showed that the principal component for each one of the 9 experiments (from figure A.1 to A.8) are within 5% of the optimal result [51]. Cross-terms were found to be reduced. The only interference above 0.05 was observed between ZX and X terms (Slope -0.083). This can be related with the inclusion of data that tested higher X shim settings (0.25 mT/m) than for other linear terms which implied the exclusion of a few slices due to difficulty in unwrapping. In fact, the correlation coefficient for that relation was relatively poor ($R^2 = 0.78$), indicating that it is not observed in all points in the graph presented in Appendix A figure A.1.

The results obtained can be compared with the study presented by Kim et al [38]. They found normalized cross-correlation values between shim terms of the order of 0.10 to 0.25. These results justified the need to use a mapped field as a model for shim calibration in that study. Contrarily to the system used by the authors, our set of coils appears to be within the error allows the shim optimization without the need for shim coils field mapping. In fact, the use of a field reference matrix as a substitute of the ideal function can overcome some errors if it is constructed with various averages. Nevertheless, that is a process that takes time and involves the coverage of the volume where the sample can be placed. For neonatal scan, that could be possible due to the size and position of the baby's head, but for foetal scan the creation of such a reference would be impractical. It would be necessary to create a phantom that occupied the bore in a way that mimics the size of a pregnant woman. In addition, all data for the dHCP should be acquired with the same method. The use of a reference matrix in shim calculation could lead to some foetal scans being shimmed in different conditions.

It is known that the fields generated by the coils lose linearity away from isocentre [52]. This is one limitation of the method that was not studied in the present work. For neonatal scan this may not pose a problem since the head is positionated at the centre of the bore. For foetal scanning, the effect of such non-linearities may depend on the fetus's head position and requires also including the fat frequency information in the optimization.

The coordinate information exported along with the B_0 field map was not sufficient to have a correct correspondence between predicted and measured residual magnetic field. In figure 3.2 the need to add the table movement ($\Delta z = 40 \text{ mm}$) after the initial calibration is apparent. The difference in shim terms is only visible in linear terms (figure 3.3 and 3.6) and F_0 . In fact, if we

analyse the terms that vary with z (Z2, ZX and ZY) and substitute by $z = z + z_0$ where z_0 is the table shift, we can calculate that effect:

$$\text{Z2 term: } (z + z_0)^2 = z^2 + 2zz_0 + z_0^2 \quad (3.1)$$

$$\text{ZX term: } (z + z_0)x = zx + z_0x \quad (3.2)$$

$$\text{ZY term: } (z + z_0)y = zy + z_0y \quad (3.3)$$

These equations show the effect that the table movement can have on each linear term, especially the Z term that has a double contribution of the offset $(2z_0)z$. This shows the importance of correctly defining the coordinate system to be used. The inclusion of angulation in all direction showed in figure 3.5 verified the transformation when including different parameters. This was applied with the FFp in order to evaluate if the relation between the z direction and FH direction were correct. The solution found implied exporting the table position at the moment of B_0 acquisition. As a result, a mechanism of time verification was implemented in order to validate the correct information.

In this Chapter the practical limitations of active shimming based on field mapping were studied. It was possible to verify the accuracy of the field generated by shim coils, as well as evaluate and correct the effect of the table movement on the shim optimization. This part of the work served as the basis to build an image-based shimming tool that could be further improved and adapted to both neonate and foetal scans.

Chapter 4

Development of a neonatal image-based shimming tool

4.1 Introduction

To accurately map the brain of a neonate it is essential to acquire high resolution functional images typically using EPI. According to the description in the first chapter, if the resolution in the phase direction increases, its pixel bandwidth goes down leading to larger phase accumulation and more prominent susceptibility artefacts. As a result, acquisitions in the context of the neonatal dHCP require a strict control over the main magnetic field B_0 inhomogeneities.

Active shimming is usually applied in order to minimise those artefacts. Conventionally, the manufacturer's default method (e.g. FASTMAP) is applied because it is fast. Nevertheless, if FASTMAP (or Pencil beam (PB) volume) is used to map inhomogeneities over extended field areas, it can lead to an inadequate correction, because the field distribution along tissue borders changes rapidly [22]. Smaller volumes with heterogeneous regions, as in the baby brain, have also rapid changes along borders which hinder FASTMAP efficiency. Additionally, when using the manufacturer's method, the user only has control over a cubic ROI not anatomically adapted within which the field is mapped and corrected. That region, denominated *shim box*, has to be defined in order to include the bulk of the brain without inclusion of air/tissue interface at the scalp.

Neonatal brain is smaller than the adult brain, as a consequence the centre pixels are closer to brains' borders where the air-tissue interface is located [53]. Shimming in neonatal brain has been applied in the context of spectroscopy in order to improve the spectral linewidth, which has different requirements comparing with whole brain scan using high resolution EPI [54].

The aim of the work presented in this chapter was to develop an image-based shimming (IBS) tool adapted to neonatal brain imaging, which included definition of the ROI to be shimmed,

phase unwrapping and shim setting calculation, in order to improve EPI of the neonatal brain.

The work developed in this section was separated into two main sections: implementation of an optimized algorithm and interface for image-base shimming, and testing on neonatal infants in the context of the dHCP. Figure 4.1 illustrates the sections that constitute the program.

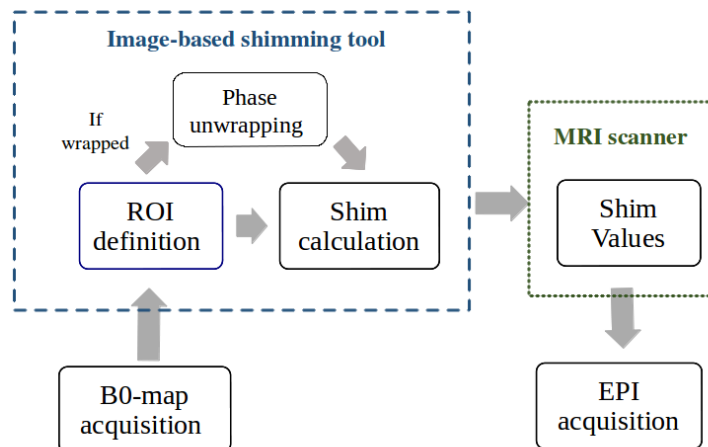


Figure 4.1: Flow chart of the image-based shimming tool. After B_0 -map acquisition of the neonatal brain the image-based shimming tool is applied. First a ROI is outlined and phase unwrapping is applied if necessary. Then shim settings are calculated using a least square optimization that includes the pixels within the ROI. Finally, shim values are exported to the MR scanner and the shim coils generate the correspondent field to shim the sample when EPI images are acquired.

4.2 Methods

4.2.1 Data acquisition and Shim evaluation

Data was acquired at the Neonatal Intensive Care unit at St Thomas' Hospital, where a 3T Philips Achieva scanner is installed. A dedicated 32 channel neonatal array receive coil was used for the neonatal data [55]. All scan acquisitions were in compliance with ethical requirements. Dataset acquisitions required changes to the current protocol, therefore all staff involved was informed about alterations needed.

Main magnetic field mapping was done by applying two gradient echoes with a T_1 fast field echo (T_1 FFE) sequence, and $\Delta TE = 2.3 \text{ ms}$ [5]. Field-of-view (FOV) of $160 \times 180 \times 160 \text{ mm}^3$ (AP, FH, RL directions), resolution of $2.5 \times 2.5 \text{ mm}^2$ and slice thickness of 6 mm (FH direction). The duration of the scan was 20.2 sec.

The images was exported to an offline computer where the algorithm developed in Matlab environment (version R2012a) was applied. The image-shimming method implemented is described

in section 4.2.2.

The algorithm was applied to 52 neonatal participants with mean gestational age at scan of 39.8 ± 1.7 weeks (range 35-42 weeks) and for all a residual B_0 -map was acquired using IBS shim settings. For 32 neonates the first B_0 -map was acquired with zero shim and for 22 neonates the B_0 -map was acquired with linear shim settings in order to decrease phase wrapping. For 34 neonates an additional residual B_0 -map was acquired with PB shim (based on FASTMAP) to compare it with IBS (22 with linear shim and 12 with zero shim). The residual B_0 field map with PB with was acquired immediately before the one with IBS volume and both with the same geometry.

The residual B_0 field maps were used to evaluate the field homogeneity improvement after shim. The magnitude images were registered to the anatomical images with FLIRT-FSL [56, 57] and the transformation was applied to the phase image. An average image of residual B_0 field maps was calculated to obtain information of mean inhomogeneities that were not possible to correct.

Measures of uniformity within the brain ROI were used to assess the pre and post shim brain field homogeneity. Different measures were used to characterize field inhomogeneity in different degrees. First, full width at half maximum (FWHM) of the histogram presents a measured of the deviation of the pixels near the mean frequency. Second, standard deviation (SD) allows to evaluate the overall pixel dispersion taking into account all pixels. Finally, 95% interval of pixel intensity allowed to take into account the maximum inhomogeneity that corresponds to the maximum distortion. Paired t-tests were applied to each measure (FWHM, SD and 95% interval) in order to analyse the difference between the field with no shim and with IBS, as well as between PB volume and IBS.

Functional images were acquired using single-shot GRE-EPI with TR=3870 ms, and TE = 38 ms, with resolution of $2.15 \times 2.15 \times 2.15 \text{ mm}^3$ and FOV $140 \times 140 \text{ mm}^2$ with shim settings applied. In the preparation phase a fat saturaton pulse was applied with the parameters described in 4.2.4.

4.2.2 Image-based shimming tool adapted to neonatal brain

4.2.2.1 Region of interest

ROI definition allows to delimit the sample volume used to fit the spherical harmonics model. It is critical to include voxels in the main areas of interest so as to reduce field inhomogeneities in those regions. Areas that enclose continuous spatial information should be included in detriment of other discrete areas. Pixels in isolated areas contribute information that increases the fit residuals in the main area of interest. ROI definition differs between foetal and neonatal imaging due to the environment in which the brains are immersed. The head in neonatal acquisitions is surrounded by air and it is therefore important to define a restricted ROI in which shim optimization is not dominated by susceptibility differences in border regions.

The initial procedure for ROI definition was done using thresholding of the B_0 map magnitude image to obtain the binary image of the brain. In magnitude B_0 images, areas like eyeball have an intensity similar to the brain cortex, making its exclusion difficult. To overcome this problem, images in the sagittal and coronal planes were used to identify the region of the eyes.

From a coronal plane it was possible to identify the location of the brain and its centre in RL direction (position between the eyes). The slice corresponding to this position in the sagittal plane was found. The position that corresponds to 25% of the brain dimension in the AP direction was measured. That allows to find the slices (HF direction) encompassing the frontal lobe, and as a consequence the ones in which eye balls are present (Figure 4.2). The area below that AP line and in front of the HF line was excluded in order to exclude the eyes.

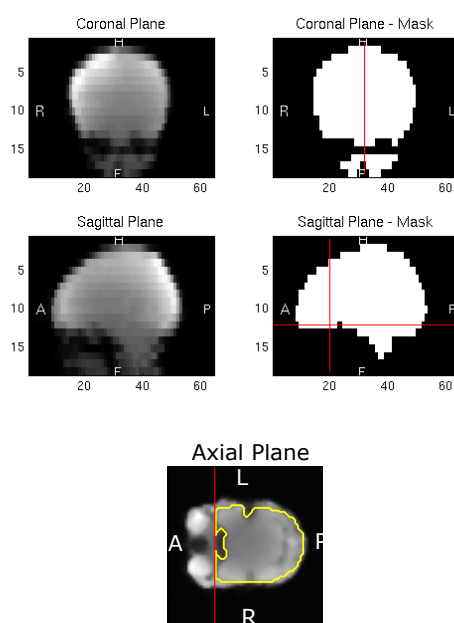


Figure 4.2: Magnitude B_0 field map in the coronal and sagittal planes with definition of the region to be excluded from the ROI. Coronal image used to define the position between the eyes in the RL direction. Sagittal image used to measure maximum brain diameter in the AP direction. The last magnitude image is an axial plane where the ROI with eyes exclusion is drawn in yellow, the area excluded is the region anterior to the red line. A - Anterior; P - Posterior; R - Right; L - Left; H - Head; F- Feet.

The exclusion area is presented in the sagittal plane of the B_0 field map in various positions in Figure 4.3. A T_2 image acquired at the same position is presented in Figure 4.4.

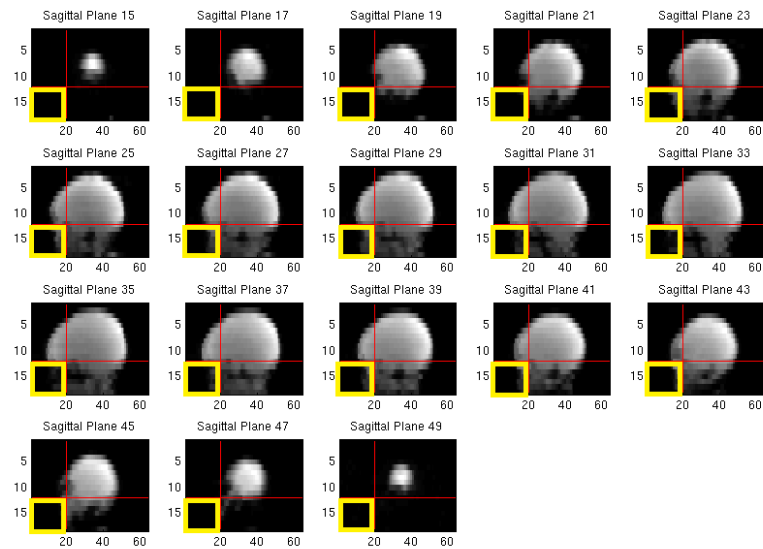


Figure 4.3: Magnitude B_0 - map sagittal plane and representation of the eye exclusion region (yellow square). After the brain's middle position in RL direction be defined in the coronal plane, the lower position tissue in the frontal portion of the head (same position as frontal lobe) is found. The region below that level and anterior's 25 % of maximum head width in AP direction is excluded.

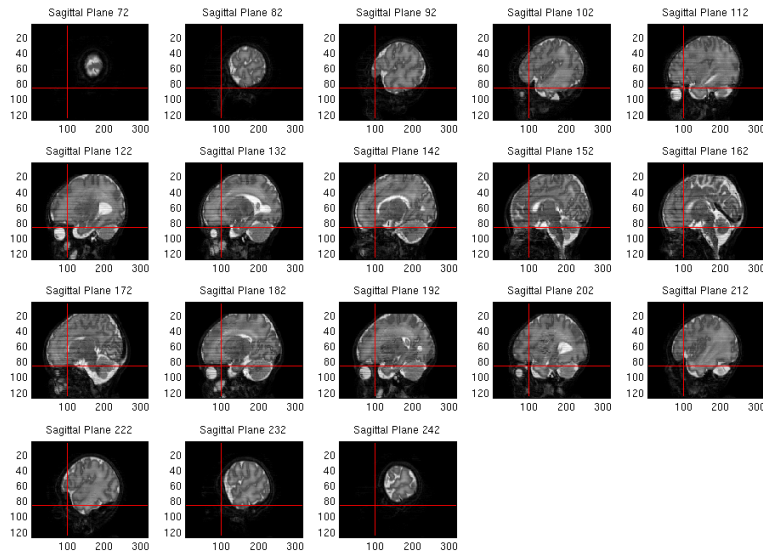


Figure 4.4: T2 weighted image in sagittal plane and representation of lines that define the exclusion region.

The overall graphical interface used to apply the methods described is presented in figure 4.5.

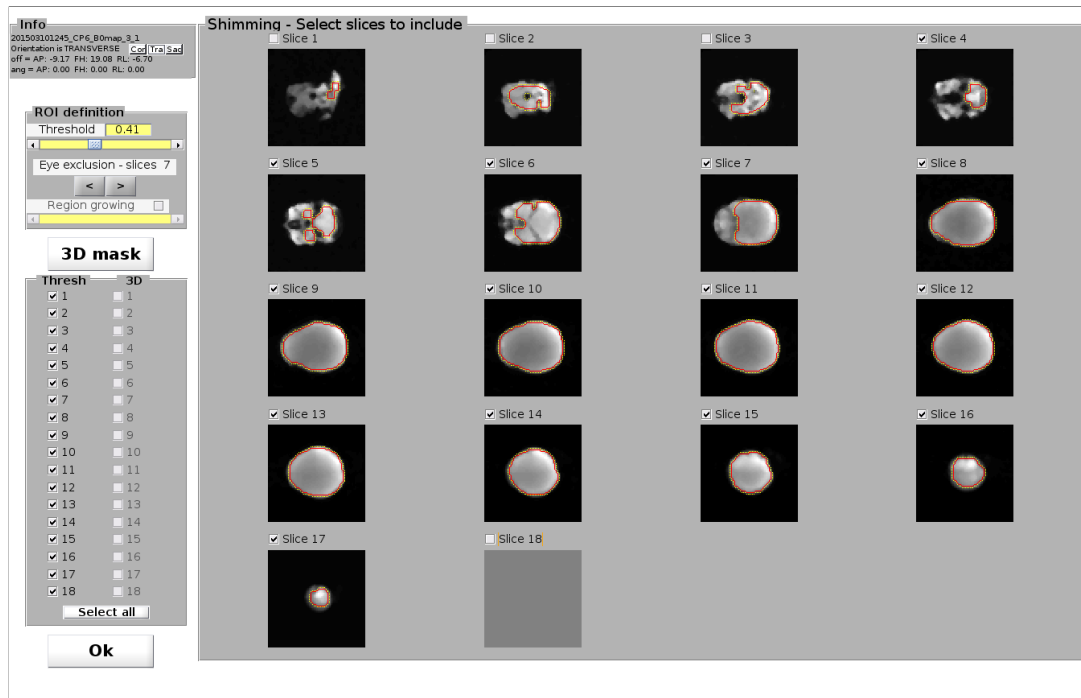


Figure 4.5: Graphical interface for ROI definition. The current ROI is outlined in red in all slices. First the threshold is adapted to include the brain, and the ROI presentation is updated automatically. The number of slices in which eyes should be excluded is defined (in this case until slice 7). If it is not possible to exclude certain areas like extra-cranial bleeding, a mask defined in three orthogonal planes can be used ("3D mask" - illustrated in figure 4.6). Finally, it is possible to choose which ROI should be used in each slice (checkboxes).

Additionally, a second ROI definition based on an ellipsoid projected to the three orthogonal planes (option "3D mask" in figure 4.5) was implemented. Its application is presented in figure 4.6. The dimensions and location of this ROI can be defined easily by the user in order to exclude scalp regions. The two types of ROI outline can be used on a slice by slice basis.

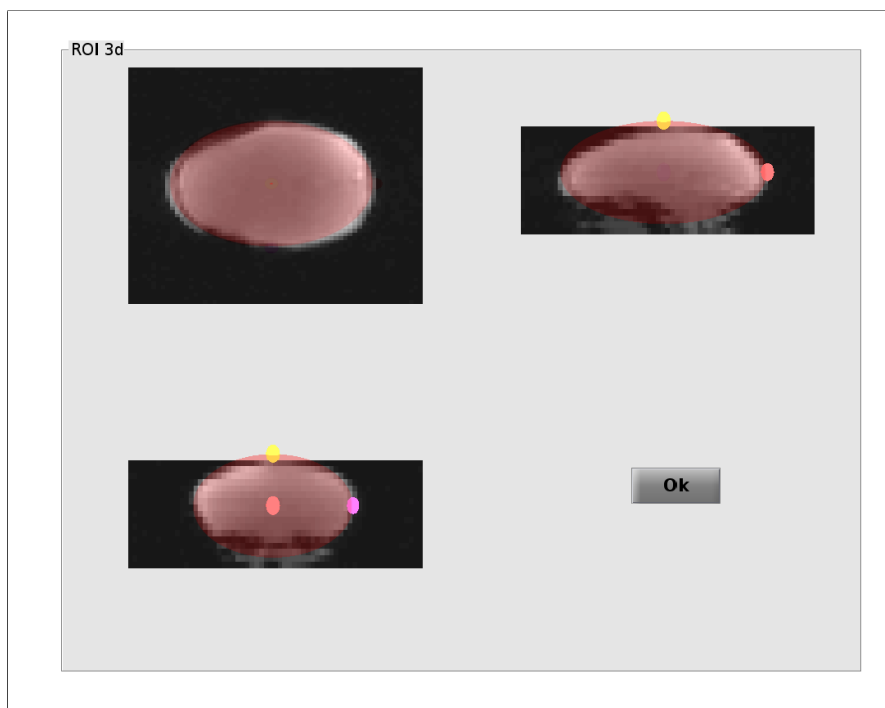


Figure 4.6: 3D ROI definition based on the three planes. The region in half transparent red is included in the final ROI. Small circles (yellow, pink and light orange) are dragged to define the dimensions of the ellipsoid main axis.

4.2.2.2 Phase unwrapping

The algorithm included phase unwrapping based on Goldstein 2D/3D unwrapping [58]. This section was applied when necessary to specific slices in order to reduce the interaction with the user and the time expended.

4.2.2.3 Shim calculation

Shim optimization fitted the spherical harmonics model to the B_0 -map voxels included in the ROI. This fit finds the optimized shim current which minimized the cost function in equation (2.24). The spherical harmonics model included the first and second order shims presented in table 2.1. The adjustment of the frequency at the origin (F_0) is done by the system after shim application.

For the minimization, a least square method constrained to the current limit for each shim coil was tested, with Tikhonov regularization [39]. The function *lsqlin* from Matlab[®] version R2012a was applied.

In the context of a neonatal brain there are two sources of perturbation that can decrease shim performance. On one hand the B_0 field map acquired has noise that cannot be avoided.

On the other hand, head movement during the EPI acquisition can lead to perturbations of the magnetic field that are not present in the measured B_0 -map used in the optimization. In order to reduce the effect of these situations it was necessary to find the adequate regularization parameter.

The influence of head movement in the shim performance was evaluated for different regularization parameters. This was done by studying the response of dispersion measures of the residual B_0 field map when accounting for movement between shim calculation and shim application. Head movements can be identified as translations and rotations along the three main axes [17]. After applying the tool MCFLIRT [56] (FSL) to two neonatal fMRI time series of 5 minutes characterized as having poor quality due to head movement. With this approach was possible to identify two maximal head movements: translation in z direction (around 6 mm), and rotations around z of 6 degrees.

Since translations in all directions and rotations around the z axes do not produce changes in the induced field, because they are parallel to the static field, it was possible to simulate the changes in shim field by translations in x , y (up to 7.8 mm) and z (up to 6 mm), as well as rotations around z (1, 5 and 10 degrees). For each rotation/translation the 95 % intervals of the residual field with movement was simulated. This measure was chosen in order to account for the worst case inhomogeneity, and how it respond to the parameter regularization. The standard deviation was also calculated in order to evaluate if the overall pixel dispersion was maintained at low lambdas. The regularization parameter λ was tested from 0 to 0.2 (step 0.005). The same process was applied to 10 dataset of B_0 field maps of neonatal brains.

4.2.2.4 Reconstruction and Export

Reconstruction of B_0 field map was done automatically on the scanner and exported to an off-line computer where the algorithm was remotely applied. After shim calculation, all shim settings were automatically exported back to the scanner in order to be applied to subsequent EPI and B_0 field map acquisitions.

4.2.3 Shimming graphical interface

The tool incorporates automatic procedures in order to reduce shimming time as well as operator dependency. The graphical interface developed allows the user to evaluate all B_0 -map magnitude images and the respective ROI for all slices.

Phase unwrapping is applied in a 2D format. This step can be applied to all slices after reference point inspection by the user, or a single slice if it is necessary. The reference point corresponds to the pixel with correct phase used to initialize the phase unwrapping algorithm.

Measured B_0 and predicted magnetic field after shimming is presented for visual comparison

and inspection (Figure 4.7). All documentation about the tool was written and stored in the same folder.

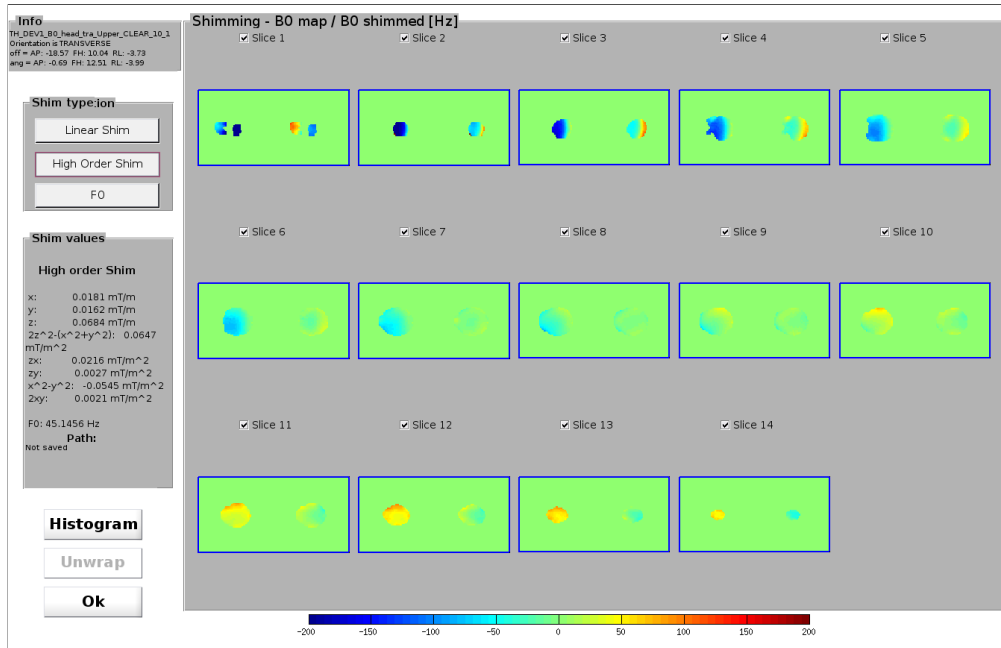


Figure 4.7: Main magnetic field within the ROI defined for all slices. The B_0 field map measured before shimming (at the left) and predicted after shimming (at the right) for 14 slices. Slices with blue border were the ones included in the optimization. Shim values for this example are presented at the left. The scale is presented at the bottom (-200 to 200 Hz).

4.2.4 Fat suppression - Neonatal head

Fat suppression was employed according with the default SPIR settings $BW=679$ Hz and pulse duration 7 ms. The pulse envelop is presented in figure 4.8.

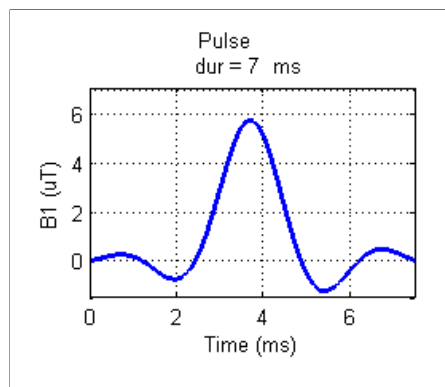


Figure 4.8: Envelope of the SPIR rf pulse.

The efficiency of the suppression of the fat around the head was studied after shim application. B_0 -map pixels outside the brain, as determined according to the structural images, were considered fat and added a shift of 430 Hz (water-fat shift at 3 T). The region outside the brain was studied as if it is fat because it was not possible to apply a fat imaging technique as Dixon.

Histograms of both regions (fat and brain) were displayed in order to evaluate the gap between frequencies of those regions.

Additionally, the same was tested in an adult brain and EPI images were acquired with different fat saturation rf pulse offset to evaluated if it was possible to maintain the brain signal and decrease fat signal. Although shimming of the adult brain is different from the neonatal brain we tested this effect in slices near the top of the head where the diameter of the brain is smaller.

4.3 Results

4.3.1 Optimization algorithm

The mean and standard deviation for the dispersion parameter 95% interval and SD for each λ for brain region of all datasets was calculated for translations in all directions and rotation around z . The results are presented in Appendix B Figures B.1, B.2, B.3 and B.4. The results for translation in x are presented in figure 4.9.

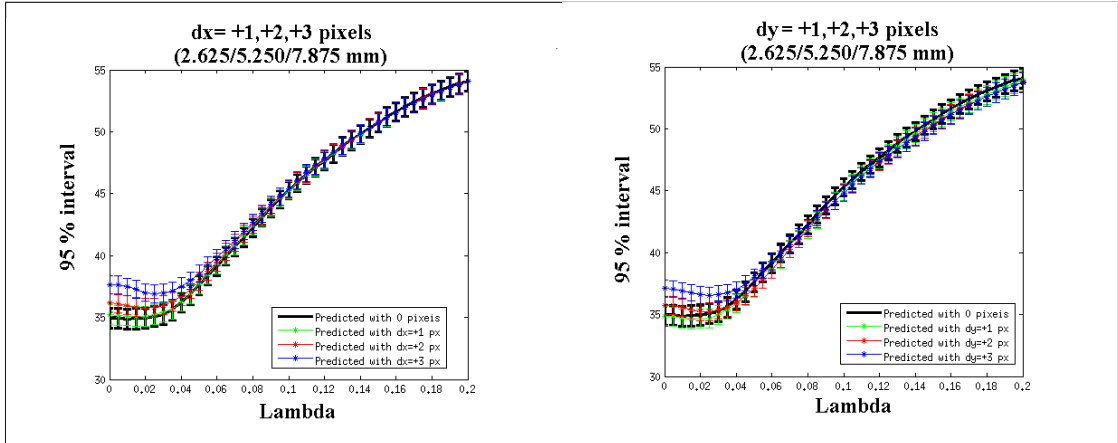


Figure 4.9: Simulation of the 95% interval in Hz of the B_0 map if the shim values calculated with different regularization parameter (lambda) values are applied after translation in $-x$ (RL) and $-y$ (PA) directions. Translation of 1, 2 and 3 pixels correspondent to 2.65, 5.25 and 7.87 mm.

According with figures B.1 to B.4 where the 95% interval within the ROI resented, a good regularization parameter would be $\lambda = 0.03$. The dispersion measures (95 % interval and SD) are related with the residual norm because they are obtain from the residuals. The behaviour of

those measures when accounting for movement between shim calculation and shim application are related with the solution norm, because lower shim values (less than optimal solution) will lead to less field inhomogeneity in the brain, and lower residuals than without regularization. The point where the 95% interval rise in the simulated translation curves relate to the corner of an L-curve in figure 2.9. That point represents the trade-off between the solution norm (i.e. shim values) and the norm of the residuals (fit to the magnetic field measured). For low regularization parameters ($\lambda < 0.03$) the regularization have more impact on the solution norm, while a high regularization parameter ($\lambda > 0.03$) have a larger increase in solution norm.

Because the major aim is to maintain the low residuals in the presence of movement by decreasing as much as possible the solution norm, the λ chosen was the one with low 95 % interval. In figures B.1, B.2 and B.4 shows a decrease of 95% interval at $\lambda = 0.03$. The was maintained almost constant from $\lambda=0$ to $\lambda = 0.03$.

4.3.2 B0 homogeneity

Measures of dispersion standard deviation, FWHM and 95% interval of the residual B_0 -map without shim, residual B_0 -map predicted after simulation and residual B_0 -map with IBS are presented in figures 4.10, 4.11 and 4.12. All measures of B_0 -map with IBS were significantly lower than without shim (p-value<0.001).

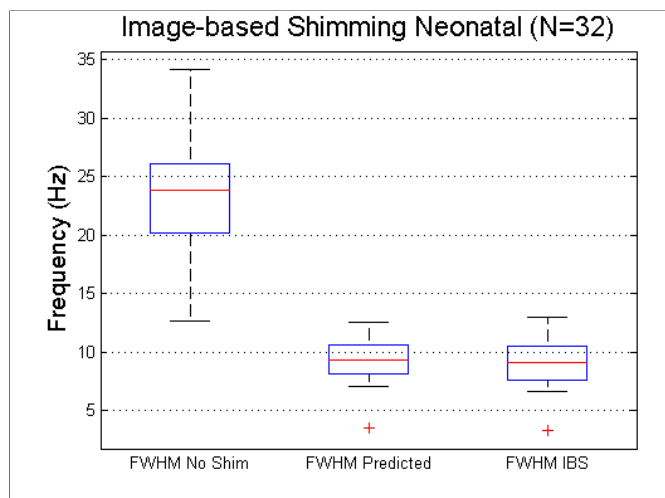


Figure 4.10: Box plot of FWHM of B_0 field maps without shim, and predicted and measured residual B_0 field map after IBS.

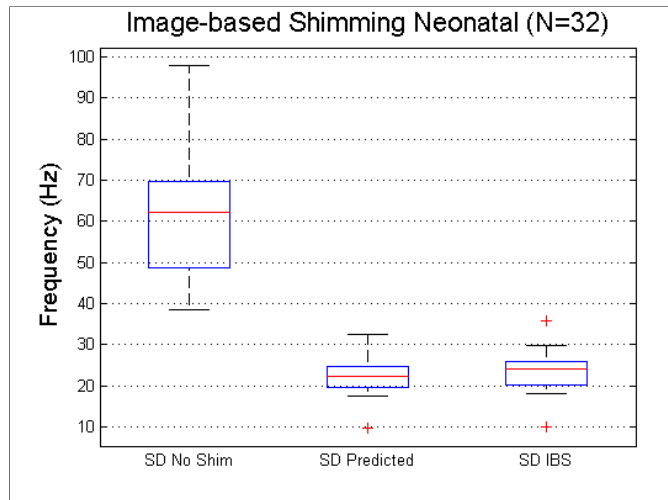


Figure 4.11: Box plot of standard deviation (SD) of B_0 field maps without shim, and predicted and measured residual B_0 field map after IBS.

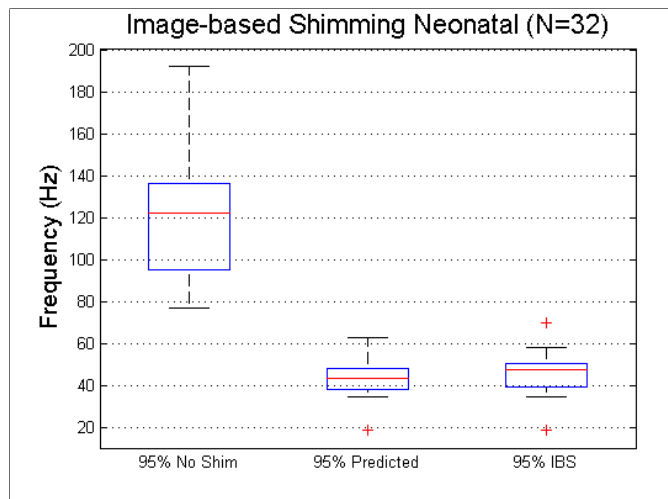


Figure 4.12: Box plot of 95 % interval of B_0 field maps without shim, and predicted and measured residual B_0 field map after image-base shimming (IBS). The 95 % interval was defined as the frequency interval within which 95% of B_0 map brain ROI pixels are.

The regions where the shim tool could not compensate for inhomogeneities are presented in the mean B_0 -map in figure 4.13.

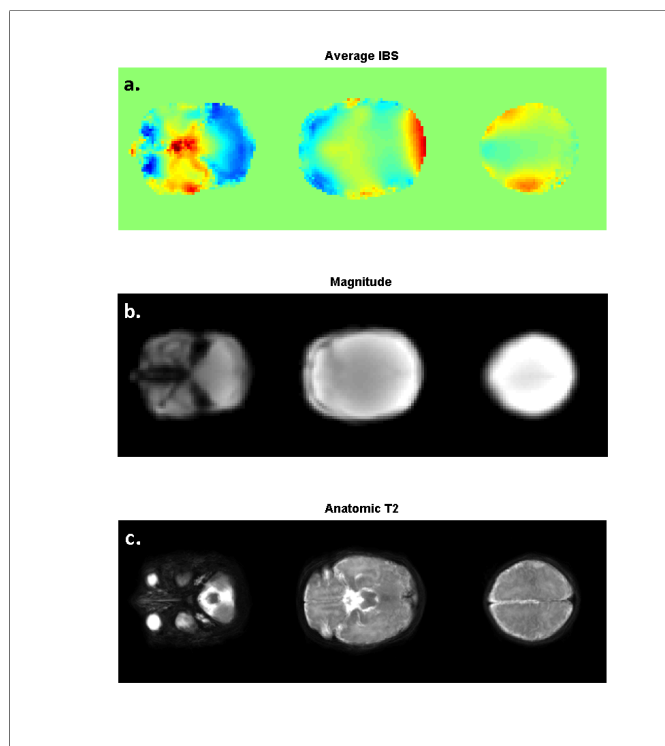


Figure 4.13: Characterization of the main field in the brain after applying IBS tool and respective structural images averaged from 20 subjects randomly chosen from the 54 subjects. **a.** average residual B_0 -map (in Hz) with IBS shim values at three different levels; **b.** magnitude B_0 field map; **c.** anatomic T2 weighted image. It is possible to observe in image **a.** the existence of regions with high inhomogeneity at the back of the head in the second slice and at a lateral level in the third slice presented. Scale -100 to 100 Hz.

4.3.3 IBS vs PB

In order to compare the main field homogeneity between the tool developed and the method offered by the manufacturer (e.g. PB volume) the region included on the IBS was compared with the same region in PB.

Figure 4.14 presents mean shim settings and the standard deviation for IBS and PB volume. Shim values for both methods were similar, although their standard deviation was smaller in IBS.

The comparison between IBS with PB volume did not showed significant differences in measures of FWHM, SD and 95 % interval (p-value > 0.1). Nevertheless, when analysing the measures IBS showed a trend to be lower (Figures 4.15, 4.16 and 4.17).

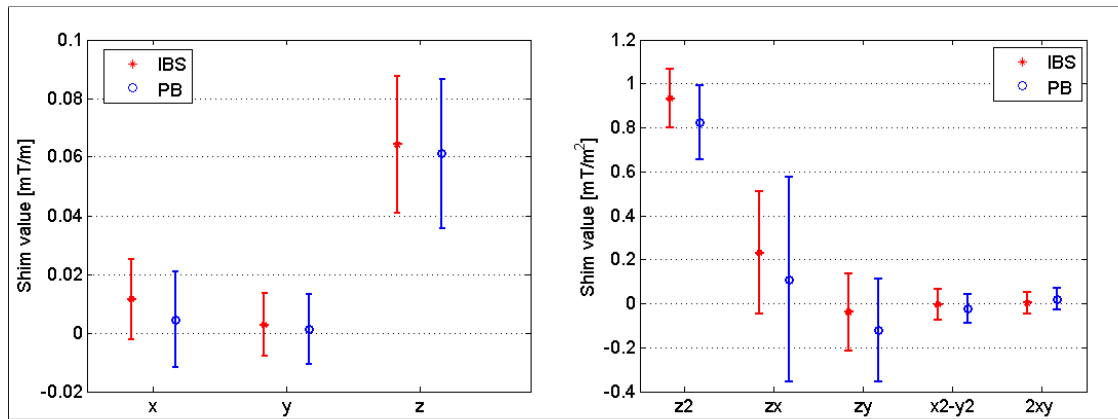


Figure 4.14: Mean \pm SD of shim values applied with PB and IBS.

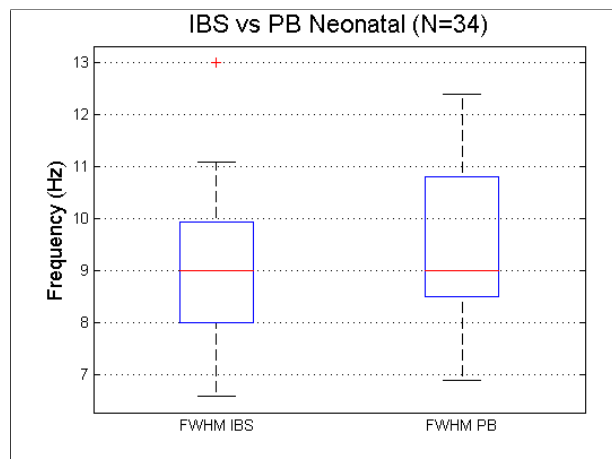


Figure 4.15: Box plot FWHM of the residual B_0 field map when applying IBS and PB volume.

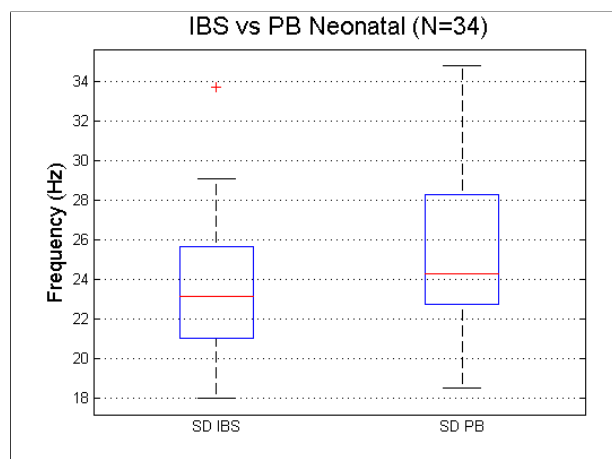


Figure 4.16: Box plot SD of the residual B_0 field map when applying IBS and PB volume.

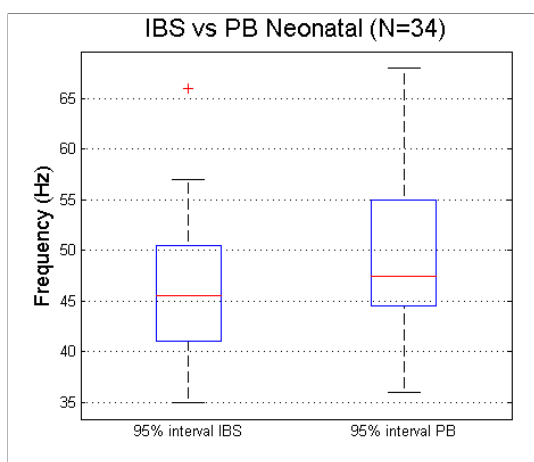


Figure 4.17: Box plot of the 95% interval of the residual B_0 field map when applying IBS and PB volume. 95% interval -frequency interval within which 95% of B_0 map Brain ROI pixels are.

In figure 4.18 is also presented one example where both shims are compared in terms of B_0 magnetic field inhomogeneity. Regions of interest included in the shim optimization are also presented.

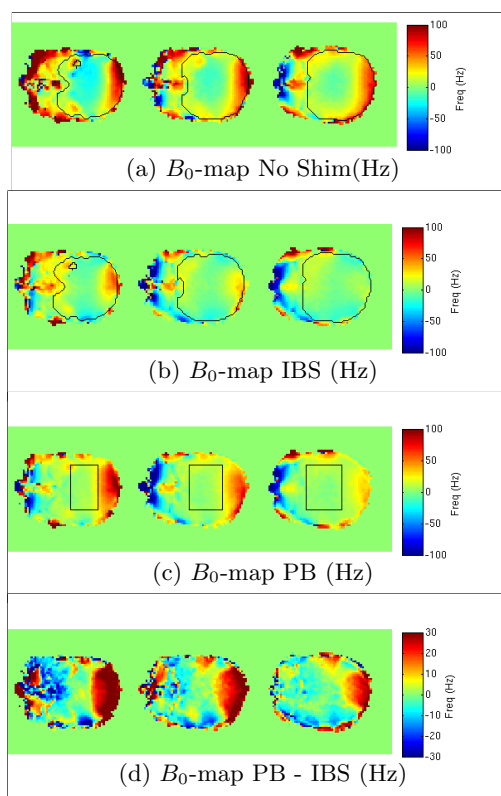


Figure 4.18: Comparison between IBS and PB volume results in terms of field inhomogeneity in Hz. In images (a) and (b) the the black line outlines the ROI used in IBS. Image (c) is the residual B_0 field map after PB volume and the rectangles define the shim box in those slices. The final image (d) is the B_0 field map difference between both methods [PB – IBS].

4.3.4 Neonatal brain EPI

In order to present the effect of B_0 inhomogeneities in EPI images of the baby brain two datasets were chosen: one in which the major inhomogeneities were corrected (Figure 4.19), and other in which the residual B_0 -map presents high inhomogeneities (Figure 4.20), both term infants. Figure 4.20 intends to show how high field inhomogeneities can lead to signal loss and deformation. Figure 4.19 shows that low field variations are possible to be obtained, but they also have a negative effect the EPI images.

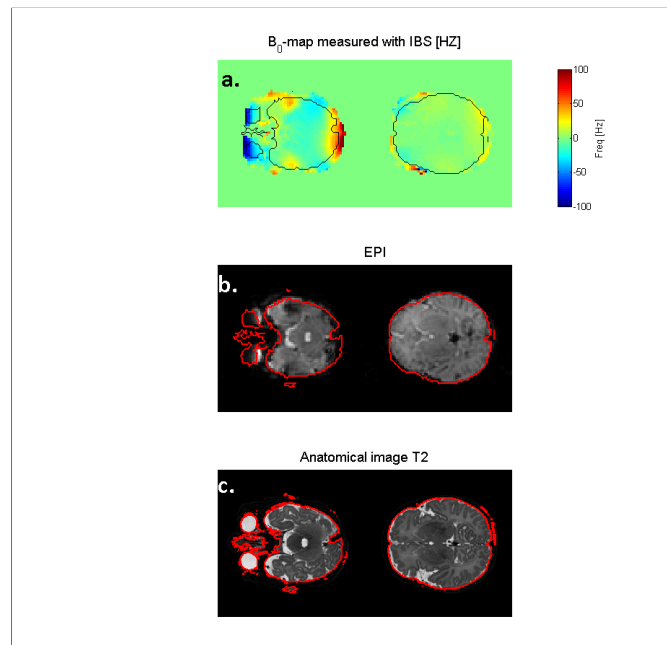


Figure 4.19: Effects of low field inhomogeneities in EPI. **a.** B_0 -map after applying IBS (SD = 18 Hz); **b.** EPI image acquired with the same shim settings; and **c.** anatomical image at the same position. First slice is located at the base of the brain and the second at a higher level. In image **a.** the border in black delineates the ROI included in the shimming. The outline in red in **b.** and **c.** is the brain delineation obtained from the structural image **c.** .

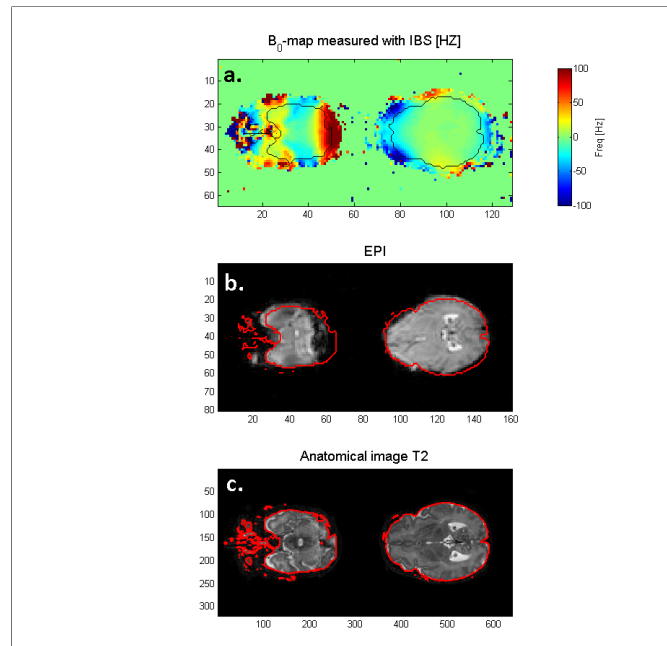


Figure 4.20: Effects of high field inhomogeneities in EPI. **a.** B_0 -map after applying IBS (SD = 27 Hz); **b.** EPI image acquired with the same shim settings; and **a.** anatomical image at the same position. First slice is located at the base of the brain and the second at a higher level. In image **a.** the border in black delineates the ROI included in the shimming. The outline in red in **b.** and **c.** is the brain delineation obtained from the structural image **c.**

4.3.5 Fat suppression - Neonatal head

Segmentation of the neonatal head used to investigate fat suppression was done using a T2 weighted image, and is presented in Figure 4.21.

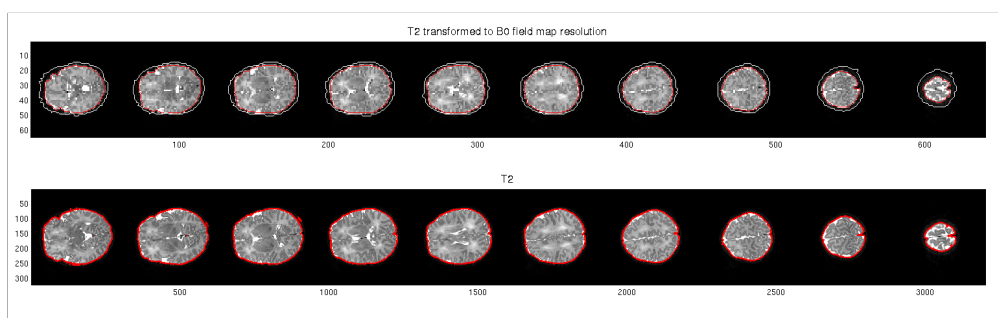


Figure 4.21: Anatomical image with brain's region of interest.

For the same subject unshimmed B_0 field map and residual B_0 field map are presented in figure 4.22, with respective fat and brain segmentation.

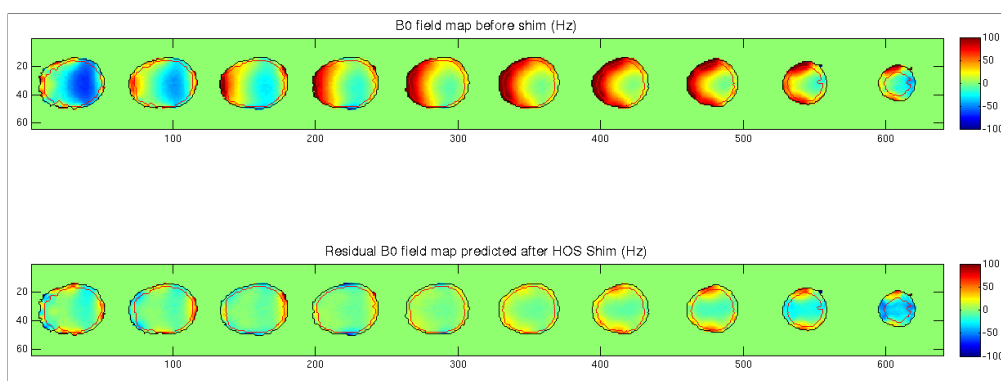


Figure 4.22: Head B_0 field maps before and after image-based shimming (IBS) in Hz.

Histograms for fat and brain of the same subject are presented in figure 4.23. The frequency clear gap between fat and brain for the neonate in this example is of the order of 300 Hz and the fat SD after shim was 30 Hz. From 16 datasets tested the mean SD of the fat after shimming the brain was 44 ± 11 Hz.

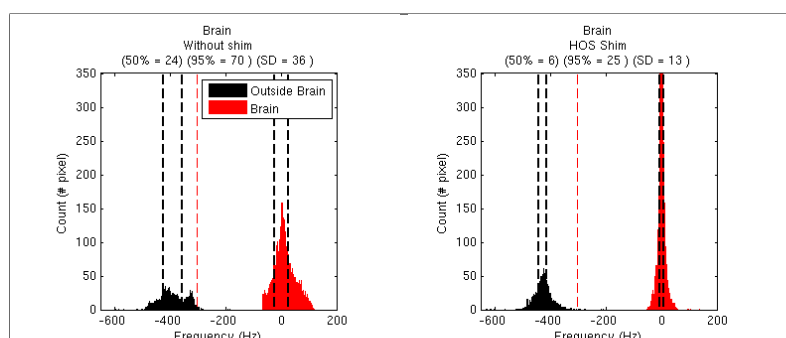


Figure 4.23: Histograms of brain (black) and outside brain (red) regions, before and after image-based shimming (IBS) in Hz. Measures in Hz: 50% - frequency interval within which 50% of Brain ROI pixels are; 95% - frequency interval within which 95% of B_0 map Brain ROI pixels are; SD - standard deviations of pixel frequency of ROI of the Brain. Black dashed lines represent the 50% interval for brain and outside brain. Red dashed lines represent the fat saturation pulse 99 interval ($99/BW=879/679$ Hz).

The evaluation of the efficiency of the fat saturation rf pulse in the brain was performed in an adult brain as we can see in figure 4.24 and 4.26. Figure 4.24 displays the B_0 field maps of an adult brain and the histograms from the brain and neighbourhood region. Fat histogram in this case is similar to neonate when observing fewer slices.

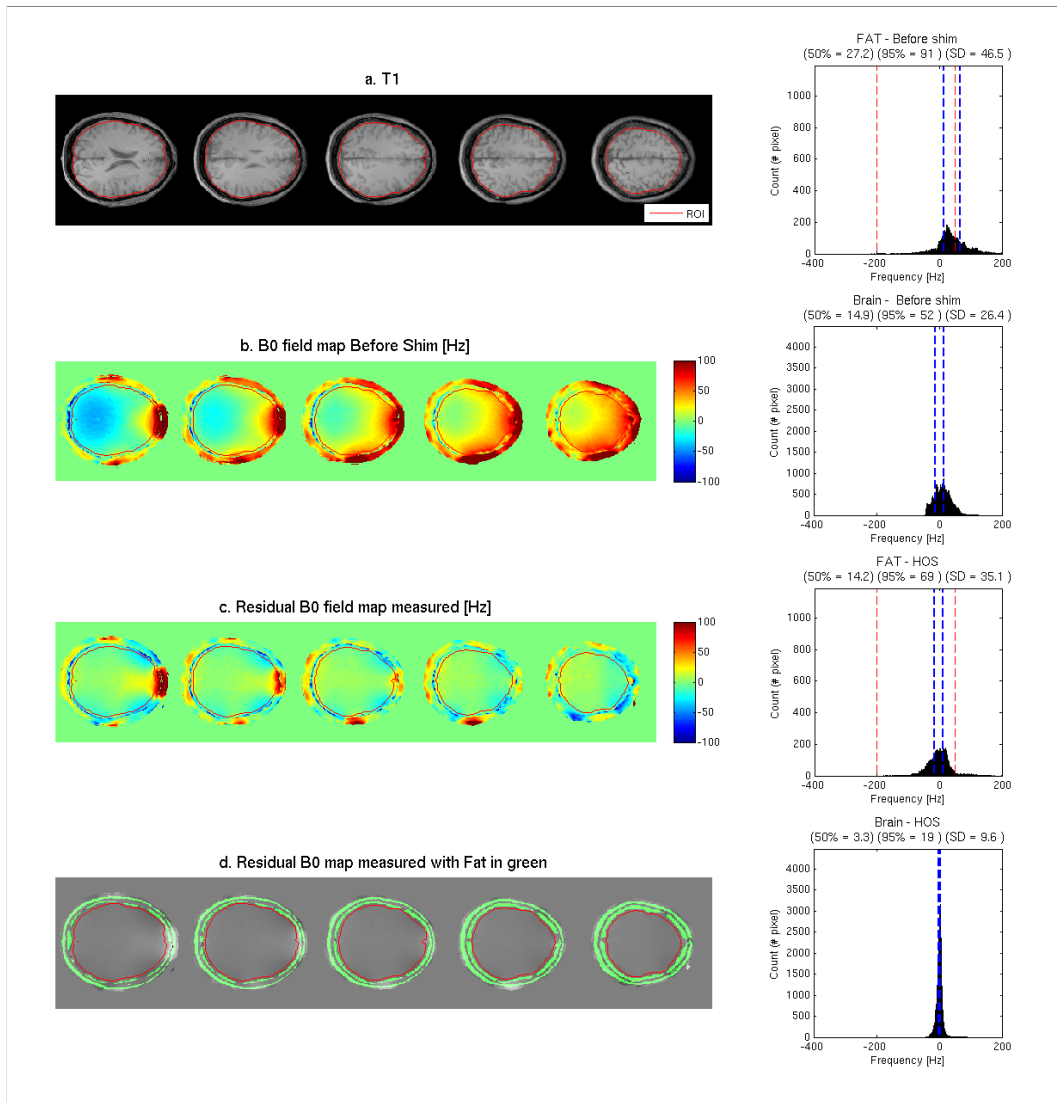


Figure 4.24: Head B_0 field maps before and after image-based shimming (IBS) in Hz. Five slices correspondent to 35 mm in FH direction (from 19 slices included in the IBS with FOV $220 \times 220 \times 147 \text{ mm}^2$) of an adult head are displayed. **a.** Anatomical T1 weighted image **b.** B_0 field map before IBS; **c.** Residual B_0 field map after IBS; **d.** Residual B_0 field map after IBS with fat representation in green. Fat region was extracted by applying a threshold to a fat image acquired through a Dixon acquisition. Red - region of interest applied in IBS. Second column presents histograms of fat and brain regions before and after high order (HOS) IBS. Measures: 50% - frequency interval within which 50% of ROI pixels are; 95% - frequency interval within which 95% of B_0 map pixels are; SD - standard deviations; IBS - Image-based shimming.

Chemical shift artefact in phase encoding direction of single shot EPI of an adult head is presented in figure 4.25. The inversion of PE direction lead to a chemical shift in the opposite direction.

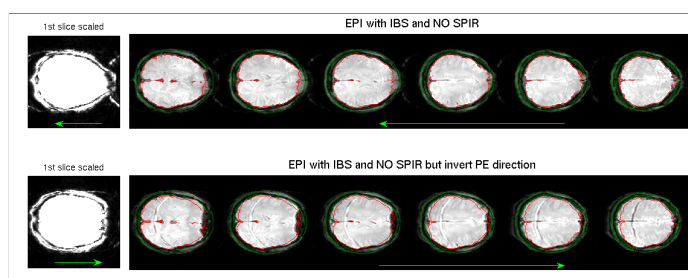


Figure 4.25: Chemical shift in the phase encoding direction (PE) of single-shot EPI of the head. Images in first line present the chemical shift from right to left and the second line shows the same artefact in the opposite direction. Water fat shift in this acquisition was 20 pixels.

EPI images with different SPIR rf pulse offset are presented in figure 4.26, using default SPIR offset ($\Delta f_{def} = -639 \text{ Hz}$), $\Delta f = -530 \text{ Hz}$ ($\Delta f_{def} + 109 \text{ Hz}$) and $\Delta f = -430 \text{ Hz}$ ($\Delta f_{def} + 209 \text{ Hz}$). In the first image without SPIR it is possible to observe the chemical shift artefact in the middle of the brain, that same artefact is corrected when applying the default SPIR. The brain signal intensity suffers a slight decrease that worsens substantially as the pulse gets closer to water frequency.

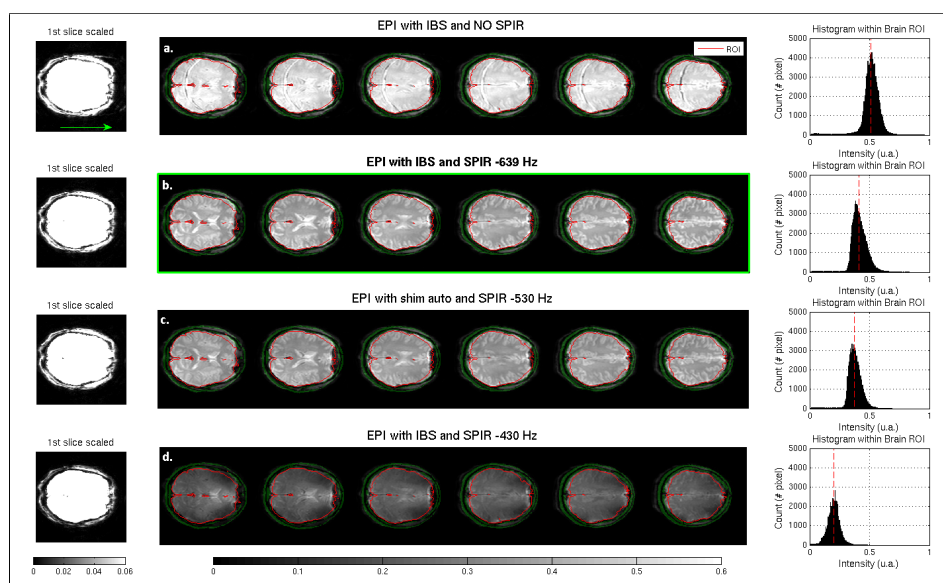


Figure 4.26: Effect of saturation pulse frequency offset on adult brain signal intensity. For all EPI acquisitions the same shim values calculated with the IBS tool were applied, specific rf pulse frequency offset was tested: **a.** no fat suppression; **b.** SPIR with default rf pulse offset (-639 Hz); **c.** SPIR with offset -530 Hz; and **b.** SPIR with offset -430 Hz. For each set the histogram of pixel intensity within the region outlined in red is displayed at the left column. It is also displayed in green the position where tissue outside the brain is located according with structural images (which includes fat). The first column presents the first slice of each set scaled in a narrower interval to evaluate the effect of the pulse.

4.4 Discussion

Neonatal image-based shimming in the context of dHCP implies an in depth knowledge of the method applied and its results. This work also required the study of strategies that could be used by the clinical team responsible for neonatal scanning. In order to apply a method with such characteristics, it was necessary to characterize the optimization problem (ROI definition and regularization) and its implication in the final images (final EPI and effect on fat suppression).

The definition of the ROI to be included in shim fit had to be implemented in a way that allowed an easy application by the user. Threshold segmentation of the magnitude images was applied as a first step. Identification of eye balls was possible in all datasets, which indicates the correct application of the algorithm. This was also possible as an adapted coil ensured the positioning of all babies is the same [55], alongside a fixed acquisition protocol.

The developed software allows a ROI definition that is more user independent than manual segmentation, while flexible when needed. In fact, with this method it is possible to adapt the ROI through the combination of thresholding, eye exclusion, and ellipsoid definition in three planes. The mean volume included in the optimization with the default method, that comprised only thresholding and eye exclusion, was ($V = 514 \pm 64 \text{ cm}^3$). The volume defined appear similar between subjects when the same default method is applied. Variations in the volume are due to inter subject differences of the babies' brain sizes. In fact, when applying a noise mask to the magnitude images the volume selected is $746 \pm 92 \text{ cm}^3$, corresponding to gestational age varying between 35 to 42 weeks. In two babies scanned an extra-cranial bleeding was present and was also excluded easily with the ellipsoid ROI definition.

The software significantly reduced the inhomogeneity in the region shimmed. The three dispersion measures were significantly lower after shim, indicating that the improvement was present in all degrees evaluated. In addition, the predicted B_0 field map was consistent with the residual field measured. As a result, in the context of neonatal shimming the simulated value can be used as a correct indicator of the shimming result.

The evaluation of the average residual B_0 field map show the presence of two regions with higher inhomogeneity: lateral-frontal region above the eyes; and occipital region (Figure 4.13). High degree of homogeneities in these regions are not usually present in shimmed adult brains. The lateral region with high field inhomogeneity can be related with the difficulty to compensate irregularities near the edges of the brain when accounting for the whole brain. Magnetic field inhomogeneities in the occipital region were also difficult to correct in central slices. Although this is related with the high value of the Z^2 shim, it is important to test the presence of pillow pads that can be responsible for this finding. In order to overcome the limitations of image-based shimming in infant brain passive shimming might be applied to improve the local result [59].

Both IBS and PB volume shimming were studied in the present work to evaluate the gain

that could be achieved through the new method. Despite the fact that the measures of dispersion did not present significant differences, it was possible to observe in the box-plot the presence of a higher median in SD and 95 % interval and higher lower and upper quartile for all measures. The subtle disparity can be related with pixels selection for shim calculation. On one hand, IBS includes all head with exception of lower slices at the level of the maxilla. On the contrary, PB volume privileges the interior part of the brain. As a result, differences are only apparent around the boundary of the brain for which pixels were not included in PB volume. Accordingly, SD and 95 % interval showed the highest disparities. The example in figure 4.18 illustrates that same finding. The ROI used in IBS includes extra pixels especially in the back of the head where inhomogeneities were more difficult to correct in the cohort studied.

One other advantage of the present IBS software over PB volume is the fact that the user has control over all parameters been used to shim the image while in PB volume the user only has control over the shim box. In addition, it was developed in order have a field map more robust to motion.

The effect of the residual inhomogeneity in image quality was also investigated. The selected examples seen in figures 4.19 and 4.20 show how a good shimming approach is critical to obtain EPI images suitable for analysis.

In the presented work the main artefact was signal loss because a GRE sequence was tested. On one hand, in GRE there is no refocusing pulse therefore the signal may decay considerably before the end of the acquisition. In addition, it is a single-shot method in which the TE is considerably higher and accumulations in phase can lead to misregistration of the signal outside k-space. Inhomogeneity around 25 Hz can lead to signal loss of adjacent pixels and impurities of the order of 100 Hz can be difficult to correct leading to loss of a substantial region in the image as it is possible to observe in figure 4.20.

The study of fat suppression in babies' heads was important in order to evaluate its adequacy to the shimming method applied. Misregistration of fat can correspond to a shift of 20 pixels in the presented images that contaminates functional information. If the shimming method deviates the lipid frequency towards the water resonance frequency, the efficiency of rf saturation pulse may decrease. The study of neonatal head magnetic field maps indicates that IBS does not deviate fat signal and that the standard pulse is adequate to the water-fat frequency gap of the present sample.

Further investigation in an adult head showed consistency with neonatal's frequency histograms. The default SPIR pulse adequately suppressed fat in EPI fMRI images in which lipids were shifted into the brain. In addition, the EPI acquired with different rf pulse offsets suggests that a shift of the fat saturation pulse towards water frequency does not have practical gain to the final image. Although a decrease of 109 Hz in the offset have only a slight reduction of brain signal, it does not result in differences in fat (Figure 4.26).

In conclusion, the tool developed was effective to shim neonatal brain, allowing the clinical

team to use it and have control over the process. When comparing with PB volume the method showed better results in regions outside the shim box although measures were not significantly different. Finally, it was possible to verify the adequacy between the imaging methodology (e.g. fat suppression) and the shimming method.

Chapter 5

Development of foetal image-based shimming tool optimized for efficient fat suppression

5.1 Introduction

Functional and diffusion imaging of the foetal brain are important in order to achieve a dynamic map of the human brain connectivity during its development. EPI of the foetal brain requires fast and quiet EPI, which can be achieved at the expense of a lower bandwidth in the phase encoding direction. Unfortunately, this leads to severe susceptibility artefacts that can be minimized with localized IBS of the foetal brain, including 2nd order shims. Despite enabling improved shimming in the foetal brain, including these terms provokes high field variation in the more distant maternal adipose regions, and it becomes difficult to saturate fat without affecting the water signal. Due to the chemical shift artefact characteristic of EPI, the difficulty to saturate properly the fat in the adipose tissue can jeopardize the functional information in the foetal brain.

Previous attempts to improve fat suppression and/or decrease inhomogeneities outside an ROI involve minimization of a cost function that includes all pixels within the FOV [1,2] or weighting the contribution of different regions to the final solution [3]. The study of shimming outside the main region of interest has been studied, in the head, prostate and liver, but not in the context of foetal imaging.

The method developed in Chapter 3 for neonatal imaging does not attempt to prevent deviation of fat frequency. As a result, additional work was required in order to adjust the method

to foetal shimming. This chapter presents an image-based shimming tool of the foetal brain optimized for efficient fat suppression. The work consisted in two main sections: study of the fat saturation rf pulse, and implementation of a least squares fit with linear constraints applied on the fat region.

5.2 Methods

The work described in this chapter was divided into two main parts. The first, detailed in section 5.2.2, addresses the possibility to optimize the SPIR rf pulse for EPI abdominal scanning. The second part, described in section 5.2.3, reports the implementation of a new IBS method adapted to foetal imaging.

5.2.1 Data acquisition

Acquisitions were performed on a Phillips 3T MR system with a 32 channel body coil in 8 volunteers: 2 adult males and 6 pregnant women. In the adult male volunteers (ages 27 and 25 years) SPIR settings in the kidney, as replacement of a foetal brain, were investigated. Shim approaches and optimized SPIR settings were subsequently tested together in foetal voluntaries. The mean gestational ages were 28 + 6 weeks (range 27 to 31 weeks). Participants were positioned supine feet-first, and the radiographer attempted to centre the foetus' head at the scanner isocentre.

For all volunteers B_0 field maps were acquired as described in section 4.2.1, with FOV $450 \times 450 \times 120 \text{ mm}^3$ and resolution $2.3 \times 2.3 \times 10 \text{ mm}^3$. Mapping was done with two different shimming methods as will be explained in section 5.2.3.

In order to delineate fat regions an Dixon protocol was applied immediately before the first B_0 field map. That acquisition allowed to obtain images containing only fat that were thresholded to obtain a binary mask of that tissue. The geometry and resolution were the same as B_0 field maps, with the fat region outlined.

Functional imaging was collected using a single-shot GRE-EPI with repetition time TR of 2900 ms, TE of 50 ms, resolution of $2.5 \times 2.5 \times 3.5 \text{ mm}^3$ and FOV $320 \times 320 \text{ mm}^2$. The bandwidth in the phase encode direction for this acquisition was 1690 Hz (WFS of 32 pixels). During the preparation phase a SPIR method was applied, and the settings are described in section 5.2.2.

5.2.2 Fat suppression

The choice of SPIR as a fat suppression method was conditioned by the restrictions in the time between pulse application and sequence initiation. Fat suppression was employed according to the default SPIR settings described in section 4.2.4 (BW=679 Hz and duration 7 ms). The

slice profile of the rf pulse (Figure 4.8) was reproduced using an algorithm for Bloch equation simulations supplied by Dr. Shaihan J. Malik.

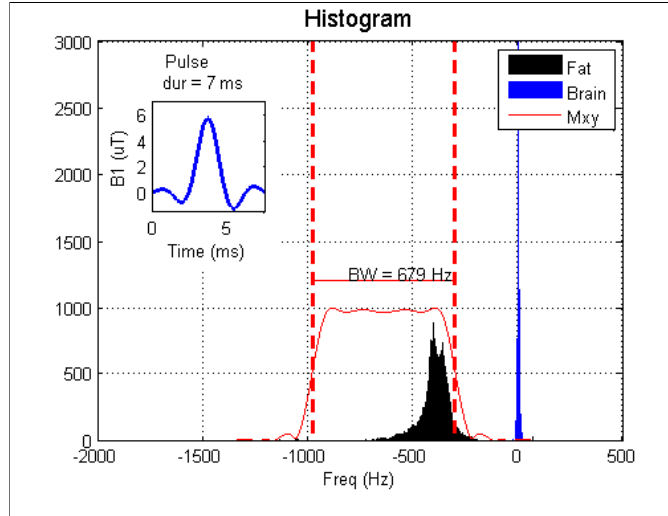


Figure 5.1: Histogram of fat and brain regions of B_0 field map of a pregnant volunteer. The slice profile of the SPIR pulse is presented in red (with maximum flip angle of 105 degrees). The bandwidth is also illustrated. The rf pulse presents ripples near the transition regions.

In order to evaluate the real impact of shimming on SPIR efficiency of abdominal imaging a kidney was shimmed with different approaches. First, an EPI of a kidney using the default SPIR was tested with shim auto (i.e. linear), PB volume and IBS. Second, the same EPI protocol was repeated with different rf pulse offsets to evaluate possible improvements. Finally, different combinations of pulse durations ($\alpha \frac{1}{BW}$) and offsets were investigated.

5.2.3 Image-based shimming adapted to the foetal brain

In order to adequately apply foetal shimming, the tool implemented for neonatal brain (Chapter 3) was adapted to include additional features. This was needed because the neonatal shim method included only hardware limits for the shim values and the solution was otherwise chosen to be the one that minimized the residuals within a restricted ROI. As a result, if this method was applied without any change, it would lead to a deviation of the frequency of fat in the abdomen. Because this optimization minimizes inhomogeneities within the ROI without further concerns, we denote this as optimal IBS (O-IBS).

For foetal imaging the adjusted tool included a simplified ROI definition, and a shim calculation with linear constraints that accounts also for the effect of shimming in the fat frequency. This method will be termed constrained IBS (C-IBS), and includes segmentation of fat regions and a complete B_0 field map unwrapping. The flowchart in figure 5.2 illustrates the process of shimming the brain of a foetus and the differences between the default method applied for

neonate (O-IBS) and the new C-IBS.

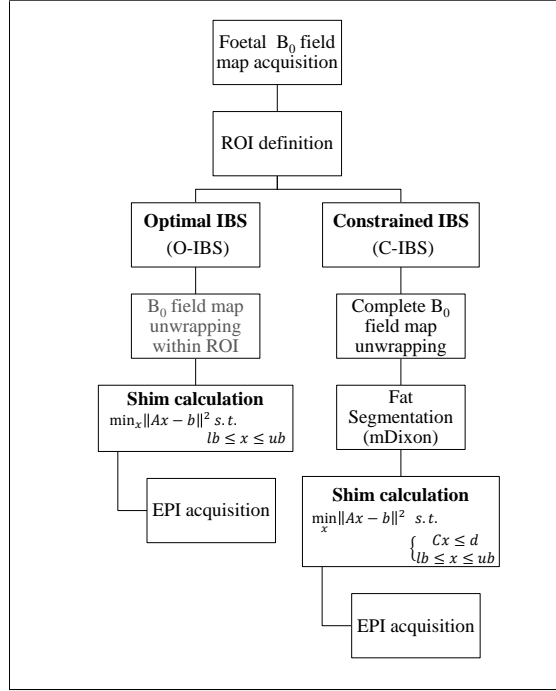


Figure 5.2: Schematics of the two methods available in the shimming tool for foetal imaging: optimal IBS (O-IBS) and constrained (C-IBS). The ROI outlined was cylindrical. O-IBS consists in a least square minimization $\min_x \|Ax - b\|^2$ with lower bound (lb) and upper bound (ub) constraints to the shim values x according to manufacturer shim coil limits. The unwrapping procedure is applied only within the brain ROI to reduce calculation times. Constrained IBS implies a complete unwrapping of the B_0 field map because the fat regions are included in the optimization. Fat segmentation is done by thresholding Dixon images acquired immediately after the B_0 field map. For C-IBS a linear constraint $Cx \leq d$, is included, where C is the matrix that includes the fat region and d is a vector matrix defining the frequency limits.

The ROI definition was simplified because the brain of a foetus is more spherical than a neonate and no external air/tissue boundaries have to be considered. In addition, regions above and below (in the z direction) can be included in the shim optimization because those regions are still within the mother’s abdomen and have a magnetic susceptibility similar to that present in the baby’s head. A circular ROI was drawn simultaneously in all slices of the foetal brain.

Fat imaging (Dixon) was required in order to segment those regions in the B_0 field map. Fat images were segmented automatically by applying a threshold of 0.3 of the normalized image. The binary image was then transformed to the B_0 field map coordinates. Then B_0 field map was completely unwrapped in order to have the correct field value near the edges where the frequency is usually higher.

Shim values up to second order harmonics were calculated according to the aforementioned two approaches. The first one is the O-IBS that corresponds to an optimization of the magnetic field within the brain ROI according to the algorithm used for neonatal shimming.

The second method (constrained IBS) limits the optimization according to the fat's resonance frequency. In this case the problem was defined as a least square fit with linear constraints $Cx \leq d$:

$$\min_x \|Ax - b\|^2 \text{ such that } \begin{cases} Cx \leq d, \\ lb \leq x \leq ub. \end{cases} \quad (5.1)$$

Where $A \in \mathbb{R}^{k \times n}$ is the spatial distribution of n spherical harmonic fields in k positions within the brain ROI, C is the matrix that includes the fat region and d is a vector matrix defining the frequency limits for lipids. Two constraints were employed. Both were chosen according with the pulse maximum magnetization interval after the offset optimization. The upper bound was chosen in order constraint the fat frequency from the water, and the lower bound was selected in order to prevent the fat frequency to leak into lower frequencies.

$$F_{0,fat} - 300 \leq Cx \leq F_{0,fat} + 100 \text{ Hz} \quad (5.2)$$

$F_{0,fat}$ is the mean magnetic field mapped within the fat regions. The conditions are defined to specify a set of feasible points x that form possible solutions. C-IBS was implemented with the same function *lsqlin* from Matlab with an active-set algorithm. An active-set algorithm creates a first collection of possible solutions with an interval defined by γ :

$$Cx - \gamma \leq d \quad (5.3)$$

This defines the initial working set. Iteratively, the direction which minimises the residuals and simultaneously fulfils the constraints in the maximum number of points is defined [60, 61]. Constraints to the solution were also included according to the maximum shim settings allowed by the manufacturer.

In agreement with the dispersion measures applied in the neonatal section (Chapter 3), characterization of field inhomogeneity was done using the FWHM, SD and 95 % interval of the residual B_0 field maps.

5.3 Results

5.3.1 B_0 -map homogeneity

Measures of dispersion of the residual B_0 field map within the foetal brain ROI without shim (NS), and using either O-IBS or C-IBS are presented in table 5.1 and figure 5.3.

Table 5.1: Dispersion measures (Mean \pm standard deviation) in Hz, within the foetal brain ROI: full-width half maximum (FWHM); 95 % interval; standard deviation (SD). Sample with 6 subjects.

	NS	O-IBS	C-IBS
<i>FWHM</i> (Hz)	18.7 \pm 6.9	4.3 \pm 1.6	4.8 \pm 1.5
95% <i>interval</i> (Hz)	70.0 \pm 24	21.3 \pm 11.3	23.0 \pm 12.1
<i>SD</i> (Hz)	35.8 \pm 12.3	10.9 \pm 5.7	11.7 \pm 5.9

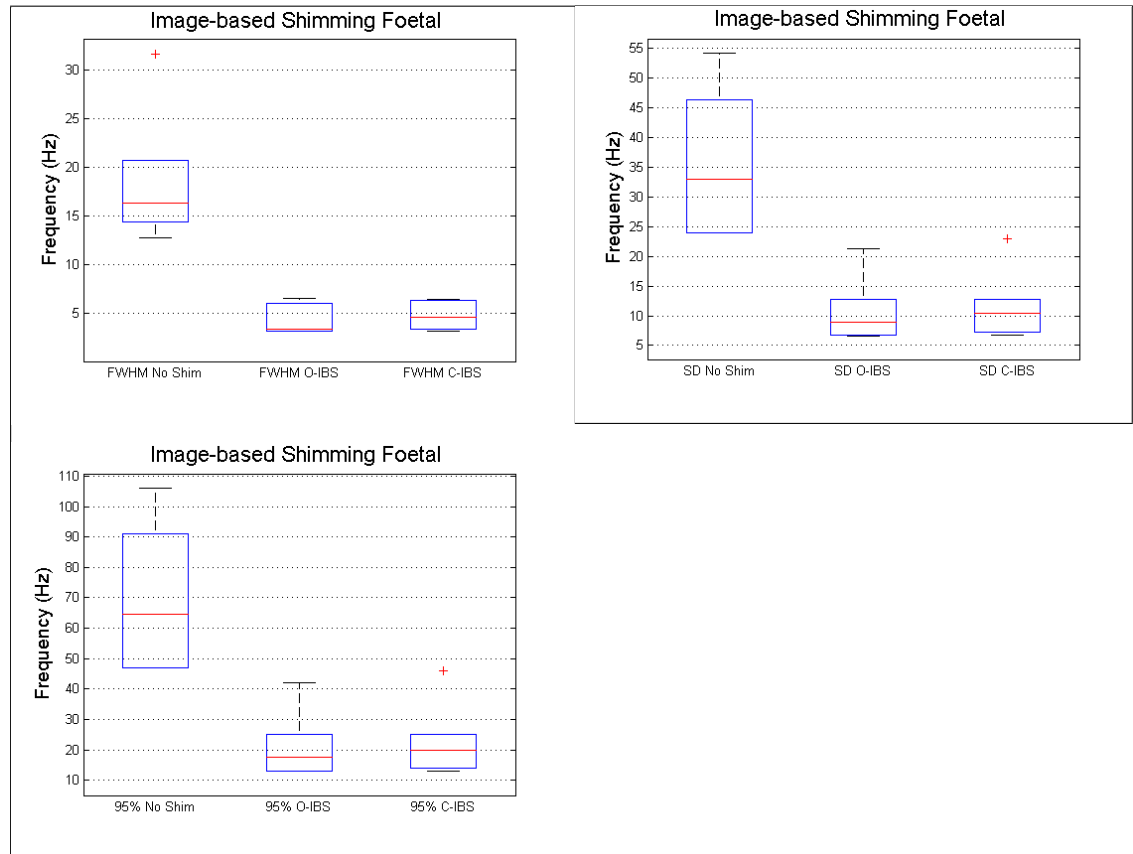


Figure 5.3: Box plot of measures of dispersion within the foetal brain ROI. The first plot shows the FWHM of the B_0 field map without shim and the same measure for the residual B_0 field map when using either C-IBS or O-IBS. The second plot on the right shows the SD of the B_0 field map without shim and the same measure for residual B_0 field maps. Finally, the plot on the bottom shows the 95% interval of the B_0 field map without shim and after using either type of shimming approach.

5.3.2 Fat suppression and EPI imaging

SPIR and shim calculation were tested in a kidney of two healthy volunteers. This allowed to find the most adequate group of settings for the fat saturation pulse, and optimize the shim

calculation accounting for it. After defining the optimal settings, foetal testing was carried out.

5.3.2.1 Fat suppression - Kidney testing

This section presents the results from kidney testing in two subjects. In the first, different shim approaches (No shim, PB volume and O-IBS) and SPIR offsets (Figures 5.4 to 5.6) were tested. In the second, the combination of different SPIR pulse offsets and durations was tested (Figures 5.7 and 5.8).

In figure 5.4 one EPI slice of a kidney is presented in different conditions. The method Dixon allows to extract fat and water images identified in the same figure. In the absence of shimming, the kidney presents deformation but fat is saturated. Nevertheless, when applying O-IBS or PB volume with the same fat suppression method has worst results.

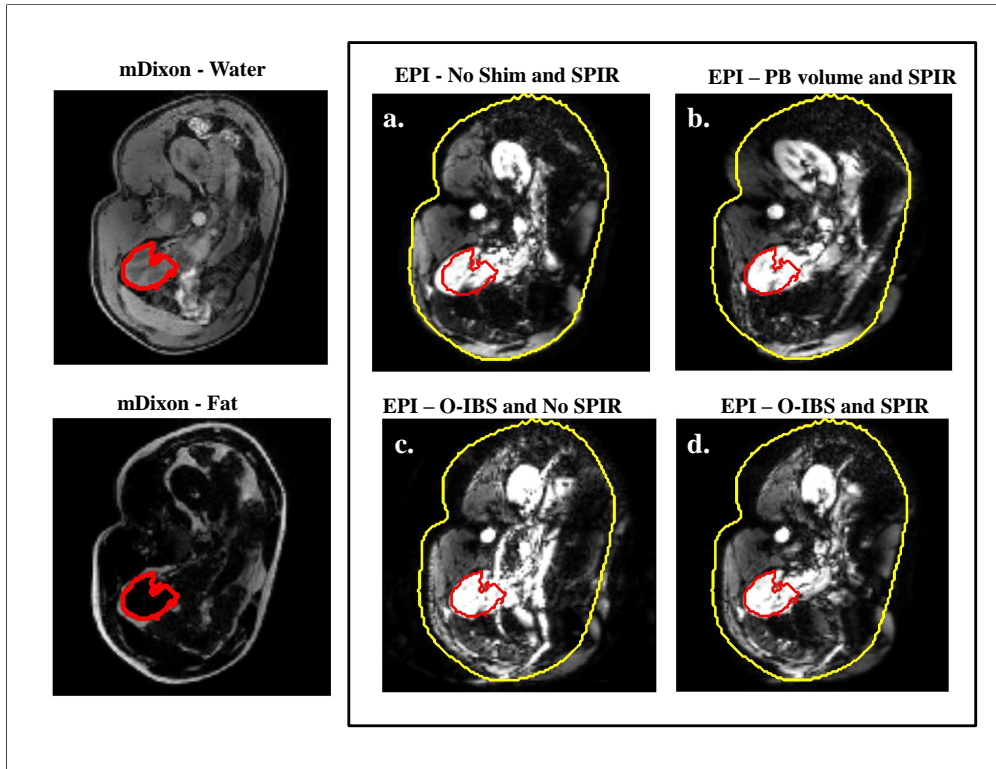


Figure 5.4: Effect of SPIR and shim application in abdomen EPI. Images were normalized to the same value. The images on the left were acquired with Dixon which does not suffer deformation. This method reveals water (first image at the top) and fat images (first image at the bottom). The first row presents EPI images acquired: **a.** without shim; and **b.** with PB volume. The second row presents two EPI acquisitions of a kidney: **c.** with O-IBS with no SPIR; and **d.** default SPIR settings. It is possible to observe a wrap of the fat that passes above the shimmed kidney (with red delineation) in **c.**.

Field maps presented in figure 5.5 at different shim conditions are consistent with EPI find-

ings. In that figure it is possible to observe that without shim the frequency histogram of fat regions show reduced dispersion and it is within the interval of frequencies that the standard fat saturation pulse would saturate. Nevertheless, when IBS is applied, the dispersion of fat frequency increases towards the right, bringing it closer to the resonance frequency of water. In the same subject different saturation pulse frequency offsets were tested (Figure 5.6).

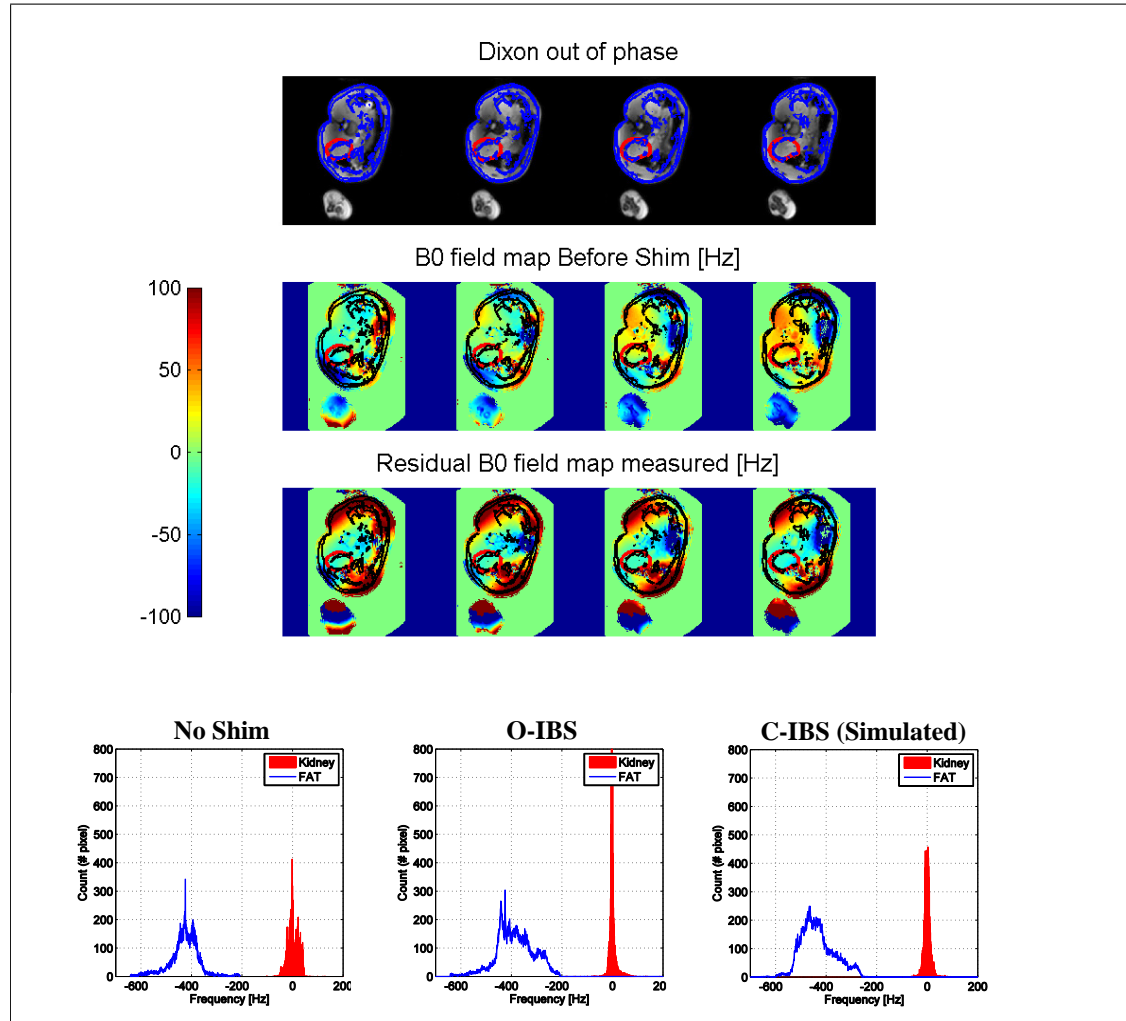


Figure 5.5: Torso B_0 field map before and after O-IBS in Hz. First row presents four slices (from 10 slices included in the IBS) of the abdomen from a Dixon acquisition out of phase (blue - fat extracted from the Dixon acquisition; red - ROI selected for the IBS.) Second row: B_0 field map before IBS (black - fat extracted from Dixon); Third row: Residual B_0 field map after IBS (black - fat extracted from Dixon). The fourth row presents the histograms of fat and kidney regions of the B_0 field map measured without shim, O-IBS and simulated C-IBS.

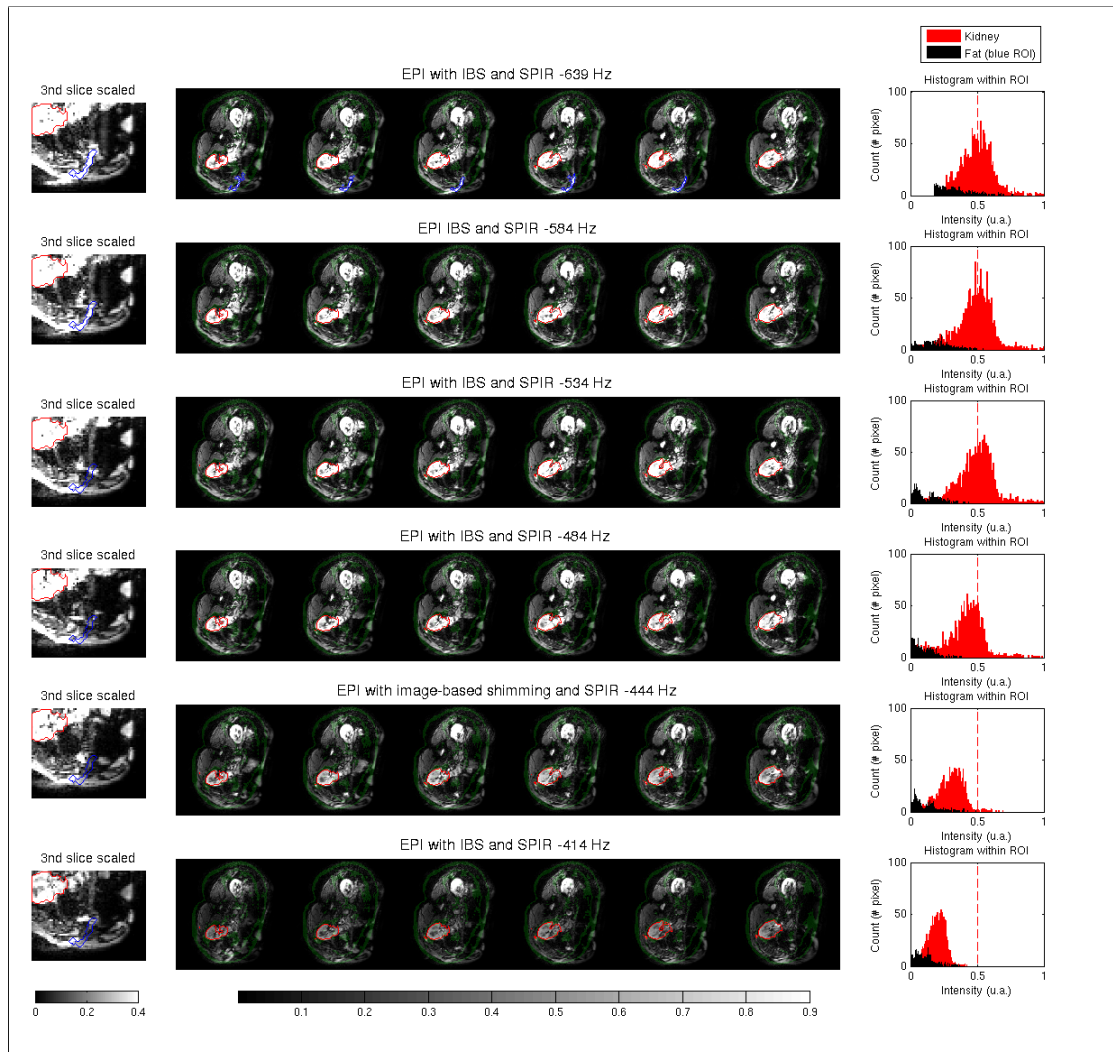


Figure 5.6: Effect of saturation pulse frequency offset on the kidney signal intensity when applying O-IBS. Six offsets were tested. On the left the images are cropped and scaled to evaluate the effect of the change. The kidney region is outlined in red while the non-saturated fat is in blue. On the right histograms of the signal from the kidney region is represented in red and the fat region in black (corresponding to the region delineated in blue).

In figure 5.7 a slice of the B_0 field map of the torso of a second healthy volunteer is displayed before and after O-IBS is applied to the kidney. In this figure it is possible to observe a fat region where the frequency is higher and reaches -166 Hz (accounting for a fat water shift of -433 Hz).

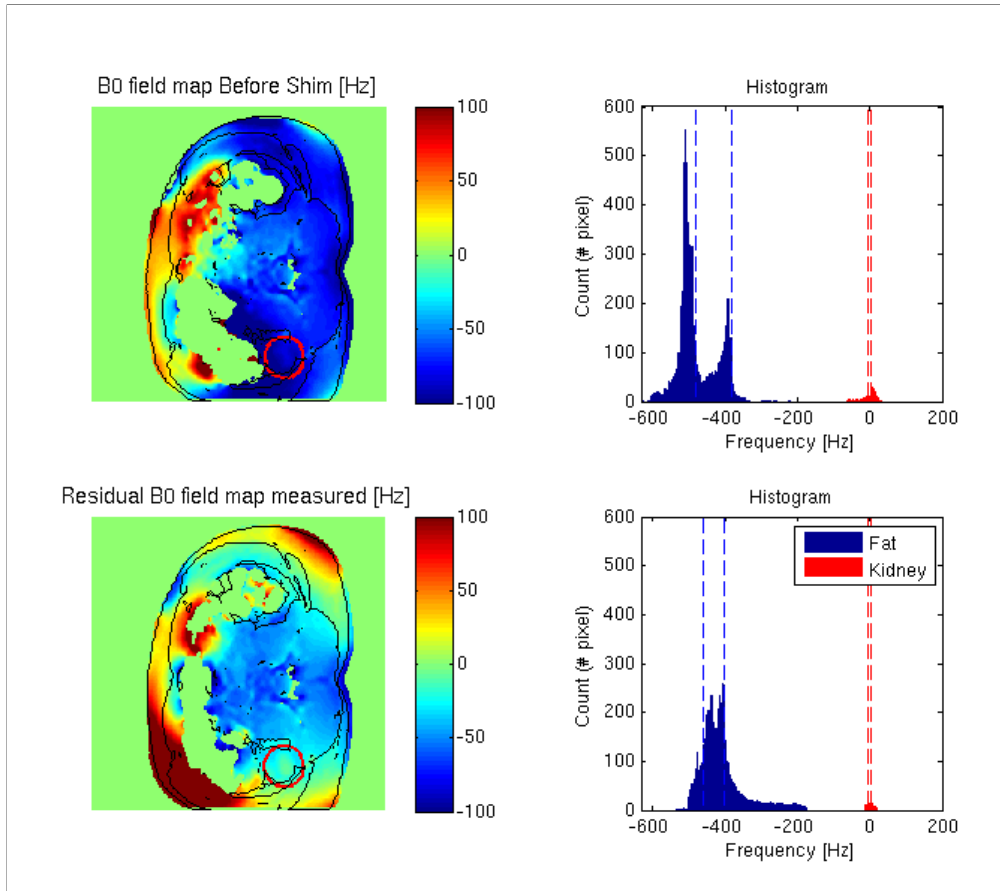


Figure 5.7: First slice of the B_0 field map measured pre and post O-IBS of the left kidney (red ROI). The fat region is outlined in black in both images. The top histogram corresponding to an histogram of fat (blue) and kidney (red) regions before O-IBS. The bottom histogram was obtained from the map measured after O-IBS of the kidney. The residual B_0 field map exhibits a fat region where the field map frequency reaches 267 Hz (taking into account that the fat-water shift corresponds to -166 Hz).

By applying the O-IBS with the EPI method and different saturation pulse settings, it is possible to observe that is difficult to remove the fat signal without affecting the water signal in the region of interest(see Figure 5.8).

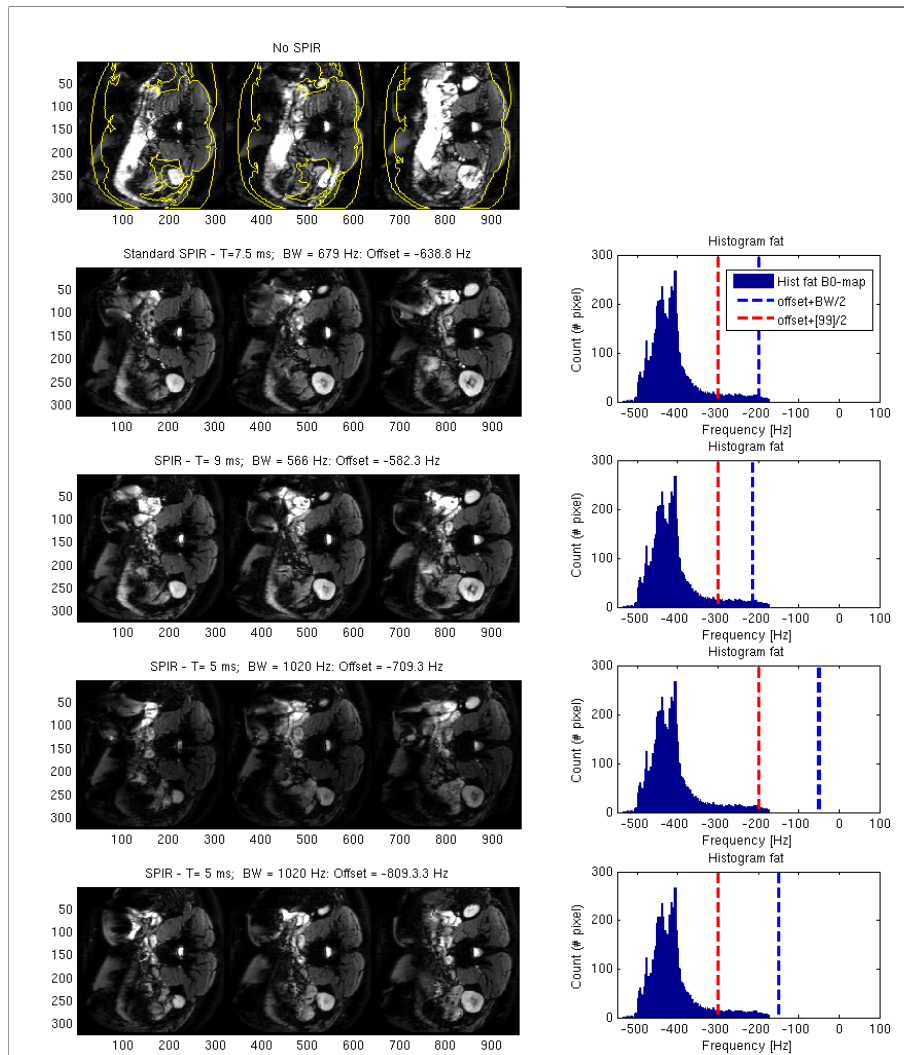


Figure 5.8: EPI images of the abdomen (kidney level) after applying different saturation pulse settings when applying O-IBS. The first EPI image was acquired without SPIR and the fat location according to the Dixon acquisition is presented in yellow. The right column exhibit the histogram of the fat region in the B_0 -map after O-IBS as shown in Figure 5.7. Red dashed line represent the pulse offset plus half the bandwidth (BW) of the pulse and the blue dashed line represents the pulse offset plus half the bandwidth for which the magnetization profile decreases by 99%. Slice position is approximately the same as that presented in Figure 5.7.

5.3.2.2 Fat suppression - Foetal EPI

The new C-IBS applied in the foetal context showed an improvement in fat suppression in 5 of 6 participants tested. The number of iterations needed for O-IBS were between 2 and 4, and for C-IBS it took between 10 to 15 iterations for the algorithm to converge.

Three examples of the EPI acquisition with different shimming approaches are presented in

this section. The first example shows the effect of three shim approaches: linear shim (Auto-shim); O-IBS and C-IBS with the respective B_0 field map (Figures 5.9 and 5.10). The second shows EPI images with O-IBS with and without the optimized offset and C-IBS with the optimized offset (Figure 5.12). For this subject the B_0 field maps with O-IBS and C-IBS are presented along with fat histograms in figure 5.11 and table 5.1. The presentation of slices without foetus's brain intends to demonstrate the efficiency of the method in locations where the brain is not currently present but where to the baby can move into. The third example shows a systematic representation of O-IBS and C-IBS with and without an optimized saturation pulse offset (Figure 5.13).

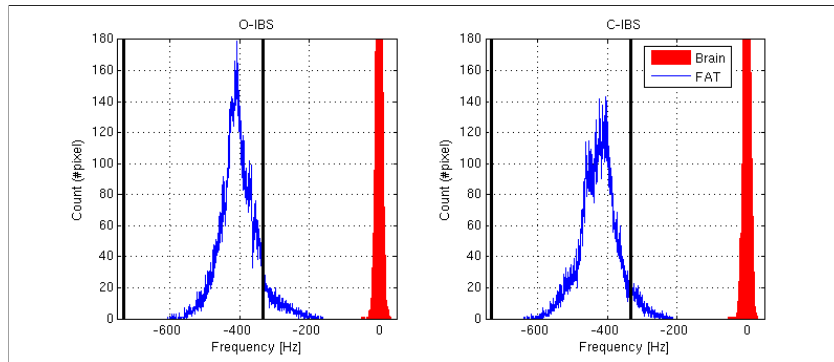


Figure 5.9: Histogram of the pixels in fat and brain. In O-IBS 8.4 % of fat pixels are outside the boundaries and in C-IBS this fraction is reduced to 5.2 %.

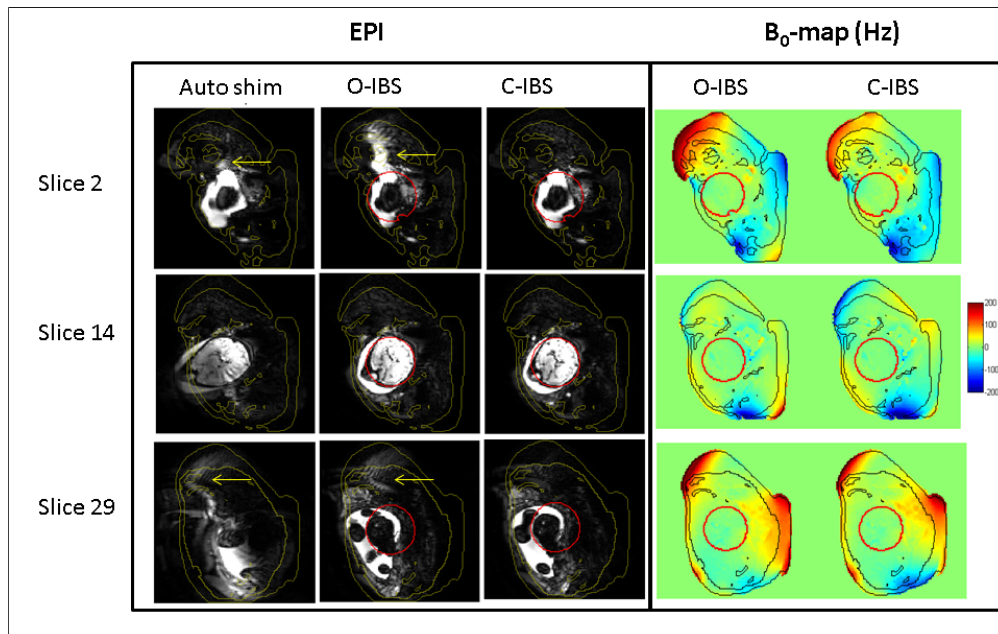


Figure 5.10: EPI with different shim methods O-IBS, C-IBS and Auto. In yellow fat region segmented with Dixon is outlined. Foetal brain ROI is delineated in red. The yellow arrows indicate regions where fat was not saturated.

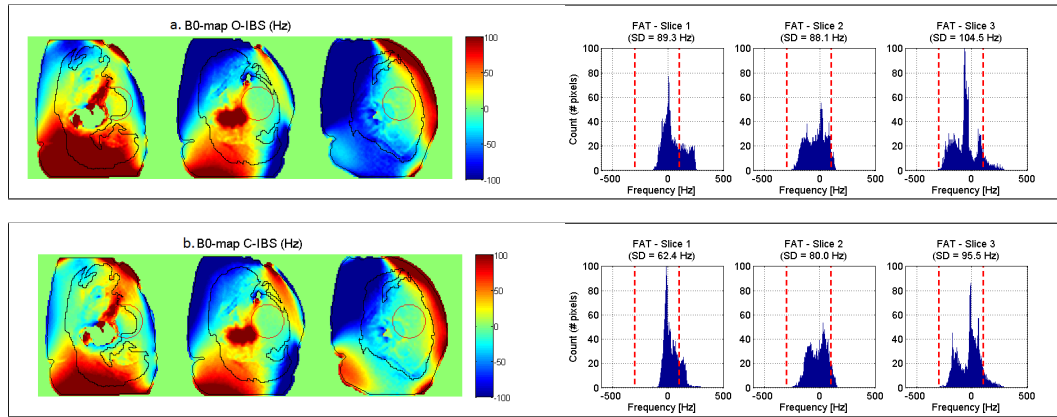


Figure 5.11: B_0 map of a foetal acquisition predicted using: a. optimal IBS (O-IBS); and b. constrained IBS (C-IBS). In black is represented the fat region. The histograms represent pixel intensity within the fat region of each slice. Red dashed lines in the histograms are the limits in the constrained fit $[-300; 100]$ Hz).

Table 5.2: Dispersion measures (Mean \pm standard deviation) in Hz, within three slices of the foetal brain ROI example: full-width half maximum (FWHM); 95 % interval; standard deviation (SD).

	Slice 1		Slice 2		Slice 3	
	O-IBS	C-IBS	O-IBS	C-IBS	O-IBS	C-IBS
50% interval (Hz)	76.8	50.5	45.3	39.8	66.1	40.9
95% interval (Hz)	175	122	173	157	205	187
SD (Hz)	89.3	62.4	88.7	80.0	104.5	85.5

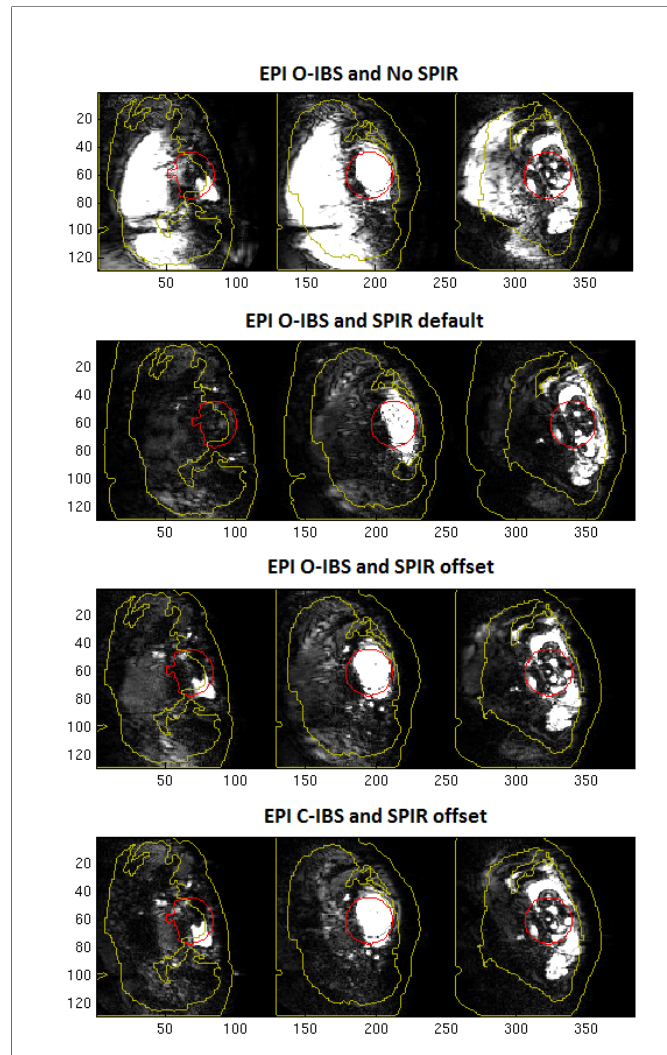


Figure 5.12: Foetal EPI with different shim methods O-IBS, C-IBS while varying the saturation pulse frequency offset. The fat region segmented with Dixon is outlined in yellow. The foetal brain ROI is delineated in red. The first row presents images acquired with the O-IBS method and no SPIR, where a large region of non-saturated fat is shown. The second and third rows present the results when O-IBS are applied with default and optimized saturation pulse offsets, respectively. The fourth row presents EPI when combining C-IBS with the new SPIR offset.

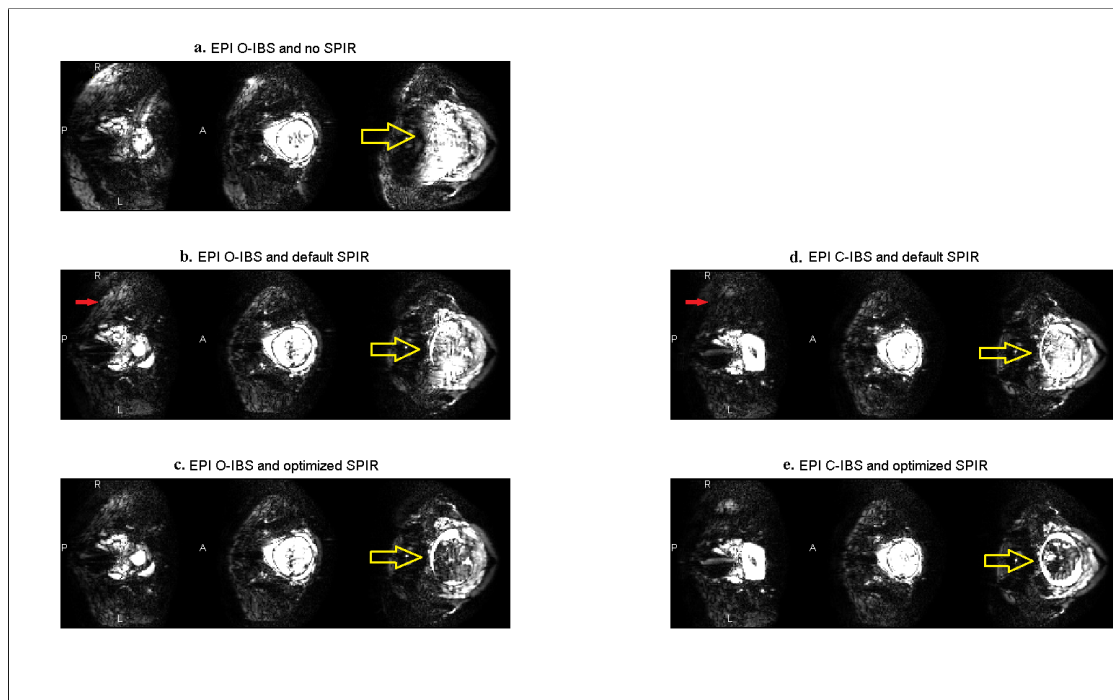


Figure 5.13: Foetal EPI images of one volunteer. EPI acquired with O-IBS and C-IBS are presented with default SPIR and optimized SPIR offset (shift of 220 Hz relative to the default). The arrows show the regions where fat was more difficult to saturate with the default method. Yellow arrows indicate fat contamination that was mainly corrected with the new saturation pulse offset, and arrows in red indicate fat that was corrected with C-IBS. The percentage of the B_0 field map in fat pixels which were outside the constraints $[-300\ 100]$ Hz) were 21% for O-IBS and 15 % for C-IBS.

5.4 Discussion

Foetal EPI scanning has specific properties that differentiate shimming requirements of this type of imaging from neonatal. First, the foetal brain is surrounded by the mother’s abdomen, which changes the magnetic environment within which the brain is immersed. Second, the foetus is not in the same position for all scans. Finally, the mother has adipose tissue responsible for extreme chemical shift artefacts. The work presented in this chapter implements an image-based shimming technique adjusted to foetal EPI requirements.

In a foetal scan, it is important to account for the baby’s positioning and motion. The first task in any foetal acquisition is to identify the babies position. In all six studies the baby had the head facing downwards and it was positioned at the level of the mother’s coccyx. Although the baby could move during the acquisition, the predicted measures of dispersion B_0 map were in concordance with those of the residual field map. This can be related with the ROI being

defined as a cylinder in the z direction across which the magnetic field was shimmed. One other factor that can contribute for the similarity between measured and predicted B_0 field map is the fact that in the final weeks of gestation the babies motion is constrained due to the limited space available in the womb leading to small variations of position that do not change the field considerably. The effect of variations in the magnetic field due to the mother's respiration are also small if we consider a ROI large enough in the z direction.

In addition to motion the presence of adipose tissue typical of pregnancy can have severe implications in an EPI acquisition, especially when a localized shimming method is applied. In this context, the study of the adequacy of the fat suppression technique is of utmost importance. The fat suppression method chosen was SPIR with a low flip angle (105 degrees) in order to have a reduced time between pulse application and sequence initiation, as opposed to STIR (short inversion time inversion recovery) [62]. In STIR all spins are initially inverted and the sequence starts when fat spins are perpendicular to M_z , i.e. after the inversion time of fat (in the order of 125 ms). This corresponds to a TI of the order of 125 ms which is too high a penalty.

In SPIR the RF pulse is spectrally selective which implies that the saturation band is correctly located over the fat's main range of frequencies. The study of O-IBS in a kidney of a healthy volunteer showed that the abdominal fat frequency gets close to water signal when that method is applied. In addition, the simulated frequency profile of the saturation pulse appeared slightly shifted to lower frequencies. The experimental study with EPI acquisitions showed that the saturation pulse frequency offset more appropriate under these shimming conditions would be -534 Hz (shift of 220 Hz). With that value water spins within the kidney did not suffer a decrease of their signal intensities.

Combination of different saturation pulse duration (proportional to $1/BW$) and offset showed it can be difficult to integrate changes of both parameters in one optimal solution. This is particularly true because the pulse offset takes into account the BW. If the BW decreases the offset also decreases. Although different combinations of BW and offset could be simulated, the real impact in water had to be tested experimentally due the existence of ripples at higher and lower frequencies of the frequency profile of the pulse. Because the study of an optimized combination of parameters was not possible in a pregnant volunteer it was chosen to adapt only the offset in the foetal applications.

The two approaches tested (O-IBS and C-IBS) presented similar outcomes in terms of field homogeneity (figure 5.3). The mean standard deviation of pixel frequency within the ROI across six subjects tested was 10.9 ± 5.7 Hz for O-IBS and 11.7 ± 5.9 Hz for C-IBS. This is consistent with the algorithm tested (active-set method) which tries to overcome the constraints changing the shimming inside the brain the least. It was showed in the first example (figure 5.10) that the application of only linear shims cannot correct inhomogeneities, leading to severe deformation of the brain and incorrect fat suppression. O-IBS is capable of avoiding deformation but it resulted in a worse fat suppression. C-IBS was able to correct both problems. The second example

shows that the application of the O-IBS and SPIR offset as a group may not generate a good result. This is because when we change the saturation pulse offset, fat protons with frequencies below -600 Hz may not be within the suppression band and are not saturated. On the other hand C-IBS accounts for both the upper and lower limits of the pulse, working in synergy with the new rf pulse offset. It is important to mention that the existence of intestinal gases in the mother can make shimming of the baby's head difficult if these regions are adjacent (Figure 5.11). This was visible in the first two slices of figure 5.11 that resulted in a slight brain deformation in the EPI image in figure 5.12. Further tests should be carried out in order to validate the evidence presented for this new method. Since only six pregnant volunteers were imaged, it would be important to investigate a wider group and relate the results with the gestational age and position position of the baby.

There are three limitations to the fat saturation method applied that should be mentioned. First, the saturation pulse did not present a sharp transition between saturation band and non saturation band. Second, the pulse presents marked ripples within its bandwidth, therefore protons with slightly different frequencies can have experienced slightly different flip angles ($\Delta FA \sim 5^\circ$). This could be overcome by changing the pulse envelope to one that would have a higher time-bandwidth product, which relates to a sharper transition in the frequency domain and less ripples.

Finally, one parameter that can also hinder fat saturation efficiency is the existence of B_1 inhomogeneities. If high imperfections are present during saturation pulse application, its real flip angle can be below or above the predicted and not saturate efficiently. Those inhomogeneities can be mapped with resource to protocols that have little sensitivity to B_0 inhomogeneities (e.g. Dual Refocusing Echo Acquisition Mode (DREAM) method [63]). If it is verified that the measured flip angle is very different from the expected, it would be possible to apply an adiabatic pulse. Nevertheless, pulses already available are designed to invert fat spin protons and not to saturate them. This happens because it is difficult to produce saturation adiabatic pulses that are spectrally selective and the ones designed are composed by a train of pulses that take more time to apply [64].

In conclusion, a new method for foetal brain shimming was presented. C-IBS demonstrates a performance comparable with O-IBS in foetal brain shimming with the advantage of a better fat suppression. Finally, the results suggest that combining C-IBS with the optimal saturation pulse frequency offset leads to the best results and should thus be the method of choice.

Chapter 6

Summary and Future work

The Developing Human Connectome Project intends to map neuronal network dynamically from 20 to 44 weeks post-conceptual age. This includes both foetal and neonatal imaging. The study of the human brain connectivity involves the use of EPI methods because they can provide adequate temporal resolution for functional imaging and the directional diffusion resolution needed. Unfortunately, due to its low bandwidth EPI is sensitive to B_0 inhomogeneities. In this context main magnetic field correction is essential. This work consisted in the study and implementation of active image-based shimming methods to improve the quality of foetal and neonatal single shot EPI. In this chapter the main results are summarized, along with possible improvements from future work.

The work was divided into three main parts. First, in Chapter 3 the limitations of image-based shimming were investigated, and the framework to apply the method was described. In chapters 4 and 5 the framework described previously was implemented in neonatal and foetal brain imaging.

The babies' brain suffers changes in dimension and shape during their development from foetal to neonatal age. In each one of those stages the baby is surrounded by a different environment which requires a distinct shimming approach.

In Chapter 3 it was possible to map the field in conditions similar to those under which the image-based shimming was subsequently applied. First, the fields generated by the shim coils were verified. With that procedure we demonstrated that the fields generated were consistent with the spherical harmonic model applied in image-based shimming in the volume intended. The shim coil fields deviation from the ideal model were of the order of $< 5 \%$ which did not justify the use of calibration data. Second, the coordinate information of the B_0 field map was corrected in order to include the table displacement needed for foetal imaging. Without this verification, it would be impossible to apply the correct shimming in the foetal head.

Neonatal shimming execution involved the creation of a tool that could be used easily by the

radiographers responsible for the acquisition. The tool included ROI definition, phase unwrapping and shim calculation. ROI definition implemented was flexible in order to adjust to the subject under study, but when applying with the same threshold/eye exclusion methodology the volume included would be similar between babies. Phase unwrapping was easily applied when needed. Finally, shim calculation allowed to generate shim values that improved inhomogeneity of the the magnetic field within the volume imaged. Although IBS showed a similar performance to PB volume in central brain neonate regions (included in the shim box), the residual B_0 field maps showed a slight improvement near the brain margins when using the former method.

Nevertheless, specific regions presented residual inhomogeneities that could have implications in EPI image quality. The study of passive shimming to correct the field in those locations can be one solution [59]. Another solution is to use the information from the residual B_0 field map and correct the image deformation during reconstruction.

For foetal shimming the groundwork presented in chapter 4 was adjusted to this cohort characteristics. The tool for foetal shimming included additional cylindrical ROI definition and constrained IBS. In foetal imaging the head is surrounded by tissue so that the difference in magnetic susceptibility in the interface foetus/mother does not require a restricted ROI definition. The constrained shimming is important because mother's adipose tissue in the presence of high shim values can lead to imperfect fat suppression.

Along with the shimming tool implementation, the rf pulse used for fat suppression was studied. It was observed that an increase of the offset of 100 Hz towards the water frequency could improve the fat suppression. It was also verified that the pulse presented a profile with ripple and a wide transition band, that limits its adjustment to the shimming problem.

The new C-IBS showed similar results in terms of field homogeneity within the foetal' brain, with improvement of fat suppression that is enhanced when used simultaneously with the optimized saturation pulse offset.

Further tests should be carried out in order to validate the results for EPI foetal shimming. The efficiency of the constrained method may also differ between different gestational ages because at the end of pregnancy the space available for the baby to move is limited in opposition to early stages. Regarding the default fat saturation pulse, it was verified that it did not have the optimal characteristics. Alternatives to that pulse that have a high time bandwidth product would have an envelop with more lobes and increase its bandwidth to the fat frequencies found during foetal shimming. Furthermore, effects of B_1 inhomogeneities in fat saturation should be investigated, and adiabatic pulses may be used as alternatives to overcome those effects.

In conclusion, the shim tools presented improved EPI image quality of the neonate and foetal brain in the context of the dHCP. The neonatal image-based shimming proved to be a reliable and consistent method, while adjustments for foetal shimming demonstrate potential to overcome limitations in fat suppression often seen with previous methods.

References

- [1] Feinberg DA, Moeller S, Smith SM, Auerbach E, Ramanna S, Glasser MF, et al. Multiplexed Echo Planar Imaging for Sub-Second Whole Brain fMRI and Fast Diffusion Imaging. *Plos One*. 2010;5(12):e15710.
- [2] Feinberg DA, Setsompop K. Ultra-fast MRI of the human brain with simultaneous multi-slice imaging. *Journal of Magnetic Resonance*. 2013;229:90 – 100.
- [3] Alayar K, Ramin VP, Bourekas EC. Editorial: MRI in Neurosciences. *International Journal of Biomedical Imaging*. 2012;p. 2.
- [4] Brown MA, Semelka RC. *MRI: Basic Principles and Applications*. New Jersey: Wiley; 2011.
- [5] Bernstein MA, F KK, Zhou XJ. *Handbook of MRI Pulse Sequences*. London: Academic Press; 2004.
- [6] Haacke EM, Brown RW, Thompson MR, Venkatesan R. *Magnetic Resonance Imaging: Physical Principles and Sequence Design*. New York: Wiley; 1999.
- [7] McRobbie DW. *MRI from Picture to Proton*. Cambridge University Press; 2003.
- [8] Lvovsky Y, Stautner EW, Zhang T. Novel technologies and configurations of superconducting magnets for MRI. *Superconductor Science and Technology*. 2013;26(9):093001.
- [9] Hashemi RH, Bradley WG, Lisanti CJ. *MRI: The Basics*. New York: Lippincott Williams & Wilkins; 2010.
- [10] Chapter 16 - Echo Train Pulse Sequences. In: Zhou MA, Bernstein KF, King XJ, editors. *Handbook of MRI Pulse Sequences*. Burlington: Academic Press; 2004. p. 702 – 801.
- [11] Jezzard P, Balaban RS. Correction for Geometric Distortion in Echo Planar. *Magnetic Resonance in Medicine*. 1995;34(1):65–73.
- [12] Koch KM, Rothman DL, de Graaf Ra. Optimization of static magnetic field homogeneity in the human and animal brain in vivo. *Progress in Nuclear Magnetic Resonance Spectroscopy*. 2009;54(2):69–96.

-
- [13] Jezzard P, Clare S. Sources of distortion in functional MRI data. *Human Brain Mapping*. 1999;8(2-3):80–85.
- [14] Wang M. *Industrial Tomography: Systems and Applications*. Woodhead Publishing Series in Electronic and Optical Materials. Elsevier Science; 2015.
- [15] Cameron I. Techniques of Fat Suppression. In *Proceedings of the 17th Annual Meeting of International Society for Magnetic Resonance in Medicine*; 2009. .
- [16] Salomir R, de Senneville BD, Moonen CT. A fast calculation method for magnetic field inhomogeneity due to an arbitrary distribution of bulk susceptibility. *Concepts in Magnetic Resonance Part B: Magnetic Resonance Engineering*. 2003;19B(1):26–34.
- [17] Marques JP, Bowtell R. Application of a fourier-based method for rapid calculation of field inhomogeneity due to spatial variation of magnetic susceptibility. *Concepts in Magnetic Resonance Part B: Magnetic Resonance Engineering*. 2005;25(1):65–78.
- [18] Schenck JF. The role of magnetic susceptibility in magnetic resonance imaging: MRI magnetic compatibility of the first and second kinds. *Medical Physics*. 1996;23(6):815–850.
- [19] Clare S, Evans J, Jezzard P. Requirements for room temperature shimming of the human brain. *Magnetic Resonance in Medicine*. 2006;55(1):210–214.
- [20] Schneider E, Glover G. Rapid in vivo proton shimming. *Magnetic Resonance in Medicine*. 1991;18(2):335–347.
- [21] Schar M, Kozerke S. Local linear shimming for cardiac SSFP imaging at 3T. vol. 10. In *Proceedings of the 10th Annual Meeting of International Society for Magnetic Resonance in Medicine*; 2002. p. 1735.
- [22] Funai AK, Fessler JA, Yeo DTB, Olafsson VT, Noll DC. Regularized field map estimation in MRI. *IEEE Transactions on Medical Imaging*. 2008;27(10):1484–1494.
- [23] While PT, Korvink JG. Designing MR Shim Arrays With Irregular Coil Geometry: Theoretical Considerations. *IEEE Transactions on Biomedical Engineering*. 2014;61(6):1614–1620.
- [24] Chmurny GN, Hoult DI. The Ancient and Honourable Art of Shimming. *Concepts in Magnetic Resonance*. 1990;2(3):131–149.
- [25] Gruetter R, Boesch C. Fast, noniterative shimming of spatially localized signals. In vivo analysis of the magnetic field along axes. *Journal of Magnetic Resonance*. 1992;96(2):323–334.
- [26] Golay MJE. Field homogenizing coils for nuclear spin resonance instrumentation . *Review of Scientific Instruments*. 1958;29(4):313–315.

-
- [27] Gruetter R. Automatic, localized in Vivo adjustment of all first-and second-order shim coils. *Magnetic Resonance in Medicine*. 1993;29(6):804–811.
- [28] Shen J, Rycyna RE, Rothman DL. Improvements on an in vivo automatic shimming method (FASTERMAP). *Magnetic Resonance in Medicine*. 1997;38(5):834–839.
- [29] Shen J, Rothman DL, Hetherington HP, Pan JW. Linear projection method for automatic slice shimming. *Magnetic Resonance in Medicine*. 1999;42(6):1082–1088.
- [30] Gruetter R, Tkáč I. Field mapping without reference scan using asymmetric echoplanar techniques. *Magnetic resonance in medicine*. 2000;43(2):319–323.
- [31] Zhao YS, Anderson AW, Gore JC. Computer simulation studies of the effects of dynamic shimming on susceptibility artifacts in EPI at high field. *Journal of Magnetic Resonance*. 2005;173(1):10–22.
- [32] Webb P, Macovski A. Rapid, fully-automatic, arbitrary-volume in vivo shimming. *Magnetic Resonance in Medicine*. 1991;20(1):113–122.
- [33] Wen H, Jaffer FA. An in vivo automated shimming method taking account shim current constraints. *Magnetic Resonance in Medicine*. 1995;34(6):898–904.
- [34] Schar M, Kozerke S, Fischer SE, Boesiger P. Cardiac SSFP imaging at 3 tesla. *Magnetic Resonance in Medicine*. 2004;51(4):799–806.
- [35] Siero J, Boer V, Hoogduin J, Luijten P, Klomp D. Cost function guided 3rd order B0 shimming for MR spectroscopic imaging at 7T. vol. 17. Honolulu, Hawaii, USA: In Proceedings of the 17th Annual Meeting of International Society for Magnetic Resonance in Medicine; 2009. p. 132.
- [36] Fillmer A, Kirchner T, Cameron D, Henning A. Constrained Image-Based B-0 Shimming Accounting for “Local Minimum Traps” in the Optimization and Field Inhomogeneities Outside the Region of Interest. *Magnetic Resonance in Medicine*. 2015;73(4):1370–1380.
- [37] Fuhry M, Reichel L. A new Tikhonov regularization method. *Numerical Algorithms*. 2012;59(3):433–445.
- [38] Kim D, Adalsteinsson E. Regularized higher-order in vivo shimming. *Magnetic Resonance in Medicine*. 2002;48(4):715–22.
- [39] Tikhonov AN. Solution of incorrectly formulated problems and regularization method. *Doklady Akademii nauk SSSR*. 1963;151(3):501–504.
- [40] Ivanov VK, Ivanov VK, Vasin VV, Tanana VP. Theory of linear ill-posed problems and its applications. vol. 36. Walter de Gruyter; 2002.

-
- [41] Hansen P, OLeary D. The Use of the L-Curve in the Regularization of Discrete Ill-Posed Problems. *SIAM Journal on Scientific Computing*. 1993;14(6):1487–1503.
- [42] Golub G, Heath M, Wahba G. Generalized cross-validation as a method for choosing a good ridge parameter. *Technometrics*. 1979;21(2):215–223.
- [43] Koch KM, McIntyre S, Nixon TW, Rothman DL, de Graaf RA. Dynamic shim updating on the human brain. *Journal of Magnetic Resonance*. 2006;180(2):286–296.
- [44] Ernst T, Hennig J. Double-volume 1H spectroscopy with interleaved acquisitions using tilted gradients. *Magnetic Resonance in Medicine*. 1991;20(1):27–35.
- [45] Blamire A, Rothman D, Nixon T. Dynamic shim updating: A new approach towards optimized whole brain shimming. *Magnetic Resonance in Medicine*. 1996;36(1):159–165.
- [46] De Graaf Ra, Brown PB, McIntyre S, Rothman DL, Nixon TW. Dynamic shim updating (DSU) for multislice signal acquisition. *Magnetic Resonance in Medicine*. 2003;49(3):409–416.
- [47] Juchem C, Nixon TW, Diduch P, Rothman DL, Starewicz P, de Graaf Ra. Dynamic shimming of the human brain at 7 T. *Concepts in Magnetic Resonance Part B: Magnetic Resonance Engineering*. 2010;37 B(3):116–128.
- [48] Balteau E, Hutton C, Weiskopf N. Improved shimming for fMRI specifically optimizing the local BOLD sensitivity. *NeuroImage*. 2010;49(1):327 – 336.
- [49] Romeo F, Hoult DI. Magnet field profiling analysis and correcting coil design. *Magnetic Resonance in Medicine*. 1984;1(1):44–65.
- [50] Juchem C, Green D, de Graaf RA. Multi-coil magnetic field modeling. *Journal of Magnetic Resonance*. 2013;236:95–104.
- [51] Juchem C, Nixon TW, McIntyre S, Rothman DL, de Graaf RA. Magnetic Field Homogenization of the Human Prefrontal Cortex With a Set of Localized Electrical Coils. *Magnetic Resonance in Medicine*. 2010;63:171–180.
- [52] Jovicich J, Czanner S, Greve D, Haley E, van der Kouwe A, Gollub R, et al. Reliability in multi-site structural MRI studies: Effects of gradient non-linearity correction on phantom and human data. *NeuroImage*. 2006;30(2):436 – 443.
- [53] Barker PB, Bizzi A, Stefano ND, Gullapalli R, Lin DDM. *Clinical MR Spectroscopy*. Cambridge University Press; 2009. Cambridge Books Online.
- [54] Akinci A, Sarac K, Gungor S, Mungan I, Aydin O. Brain MR spectroscopy findings in neonates with hypothyroidism born to mothers living in iodine-deficient areas. *American Journal of Neuroradiology*. 2006;27(10):2083–2087.

-
- [55] Hughes E, Winchmann T, Mager L, Padormo F, Jana H, Wurie J, et al.. Tackling the Challenges of Imaging the Infant Brain in a Dedicated Neonatal Coil, presented at the Int. Soc. Magn. Reson. Med. 23th Annual Meeting.; 2015.
- [56] Jenkinson M, Bannister P, Brady M, Smith S. Improved optimization for the robust and accurate linear registration and motion correction of brain images. *Neuroimage*. 2002;17(2):825–841.
- [57] Greve DN, Fischl B. Accurate and robust brain image alignment using boundary-based registration. *Neuroimage*. 2009;48(1):63–72.
- [58] Goldstein RM, Zebker HA, Werner CL. Satellite radar interferometry: Two-dimensional phase unwrapping. *Radio Science*. 1988;23(4):713–720.
- [59] Yang S, Kim H, Ghim MO, Lee BU, Kim DH. Local in vivo shimming using adaptive passive shim positioning. *Magnetic Resonance Imaging*. 2011;29(3):401 – 407.
- [60] Antoniou A, Wu-Sheng L. Practical optimization: algorithms and engineering applications. New York, N.Y. Springer; 2007.
- [61] Gill PE, Murray W, Wright MH. Numerical linear algebra and optimization, Vol. 1. Redwood: Addison-Wesley Pub. Co.; 1991.
- [62] Bydder G, Young I. MR imaging: clinical use of the inversion recovery sequence. *Journal of computer assisted tomography*. 1985;9(4):659–675.
- [63] Nehrke K, Börnert P. DREAMa novel approach for robust, ultrafast, multislice B1 mapping. *Magnetic Resonance in Medicine*. 2012;68(5):1517–1526.
- [64] Abe T. Fast fat suppression RF pulse train with insensitivity to B1 inhomogeneity for body imaging. *Magnetic Resonance in Medicine*. 2012;67(2):464–469.

Appendix A

Coil verification graphs.

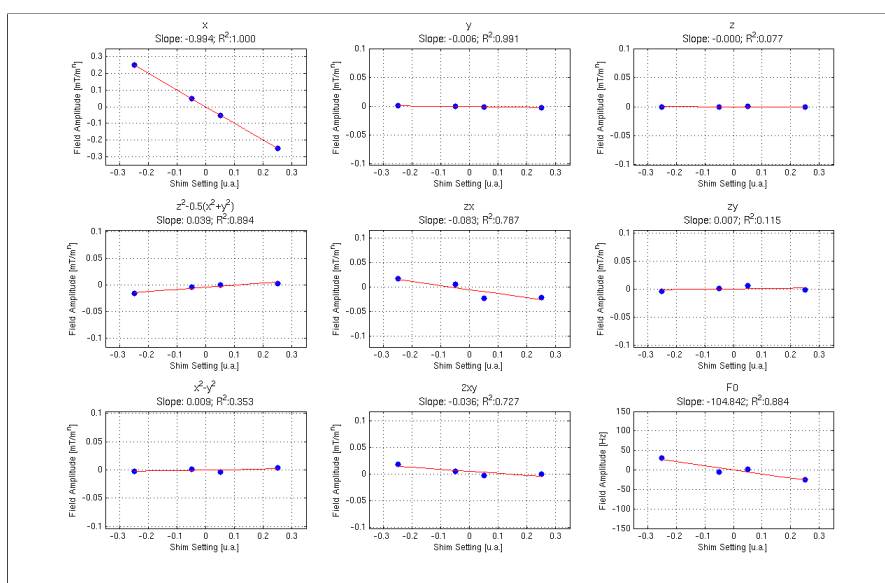


Figure A.1: Calibration plots of X coil after applying four known shim setting values.

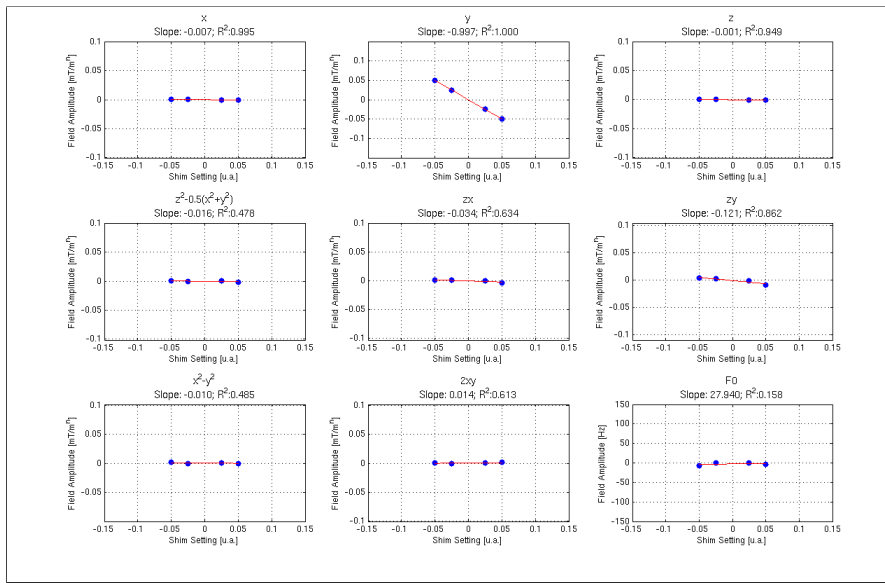


Figure A.2: Calibration plots of Y coil after applying four known shim setting values.

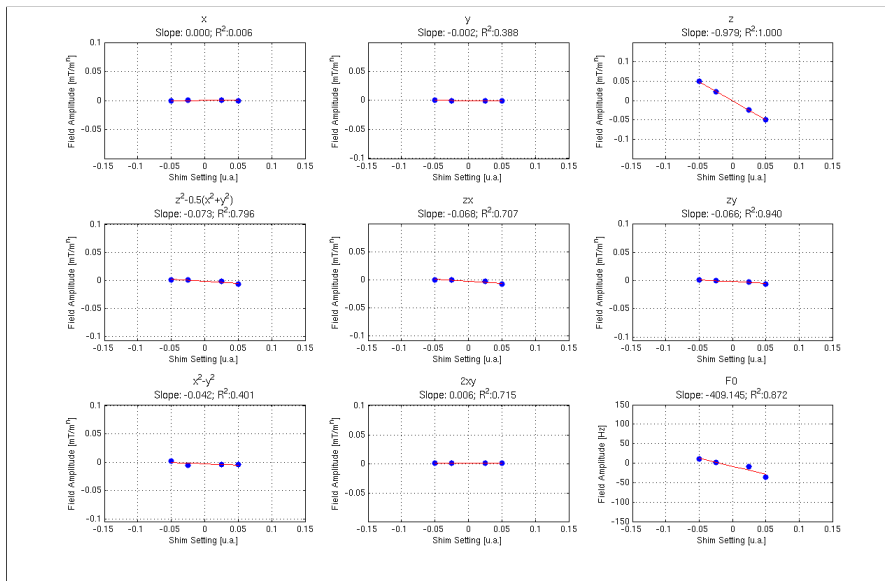


Figure A.3: Calibration plots of Z coil after applying four known shim setting values.

APPENDIX A. COIL VERIFICATION GRAPHS.

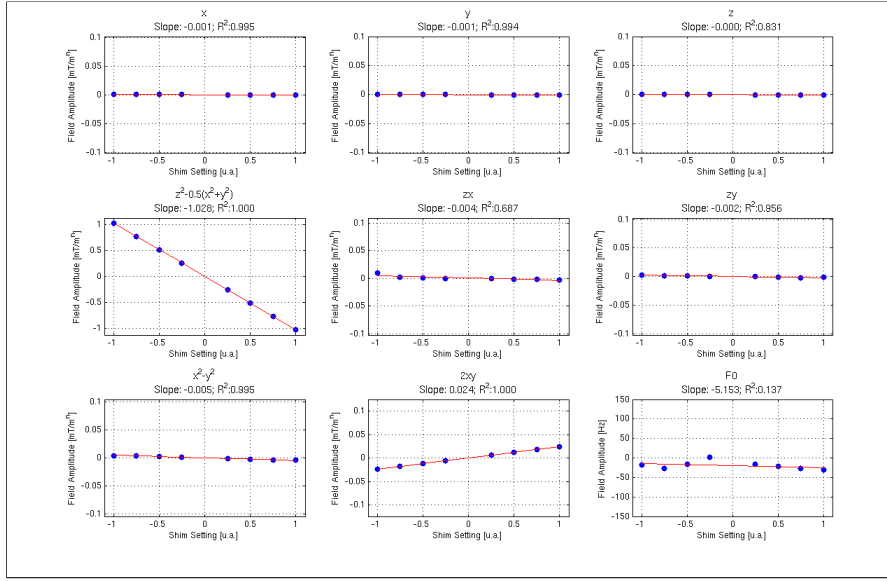


Figure A.4: Calibration plots of Z^2 coil after applying eight known shim setting values.

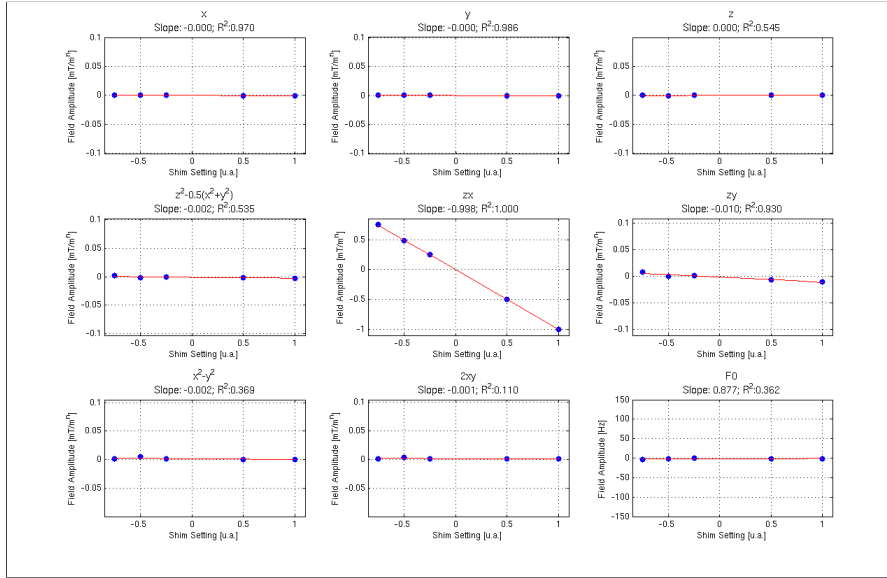


Figure A.5: Calibration plots of ZX coil after applying five known shim setting values.

APPENDIX A. COIL VERIFICATION GRAPHS.

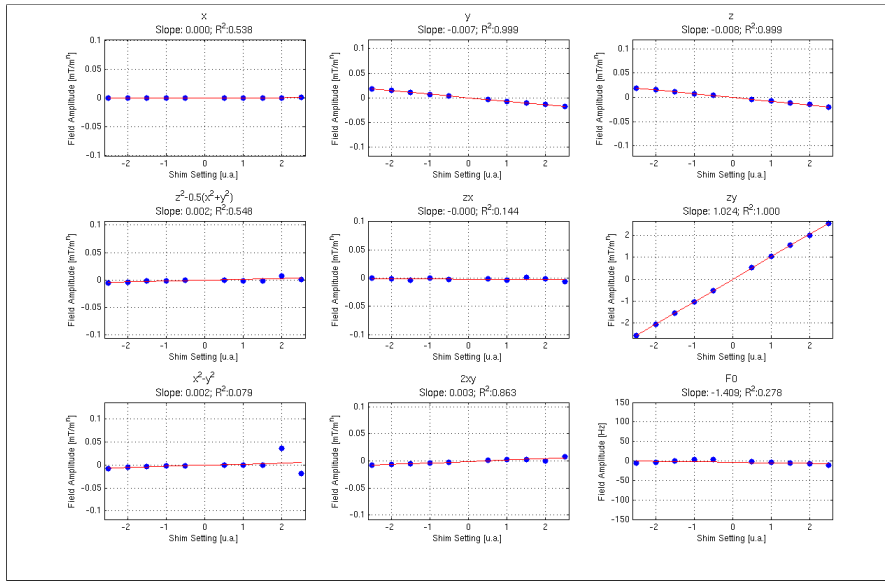


Figure A.6: Calibration plots of ZY coil after applying five known shim setting values.

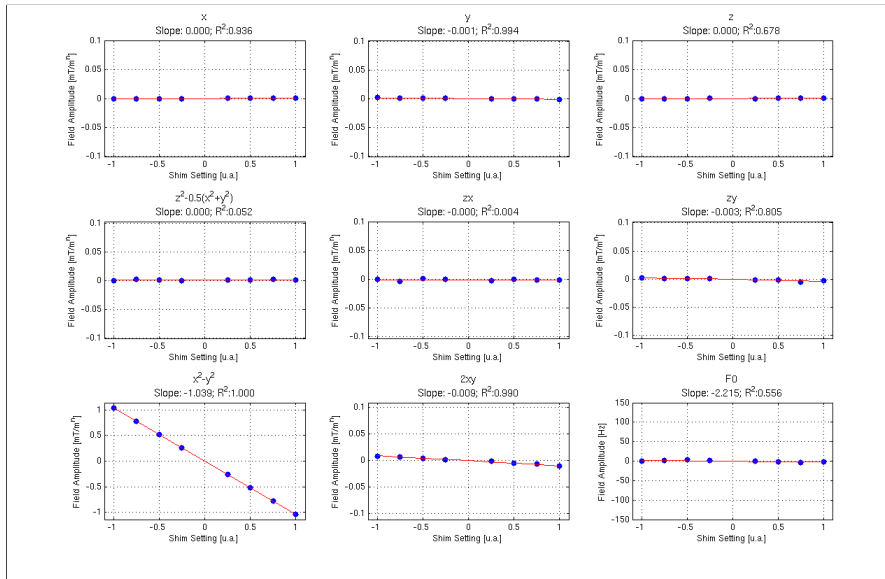


Figure A.7: Calibration plots of X2Y2 coil after applying five known shim setting values.

APPENDIX A. COIL VERIFICATION GRAPHS.

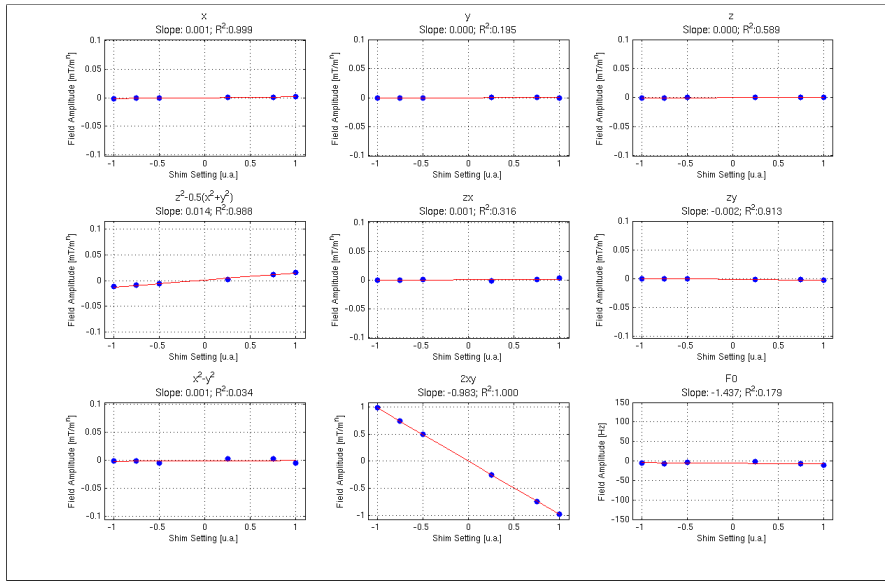


Figure A.8: Calibration plots of 2XY coil after applying six known shim setting values.

Appendix B

Regularization

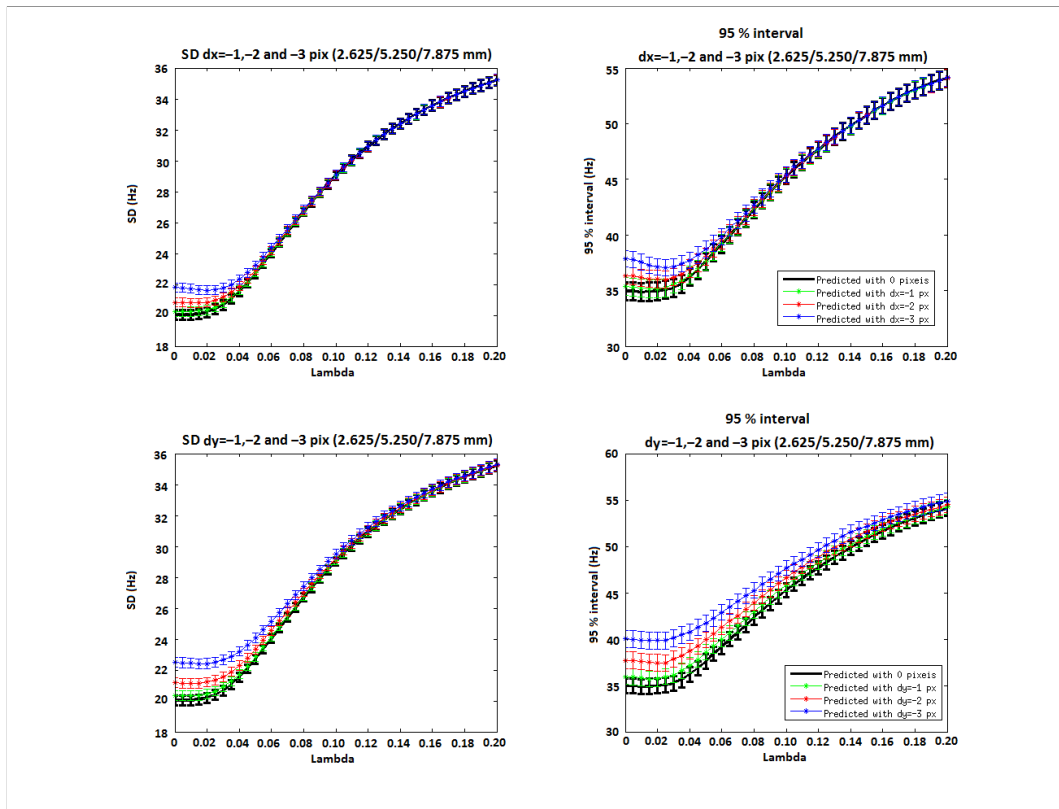


Figure B.1: Simulation of the standard deviation and 95% interval in Hz of the B_0 map if the shim values calculated with different regularization parameter (lambda) values are applied after translation in $+x$ (towards the right) and $+y$ (towards posterior) directions. Translation of 1, 2 and 3 pixels correspondent to 2.65, 5.25 and 7.87 mm. Measures presented are the mean of 10 neonatal datasets, and vertical bars represent the SD for each lambda.

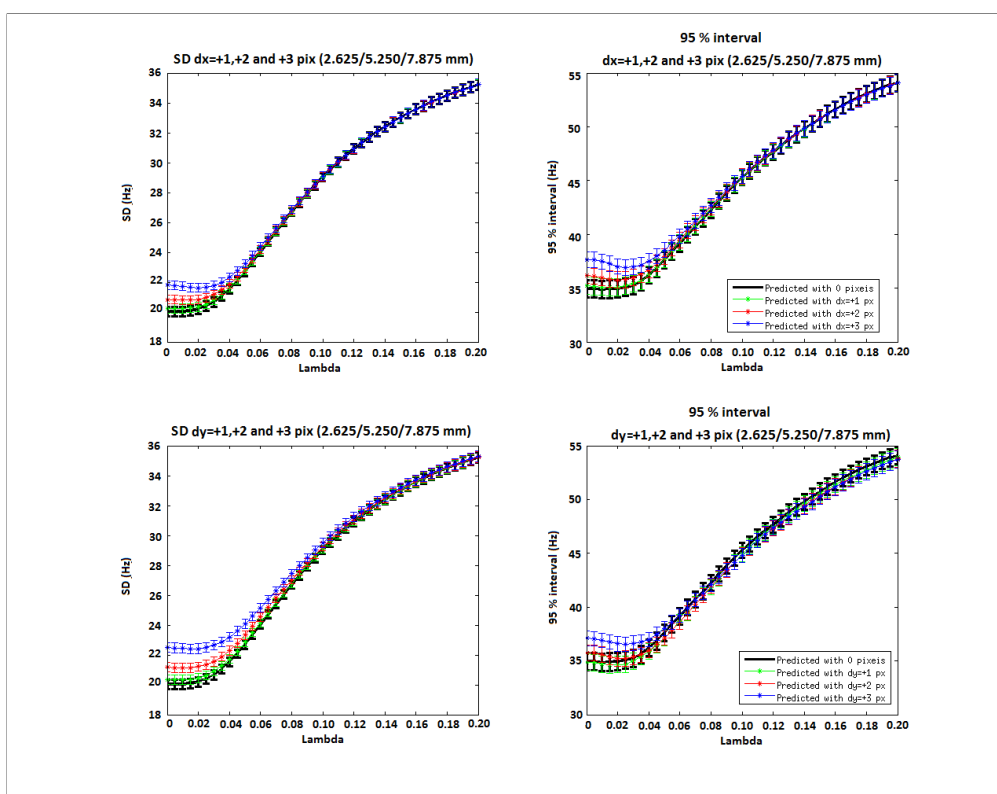


Figure B.2: Simulation of the standard deviation and 95% interval in Hz of the B_0 map if the shim values calculated with different regularization parameter (λ) values are applied after translation in $-x$ (RL) and $-y$ (PA) directions. Translation of 1, 2 and 3 pixels correspondent to 2.65, 5.25 and 7.87 mm.

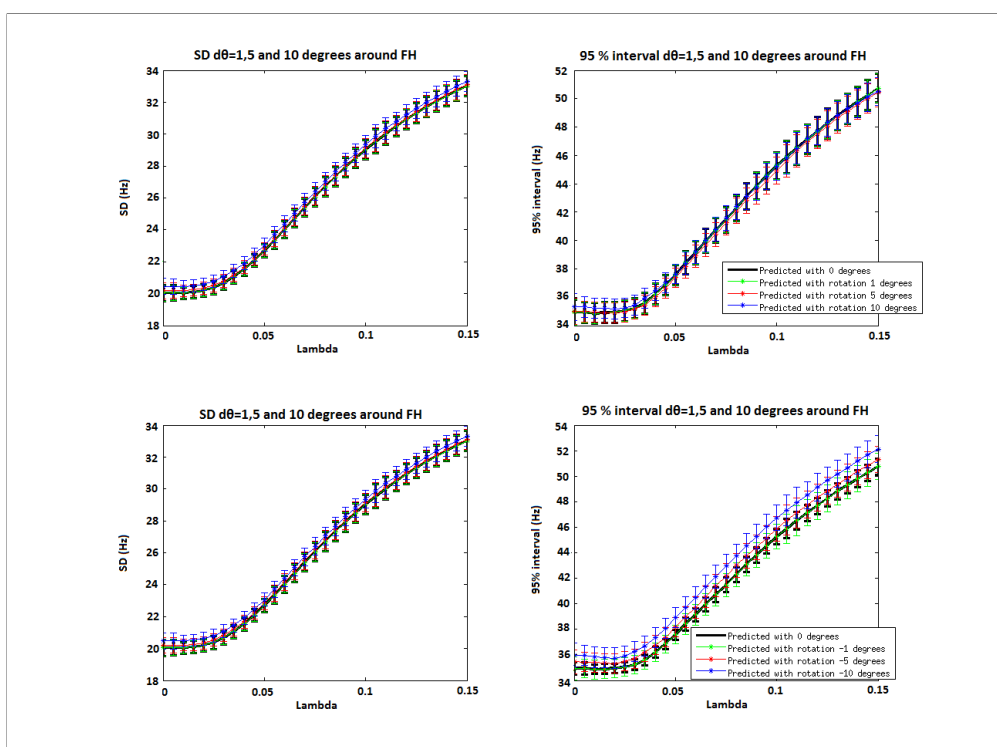


Figure B.3: Simulation of the standard deviation and 95% interval in Hz of the B_0 map if the shim values calculated with different regularization parameter (λ) values are applied after rotation in $+\theta_z$ and $-\theta_z$ directions. Rotation of 1, 5 and 10 degrees.

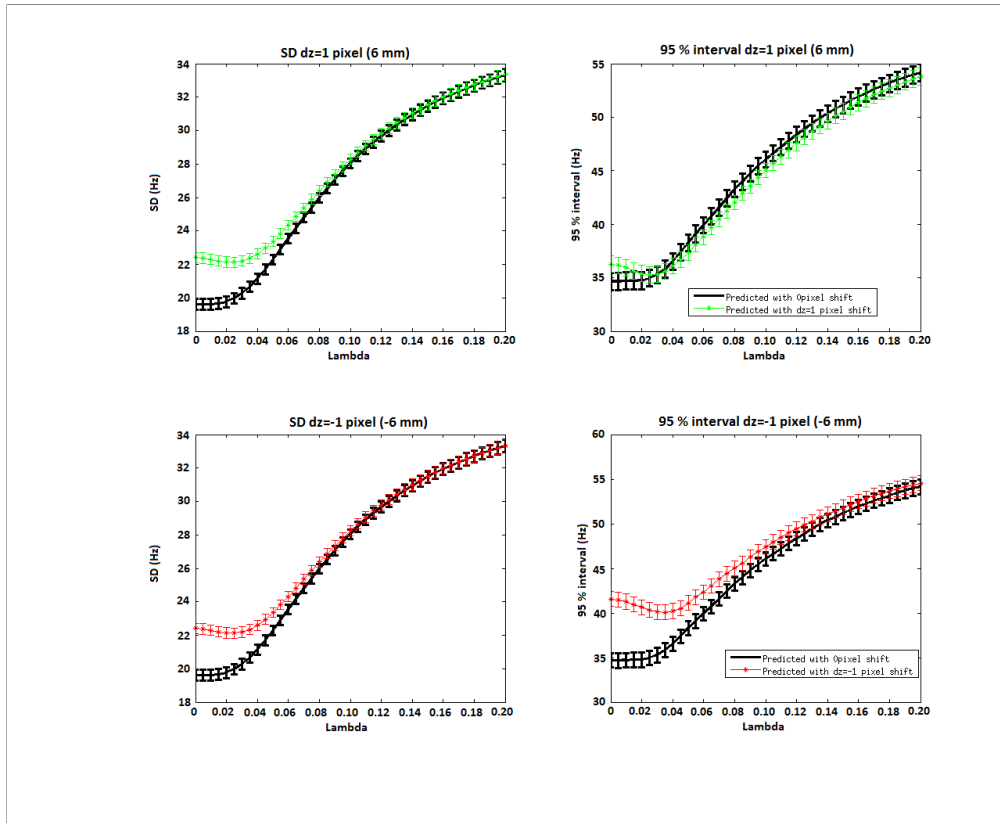


Figure B.4: Simulation of the standard deviation and 95% interval in Hz of the B_0 map if the shim values calculated with different regularization parameter (λ) values are applied after translation in dz and $-dz$ directions. Translation of 1 pixel correspondent to 6 mm.